Development of Flexible, Carbon-Based Electrochemical Energy Storage Electrodes

by

Ricky Tjandra

A thesis
presented to the University of Waterloo
in fulfillment of the
thesis requirement for the degree of
Doctor of Philosophy
in
Chemical Engineering (Nanotechnology)

Waterloo, Ontario, Canada, 2019

Examining Committee Membership

The following served on the Examining Committee for this thesis. The decision of the Examining Committee is by majority vote.

External Examiner	**NAME:** Hani Naguib Title: Professor Department of Mechanical Engineering, University of Toronto
Supervisor	**NAME:** Aiping Yu **Title:** Professor Department of Chemical Engineering, University of Waterloo
Internal Members	**NAME:** Mark Pritzker **Title:** Professor Department of Chemical Engineering, University of Waterloo
	NAME: Michael Fowler **Title:** Professor Department of Chemical Engineering, University of Waterloo
Internal-external Member	**NAME:** Na Young kim **Title:** Associate Professor Institute for Quantum Computing, University of Waterloo
Other Member(s)	n/a

Author's Declaration

This thesis consists of material all of which I authored or co-authored: see Statement of Contributions included in the thesis. This is a true copy of the thesis, including any required final revisions, as accepted by my examiners.

I understand that my thesis may be made electronically available to the public.

Statement of Contribution

The body of this thesis is based on a combination of both published and unpublished works. Various sections are adapted from the following list of publications.

Chapter 4

R. Tjandra, G. Li, X. Wang, J. Yan, M. Li, A. Yu. "Flexible high performance lithium ion battery electrode based on a free-standing TiO_2 nanocrystals/carbon cloth composite". *RSC Adv.,* 6 (42), 35479-35485. 2016

- I performed all of the experiments with guidance from G. Li and X. Wang.
- X. Wang and J. Yan gave me guidance for the data analysis and structure of the manuscript..
- M. Li helped provide suggestions and proofreading for the manuscript.

Chapter 5

R. Tjandra, W. Liu, L. Lim, A. Yu. "Melamine based, n-doped carbon/reduced graphene oxide composite foam for Li-ion Hybrid Supercapacitors. *Carbon* 129, 152-158. 2018

- I performed all of the synthesis experiments.
- W. Liu gave me guidance on the data analysis of the full-cell hybrid supercapacitor.
- L. Lim and W. Liu helped with the review of the manuscript.

Chapter 6

R. Tjandra, W. Liu, M. Zhang, A. Yu. "All-carbon flexible supercapacitors based on electrophoretic deposition of Graphene quantum dots on carbon cloth". (Submitted to *Journal of Power Sources*)

- I performed all of the experiments in this work with guidance from W. Liu, especially in the electrodeposition process of GQDs on carbon cloth.
- M. Zhang provided some of her own GQDs as a comparison for some experiments.
- W. Liu also helped review the manuscript.

Abstract

Research into energy storage and conversion technologies has skyrocketed within the past few decades, motivated by the increased energy demands of our society and the threat of depleting energy sources. One of the exciting forefronts of energy storage research is the development of flexible electrochemical energy storage systems. This area of active research is fueled by the popularity of the Internet-of-Things (IOT), smart wearables/clothing and flexible electronics. A distinct lack of commercially available electrochemical energy storage options that can be flexed, bent, stretched and twisted is currently available to power these devices. Instead, most of today's flexible electronic and wearables rely on rigid cell formats such as cylindrical and prismatic cells. The problem of flexible energy storage devices can be broken down into 2 deficiencies: the lack of flexible electrodes that can match the performance of their rigid counterparts and the lack of high-performance solid-state electrolytes. Carbon-based materials, especially nanoscale materials such as graphene, are a potential solution to this problem due to their electronic conductivity, relative abundance, energy storage capabilities, and ability to be used in all parts of the energy storage system.

All the work presented in this thesis involves the development and applications of carbon-based materials for flexible electrochemical energy storage systems. This thesis will explore two different pathways of achieving flexible electrodes based on carbon-based materials:

- Replacement of non-flexible metal foil current collectors using flexible carbon-based current collectors
- Elimination of current collectors and binders by using carbon-based, free-standing materials

Firstly, this thesis will explore the use of carbon cloth as a substrate for a novel TiO_2 nanocrystal material for use as an anode in flexible lithium-ion supercapacitors. Although lithium-ion supercapacitors are the focus of this study, the same composite material can also be used as an anode in traditional lithium-ion batteries. The resulting carbon cloth/TiO_2 composite is able to withstand 100 flexion cycles while still retaining its energy storage capabilities, showing the advantage of the carbon cloth as a substrate when compared to traditional metal foils. The composite is also successfully integrated into a flexible pouch cell that delivers an excellent reversible capacity of 270 mAh g^{-1}. This work establishes that carbon cloth can be used to replace metal foils as a flexible current collector without sacrificing electrochemical performance.

Secondly, this thesis explores the use of a nitrogen-rich carbon foam based on the carbonization of melamine formaldehyde and graphene oxide for use in lithium-ion hybrid capacitors. The foam presented here can be used as-is as a flexible, free-standing, binder-free anode for lithium-ion hybrid capacitors/batteries. Furthermore, the foam can also be used as a 3-dimensional current collector for other active materials both in the anode and the cathode, which demonstrates its versatility for electrochemical energy storage systems. An all-carbon based lithium-ion hybrid supercapacitor has been fabricated using the foam as both an active material for the anode and the current collector for the activated carbon cathode. The cell shown in this chapter achieved an energy density of 40 Wh kg^{-1} which is superior to that reported in the literature that are based purely on carbon materials. The work presents a novel carbon-based flexible electrode material and concept device that also enables the removal of binders and current collectors from traditional batteries and supercapacitors, bringing us one step closer to achieving a fully flexible electrochemical energy storage system.

Finally, graphene quantum dots (GQDs) have been synthesized using a simple peroxide-assisted method. The GQDs are then electrodeposited onto carbon cloth to make an all-carbon, binder-free, flexible electrode for supercapacitors. This work builds off the TiO_2/carbon cloth composite by replacing the TiO_2 with a carbon-based nanomaterial. Presently reported research has involved the use of GQDs either in conjunction with another active material or used as an active material on rigid, planar substrates. We have shown that GQDs can function as a stand-alone active material for EDLC capacitors. At the time of writing, this work shows the first such use of GQDs on a non-planar, flexible substrate for supercapacitors.

All the work in this thesis centers around the use of carbon-based materials and their composites towards the development of flexible electrodes for lithium-ion batteries, supercapacitors and their hybrids. This thesis provides insights into the viability of using various carbon-based materials in different aspects of flexible electrodes and provides a basis for future investigations into this topic.

Acknowledgements

I would like to thank my supervisor, Prof. Aiping Yu, for her guidance and support during my PhD career. She has provided valuable guidance and trust the pursuit of different avenues of my research. I would also like to thank Prof. Zhongwei Chen for providing research guidance and laboratory space/equipment during my tenure here. I would also like to thank and acknowledge every single one of the researchers Yu/Chen group for helping my research in every way imaginable.

I would like to thank all of my friends for keeping my sanity throughout these years. I do not think that I could have done it without you all. Thank you for working out with me, thank you for being there when I needed you, thank you for providing me perspective and insight into my life that I could have never gotten myself. Even though I do not have space here to acknowledge every single one of you, know that you have affected life in ways that you may not have realized.

Thank you to my family for supporting me and believing in me throughout my educational journey. Thank you Mom and Dad for making countless trips of Waterloo to hang out and drop-off delicious home made food. Thank you to my sisters for giving me valuable experience and insight, even though you might not have known it.

Finally, I would like to thank my dog Koji for even though you're a relatively new addition to my life, you have provided me with endless joy and love in the final months of my PhD career.

Table of Contents

Table of Figures

Table of Tables

1.0 Introduction

Electrochemical energy storage systems have been at the forefront of research for the past few decades, spurred on by the growing demand and electrification of our society. Currently, the most popular technology for electrochemical energy storage is the lithium-ion battery (LIB) [1]–[9]. LIBs are present in just about every application in which electrical energy storage is involved, from grid/utility-level storage to mobile electrical storage. LIBs are attractive due to their high energy density and moderate power density. Another type of popular electrochemical energy storage system is the supercapacitor. Supercapacitors are a form of electrochemical energy storage which relies on the adsorption of ions onto the surface of high surface area materials. Supercapacitors can be thought of as opposites of LIB, possessing high power density and cycle lives while only possessing low to moderate energy densities. As such, supercapacitors are useful in applications where high power densities are needed and can also used in conjunction with LIBs.

Currently, most commercially available LIBs and supercapacitors have rigid formats, such as cylindrical and prismatic cells[6], [10]. Unfortunately, these rigid formats are unsuitable for applications where flexibility is key such as smart wearables and medical sensors. With the growing popularity of these devices, a pressing need exists to develop reliable, high performance flexible electrochemical energy storage systems to fulfill the demand [6], [11]–[13].

Flexible energy storage systems can be defined as any energy storage devices that can be bent, stretched, twisted, folded or compressed [10]. The two main barriers to the viability of flexible

energy storage systems are the lack of high-performance solid-state electrolytes and flexible electrodes. This thesis focused on the latter issue and address different strategies for the development of flexible electrodes using carbon-based active materials. In this thesis, active materials are defined as materials that are responsible for most of the electrochemical energy storage in a cell. For example, the active materials consist of graphite in the negative electrode and a $LiCoO_2$ (or a host of other transition lithium-rich transition metal oxides) in a LIB.

Currently, most commercially available LIBs or supercapacitors are made by casting a slurry of active materials and binders onto metal foils which are then packed together to form a cell. The slurry casting method allows for the deposition of a high amount of active materials but does not allow the cell to be flexible. The slurry pasted onto the metal foils tends to flake when subjected to repeated bending stresses. Moreover, the metal foils themselves eventually break due to the same reason. The two main strategies that can be employed to overcome this problem are the replacement of:

1. metal foil current collectors with a flexible current collector
2. current collectors with a free-standing, binder-free electrode

Carbon-based materials such as graphene, carbon nanotubes and carbon cloth have attracted much research interest in the area of electrochemical energy storage. Carbon-based materials have lower energy storage densities compared to metal oxides but they are widely researched due to their abundance, low-cost and environmentally friendly nature.

Graphene is a 2D carbon allotrope that has many interesting properties. Graphene has a very high electric and thermal conductivity in addition to excellent mechanical properties [14], [15]. It has also been shown to store lithium-ions well due to its high surface area to volume ratio

[16]–[22]. Due to these reasons, graphene and its derivatives have received much interest in the electrochemical energy storage field, especially for use in LIBs and lithium-ion capacitors (LIC). More recently, researchers have tried to fabricate rGO with different dimensionalities from 1D (fibrous) to 3D (foams) [18], [19], [23]–[32]. These forms of rGO are often flexible, making them perfect for use in flexible electrochemical energy devices.

1.1 Objectives

The objectives of this work are to: (i) explore the use of carbon-based materials as flexible electrodes in different electrochemical energy systems and (ii) design and fabricate flexible electrochemical energy storage devices based on carbon materials. More specifically, the following topics are examined:

1) Examination of the performance of carbon fiber cloth when used as a flexible current collector for an intercalation-type anode by
    a. demonstrating the viability of using carbon cloth to replace metal foils
    b. fabricating and testing the electrochemical performance of a carbon fiber cloth/TiO_2 composite as a free-standing, flexible anode in lithium-ion batteries/hybrid capacitors.
2) design and fabrication of a nitrogen-doped carbon foam for use in flexible electrochemical energy systems by
    a. optimizing the conditions for synthesis of a nitrogen-doped carbon foam/graphene composite as both free-standing electrode and flexible current collector for lithium-ion hybrid capacitors.
    b. evaluating the performance of the current collector-less hybrid capacitor.
    c. evaluating the use of composite foam in an EDLC supercapacitor system.

3) Synthesis of an all-carbon EDLC supercapacitor based on the electrophoretic deposition of graphene quantum dots (GQDs) onto carbon cloth by

   a. optimizing the synthesis parameters of GQDs to give the best performance

   b. optimizing the deposition parameters of GQDs onto carbon cloth

   c. evaluating the performance of a flexible EDLC cell under normal and flexed conditions.

Figure 1-1 summarizes the strategies employed in this thesis to develop next generation flexible electrodes in a flowchart.

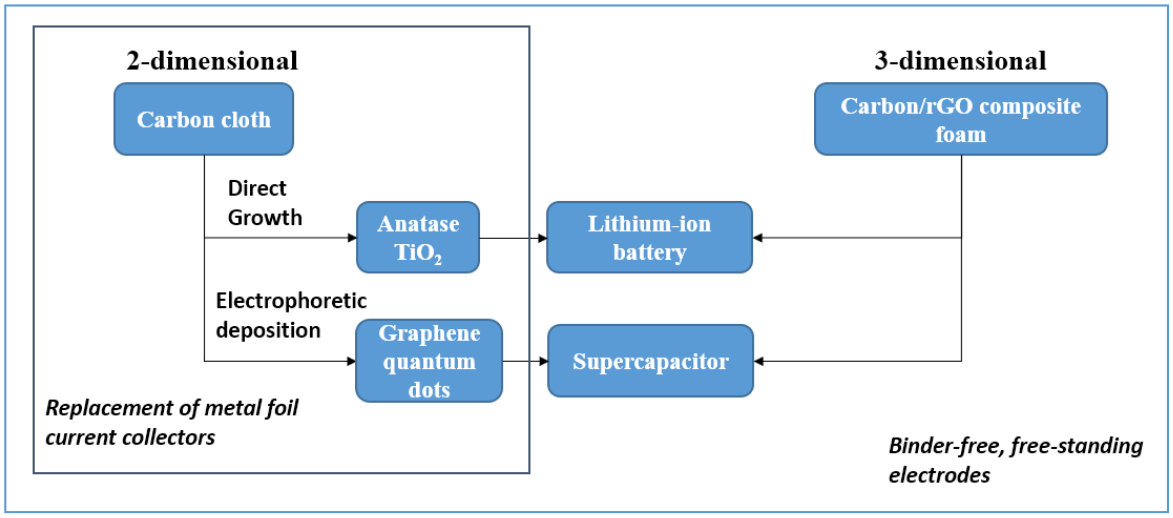

Figure 1-1 *Flowchart of experiments conducted in this thesis*

1.2 Thesis Organization

This work is organized in the following manner:

Chapter 1 gives a brief introduction to the topic of this thesis including its motivation and objectives. **Chapter 2** provides a brief overview into the field of electrochemical energy

storage, focusing specifically on lithium-ion batteries, supercapacitors, and their hybrids. Carbon-based materials will also be discussed briefly in order to give the reader a background understanding of their use in electrochemical energy storage systems. This is followed by an overview of the literature on the use of carbon-based materials in flexible electrochemical energy storage systems, subdivided into the shape and form of the electrodes. **Chapter 3** provides a description of the characterization and experimental techniques used in this thesis. **Chapter 4** presents work done on using carbon fiber cloth as a current collector for TiO_2 nanocrystals for use in flexible lithium-ion batteries. Carbon cloth was chosen due to its flexibility and electronic conductivity. TiO_2 was used as the active material in order to boost the lithium-ion capacity since carbon cloth has negligible lithium-ion storage capacities. Despite having excellent performance and flexibility, the low-surface area of carbon cloth limits the both the electrolyte accessibility to the surface and the available surface area for active material deposition. **Chapter 5** presents work done in order to overcome the low-surface area of carbo cloth as an electrode material. This work presents the synthesis of a nitrogen-doped carbon/graphene composite foam as a free-standing, binder free electrode for use in flexible lithium-ion hybrid capacitors and EDLC supercapacitors. Despite its excellent lithium-ion battery and supercapacitor performance, the fragility of the foam presents a roadblock for its use as a flexible electrode. We decided to revisit carbon cloth as a flexible electrode candidate and use it in an EDLC supercapacitor system. By choosing to use carbon cloth in an EDLC supercapacitor system, we can place less emphasis on the energy density of the electrode and focus on applications that focuses on flexibility and moderate to low energy densities such as smart wearable sensors. **Chapter 6** presents work on the synthesis and deposition of GQDs on carbon cloth for use in binder-free, flexible EDLC supercapacitors. In this work, we have shown

a flexible EDLC supercapacitor with extremely high rate capabilities that can be used in low-energy applications. **Chapter 7** summarizes the conclusions, contributions, recommendations and presents an outlook based on the work presented in this thesis.

2.0 Literature Review

2.1 Electrochemical Energy Storage

Electrochemical energy storage devices are an integral part of our energy future due to the rapid electrification of our society. Electrochemical energy storage devices are devices that utilize principles of electrochemistry in order to store energy from various sources for later use. There are many different types of electrochemical storage devices that are available, we focus on two popular types: lithium-ion batteries and supercapacitors, in this project.

2.1.1 Lithium-Ion Batteries

LIBs are a class of devices that utilizes the storage and transport of lithium ions to store energy. Current iterations of LIBs consists of a positive electrode, negative electrode, semi-permeable membrane separator and lithium-salt as the electrolyte. The negative electrode most commonly used is lithiated graphite, while the positive electrode usually consists of a transition metal compound such as lithium iron phosphate or nickel cobalt oxide. To charge a LIB, lithium-ions are driven into the lattice structure of graphite, forming a graphite intercalated compound (GIC). This intercalation process is controlled by the rate of solid state diffusion of lithium ions into graphite and proceeds at a relatively slow rate. The opposite process occurs when the LIB is discharged. The lithium ion is spontaneously driven out of the graphite lattice and this process releases electrons that travel through an external circuit. Due to the larger size of ithium ions compared to the spacing in the graphite lattice, the charge and discharge process stresses the graphite structure. This stress eventually causes the lattice to break down after several hundred of charge and discharge cycles, lowering the capacity of the LIB.

The half-cell reaction graphite can be expressed as the following [33]:

$$xLi^+ + \ x\,e^- + xC_6 \ \leftrightharpoons \ xLiC_6 \qquad (2\text{-}1)$$

x moles of lithium ions can be stored in every 6 moles of carbon atoms. The specific capacity of an electrode material is defined by:

$$Q = \frac{xF}{M} \qquad (2\text{-}2)$$

where Q is the specific capacity in mAh g^{-1}, x is the number of electrons transferred in the redox reaction, F is the Faraday constant in mAh and M is the molecular mass of the active species. For a perfect graphite lattice, x has a value of 1 and corresponds to a theoretical specific capacity of 372 mAh g^{-1}.

Figure 2-1 shows a typical first charge and discharge curve of a graphite half-cell where lithium is the counter electrode.

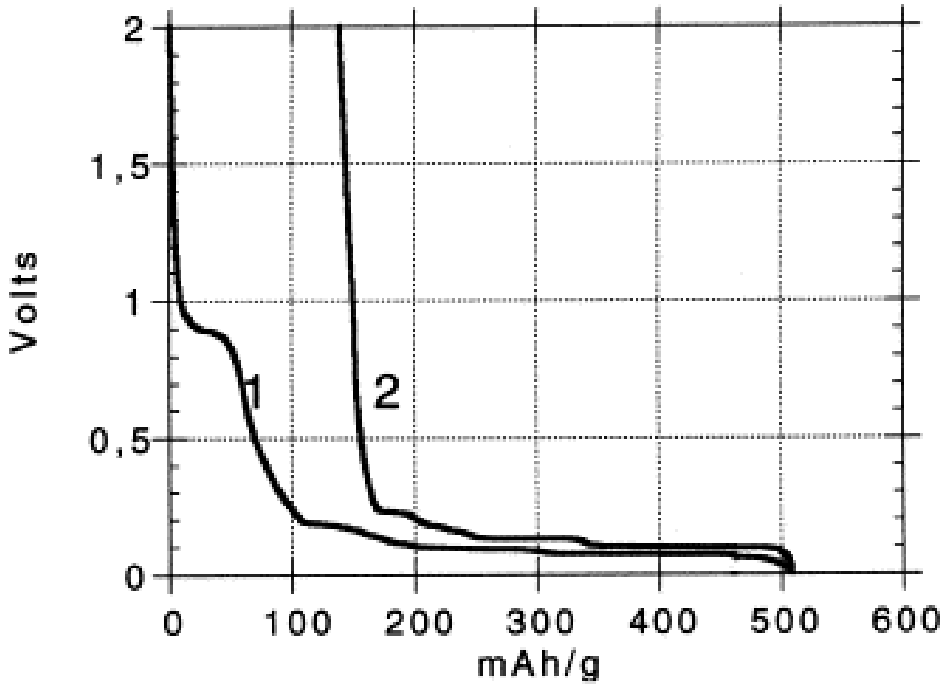

Figure 2-1 *First discharge (1) and charge (2) curve of a typical graphite half-cell [5]*

The first discharge of the graphite half-cell shows a voltage plateau at approximately 0.9 V which corresponds to an irreversible reaction whereby a solid electrolyte interphase (SEI) is formed. The SEI is a passivating layer resulting from the reaction between the electrolyte and the electrode which causes an irreversible capacity loss. Several plateaus can also be observed below 0.3 V. These plateaus are caused by the insertion of Li^+ ions into the graphite electrode. As shown in the curve, lithium insertion into graphite occurs in multiple stages, corresponding to the number of graphene layers between two successive intercalation layers [5]. The process of insertion/de-insertion is a thermodynamically driven process that depends on the energy to widen the gap between graphene layers. Although graphite is currently the standard anode material for LIBs, it has its own challenges and problems. First, the lithium diffusion rate in carbon (and non-nanostructured carbonaceous materials in general) is sluggish having a rate of between 10^{-12} to 10^{-6} cm s^{-1} [34], [35] which results in lower power densities. Second, graphite experiences a large volume change when lithium intercalates and de-intercalates from its structure which results in a structural and capacity degradation over time [36].

2.1.2 Supercapacitors

Supercapacitors or electrochemical capacitors are a type of electrochemical energy storage system that relies on the electric double layer phenomena and/or pseudocapacitance to store charge. Electric double layer capacitors (EDLCs) store charge through the reversible accumulation of charged species on the surface of an electrode when a potential is applied. **Figure 2-2** shows a graphical illustration of the mechanism of an EDLC.

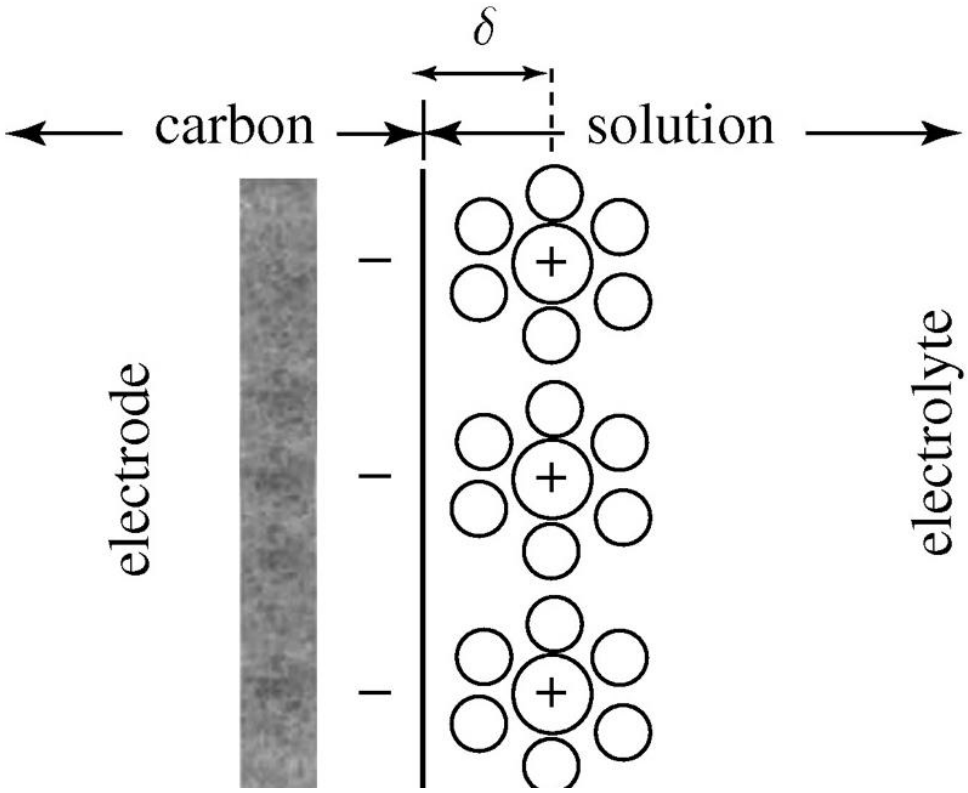

Figure 2-2 *Illustration of the mechanism of EDLC capacitance [37]*

During charging, the ions will travel to the negative and positive electrodes respectively. These ions form a Helmholtz double layer on the surface of the electrodes with no Faradaic charge transfer. When the EDLC is discharged, the opposite happens and the accumulated electrons will flow through the external circuit through the load. This process happens on a very short time scale since it only relies on the mass transport of the electrolytes to the surface of the electrodes. Furthermore, no reaction or phase change occurs on the electrodes, the durability of supercapacitors is much longer compared to LIBs [37], [38]. The capacitance of an EDLC can be expressed as [39]:

$$C = \frac{\epsilon_r \epsilon_0 A}{d} \qquad (2\text{-}3)$$

where ε_r is the pemittivity of the electrolyte, ε_0 is the permittivity of the vacuum, A is the surface area of the electrodes, and d is the thickness of the Helmholtz double layer. From the equation, the capacitance of an EDLC can be increased by increasing the available surface area of the electrode. This can be achieved by a variety of strategies such as controlling the nanostructure of the electrode's surface and increasing the amount of electrolyte that have access to the surface of the electrode.

Another type of supercapacitor is the pseudocapacitor. Pseudocapacitors have a fundamentally different principle operation compared to EDLCs and are more similar to LIBs. Pseudocapacitors store charge through fast Faradaic reactions on the surface or sub-surface of an electrode. Pseudocapacitance can roughly be divided into 3 main categories: underpotential deposition, redox and intercalation. **Figure 2-3** shows an illustration of the 3 categories of pseudocapacitance.

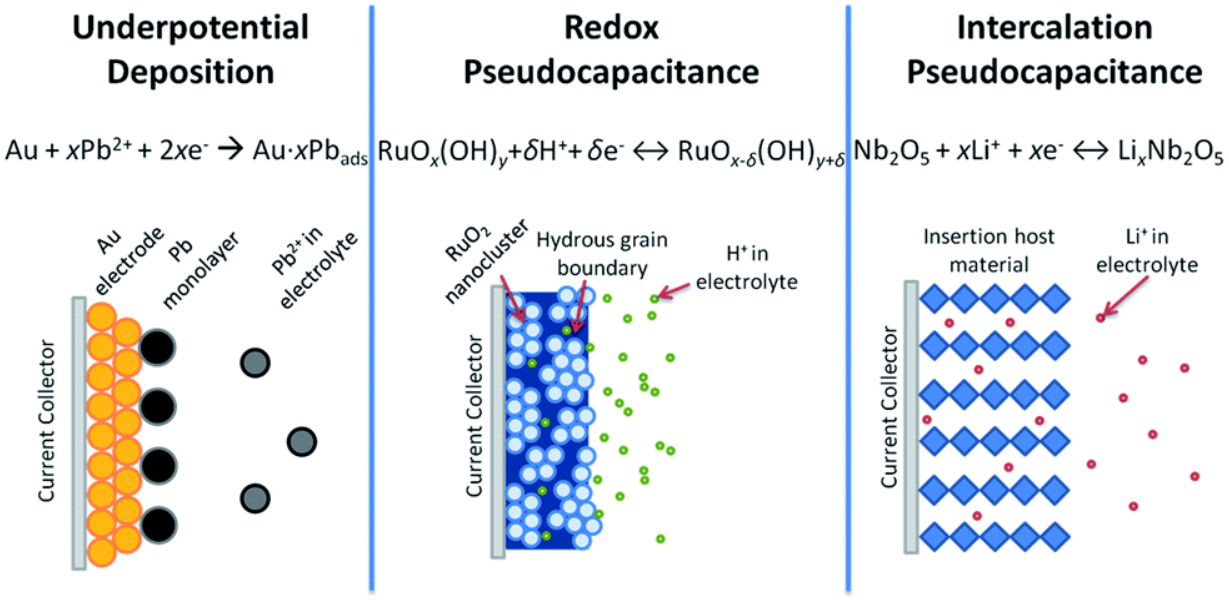

Figure 2-3 *Illustration of 3 main mechanisms of pseudocapacitance [40]*

Underpotential deposition occurs when a more favourable interaction exists between the active material and the substrate than between the active species molecules themselves. This happens because the deposition potential of the species to the surface of the active material is more positive than the Nernst reduction potential of the species. Redox pseudocapacitance occurs when a charged species is adsorbed onto or near the surface of an active material and a Faradaic charge transfer occurs. Intercalation pseudocapacitance occurs when a charged species intercalates into the crystalline layers of an active material and a charge transfer reaction occurs without a corresponding phase change. Although the aforementioned processes also occur in LIBs, they are faster because they only occur on the surface of a few nanometers below the surface of the electrode. Thus these processes, unlike the ones in LIBs, are not constrained by solid state transport [40]. Furthermore, since the processes do not induce a phase change, the electrodes have a higher longevity compared to ones in LIBs [18], [33], [40]. The capacitance of a pseudocapacitor can be expressed as [40]:

$$C = \frac{(nF)X}{mE} \qquad (2\text{-}4)$$

where n denotes the number of electrons transferred in the reaction, F denotes the Faraday constant, X denotes the fraction of the electrode surface covered by the adsorbed species, m denotes the molar mass of the active material and E is the potential at which the reaction occurs. Similar to EDLCs, the simplest way to increase the capacitance of a pseudocapacitor is to increase the available surface area of the electrode for ions to adsorb and react.

Both EDLCs and pseudocapacitors are relatively simple to fabricate, consisting of 2 electrodes, a semi-permeable membrane separator and an aqueous or organic electrolyte. Since the capacitance is directly related to the number of adsorbing ions, the surface area of the electrodes plays a huge role in determining the performance of the device. Usually, supercapacitors utilize

the same active materials in both electrodes. These supercapacitors are often referred to as symmetric supercapacitors. Supercapacitors with different active materials in the electrodes are referred to as asymmetric supercapacitors.

Asymmetric capacitors usually combine pseudocapacitative or battery-type active materials in one electrode and a double-layer active material on the other [28], [41], [42]. This allows the device to have both high power and energy densities. Due to the combination of pseudocapacitance/regular redox electrodes and double-layer electrodes, these capacitors are often referred to as hybrid supercapacitors. One such example is the lithium-ion capacitor (LIC) or lithium-ion hybrid supercapacitors. LICs are a relatively recent development that combines both adsorption electrode materials with intercalation electrode materials [18], [43]–[49]. LICs can be made with either a positive EDLC material, such as activated carbon, and a negative intercalation material, such as graphite, or vice versa. The most common LIC configuration currently being studied is the former. **Figure 2-4** shows a schematic illustration of the operation of a LIC with a positive EDLC-type electrode and a negative intercalation electrode.

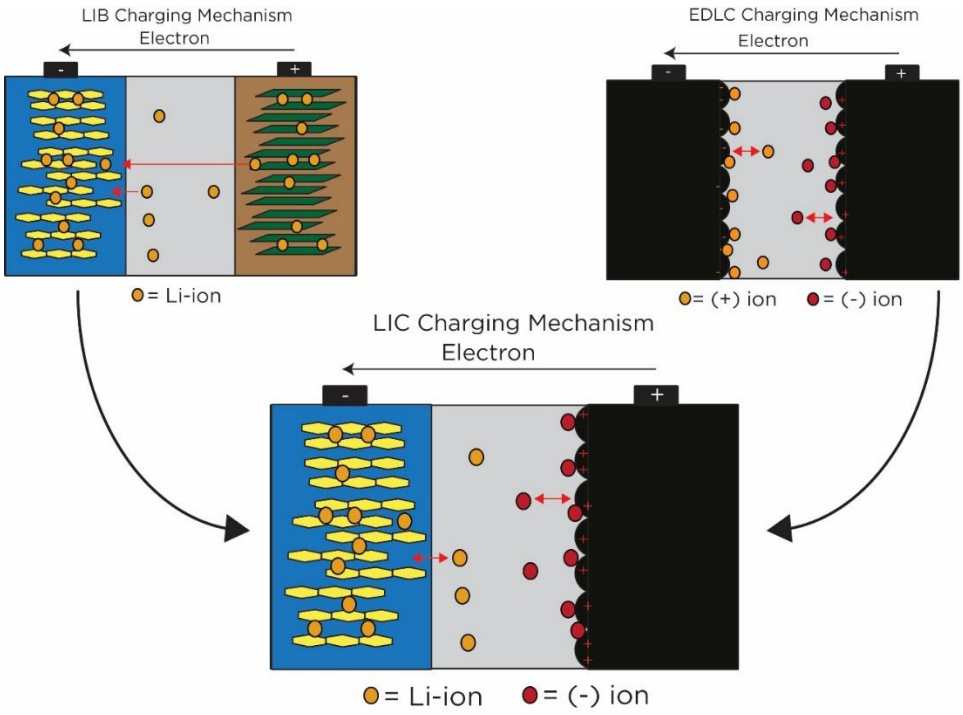

Figure 2-4 *Schematic illustration of the operation mechanism for one type of lithium ion capacitors*

Current commercially available LICs are made with an activated carbon (AC) positive electrode and a negative graphite electdode [33], [50]. Nevertheless, improvements to both the positive and negative materials can still be made. Since the intercalation process at the negative electrode is much slower than the adsorption/desorption process at the positive electrode, the negative electrode dictates the power characteristic of the whole device. On the reverse side, the energy density of the device is dictated by the energy density of the positive material since the negative material usually has higher energy density. Various carbon materials have been explored for use to address these issues in LIC. Zhang et al. explored the use of different hard carbon materials for use in LIC and found that using hard carbons in LIC can improve the power density of the overall device, achieving a power density as high as 7.6 kW kg^{-1} while still

retaining a high energy density of ~87 Wh kg^{-1}[51]. They found that the increased layer spacing in hard carbons compared to graphene can facilitate the diffusion of lithium-ions in and out of the structure, allowing for faster charge/discharge rate which is directly related to the power density of the device.

2.2 Carbon-Based Materials in Electrochemical Energy Storage Systems

2.2.1 Graphene

Graphene is an allotrope of carbon that has received a great deal of attention recently especially in the electrochemical energy storage field due to its mechanical and electronic properties. Graphene consists of a network of sp2 bonded carbon atoms that forms 2-D layers with single atom thickness. **Figure 2-5** shows TEM and SEM images of a representative graphene sample. The wrinkly nature of the graphene, which gives it a high surface area is clearly evident.

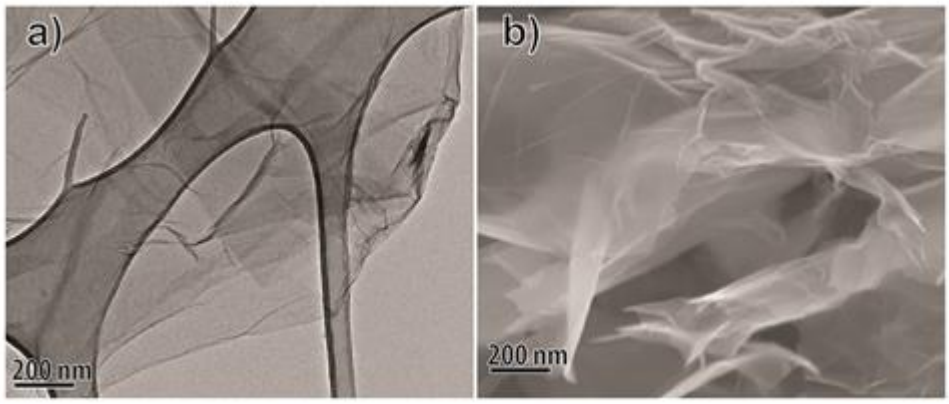

Figure 2-5 *Representative TEM (left) and SEM (right) images of graphene [52]*

Similar to graphite, graphene has the capability to store lithium-ions. However, graphene has been shown to have capacities exceeding the value of 372 mAh g^{-1} [21], [53], [54]. The high lithium storage capacity of graphene may be attributed to the difference in interaction between the graphene sheets and lithium. In normal graphite, the maximum lithium content corresponds

to a stoichiometry of LiC_6 while the stoichiometry in graphene sheets can range from LiC_3 to LiC_2 [55]–[60]. **Figure 2-6** shows a schematic illustration of the "house of cards" model that Dahn et al proposed [59]. Dahn proposes that graphene has a higher capacity compared to graphite because lithium ions can be stored on both sides of the graphene surface, corresponding to the stoichiometry of LiC_3 and theoretical capacity of 740 mAh g^{-1}. The second stoichiometry LiC_2, which corresponds to a theoretical capacity of 1115 mAh g^{-1}, has been shown by Pan et al to arise from the effects of edge and other defects present in the imperfect rGO lattice [55]. Based on the I_D/I_G ratios obtained from Raman spectroscopy, Pan et al shows that the greater the disorder present in the lattice, the greater the reversible capacity of the rGO. They theorized that the enhanced capacity is caused by 2 effects: the increased interlayer spacing caused by the functional groups in rGO and the presence of defects (sp3 bonded carbon atoms, dangling bonds, vacancies, etc.) on the edge and surfaces of individual graphene sheets [55].

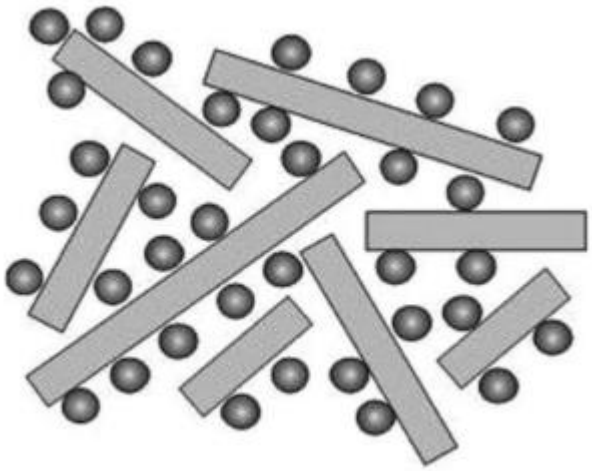

Figure 2-6 *"House of cards" model for lithium-ion storage in graphene proposed by Dahn et al [59]*

Graphene Production

Many pathways can be used to synthesize graphene. In this study, the main focus will be on preparing graphene through chemical synthesis. The most popular chemical route for graphene synthesis is through the oxidation of graphite to form graphene oxide (GO) followed by subsequent reduction to graphene. The oxidation of graphite introduces functional groups on the surface of the carbon lattice, breaking their perfect structure. This results in numerous defects, depending on the degree of oxidation. However, these functional groups make GO hydrophilic making it easier to process in various solvents. The reduction of GO to graphene is often imperfect, leaving behind functional groups and defects on the surface of the sheets. Consequently, graphene produced using this method is usually called reduced graphene oxide (rGO) instead of graphene. The number of defects and functional groups present in the final product can be tuned using different reduction methods. Although the rGO produced in this way is less pristine than graphene produced via other methods, such as chemical vapour deposition (CVD) or mechanical exfoliation, they have their own advantages. First and foremost, the production of rGO via the chemical exfoliation of graphite is cheaper and more scalable than methods such as CVD [15]. The surface properties of the resulting product can also be easily tailored by careful control of oxidation and reduction conditions [61]. Furthermore, the conversion rate of graphite to rGO is relatively high compared to other production methods. The drawbacks of the chemical exfoliation method is the presence of harmful by-products in the waste stream. However, these harmful by-products can be reduced or recycled for other processes.

The most popular method of producing rGO from graphite involves the use of the modified Hummers' method. The Hummers' method produces GO by oxidizing graphite in strong acids,

which also tends to separate them. In the modified Hummers' method, H_2SO_4 and $KMnO_4$ are used. H_2SO_4 intercalates into the lattice structure of graphite, forming an intermediate compound. At this point, the graphite is still pristine and no phase changes have occurred [62]. $KMnO_4$ is primarily responsible for the oxidation of the graphite to GO. The oxidation of graphite moves from the outside in as $KMnO_4$ diffuses further into the lattice of graphite. This process happens relatively slowly at a rate that depends on the lateral size of the graphite sheets. A schematic illustration of this process is shown in **Figure 2-7**. The subsequent addition of water allows for the complete exfoliation of the GO sheets, which are still tightly bound and stable up to this stage.

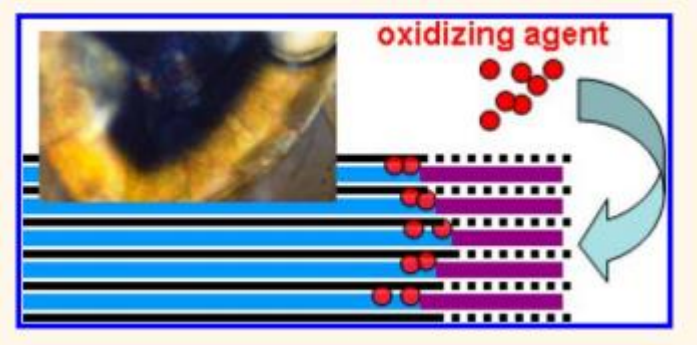

Figure 2-7 *Schematic illustration for GO formation [62]*

Typically, the result of the chemical exfoliation process is rGO powder. However, different forms of rGO can be formed by manipulating the GO structure before it is reduced to rGO. The modifications to GO and rGO can be categorized by the 3dimensional structure of the final product. The 3 categories are: rGO fibers (1-dimensional) [27], [29], [63]–[67], rGO film (2-dimensional) [24], [54], [68]–[70] and rGO foam (3-dimensional) [28], [71]–[80]. For the purpose of convenience, the term rGO and graphene will be taken as equivalent from this point on and used interchangeably.

2.2.1 Graphene quantum dots

Graphene quantum dots (GQDs) are a relatively new class of material derived from graphene. Strictly speaking, GQDs are single atomic layers of graphene sheets with a lateral size of less than 50 nm[81]–[84]. However, in practice, most GQDs consist of more than one layer of graphene sheets with oxygen and hydrogen containing functional groups on the surface stacked together with a lateral size of lower than 10 nm. Due to the presence of these surface functional groups and the quantum confinement effect, GQDs can have a range of tunable bandgaps from 0 eV – 6 eV [85]. The bandgap of GQDs depends on its lateral size and the type and number of functional groups present on the surface. GQDs are attractive compared to other semi-conductor quantum dots due to their low toxicity, stable photoluminescence and water solubility[82], [84], [86]. Previous studies have focused on exploring the applications of GQDs photoluminescence [86]–[91]. However, a limited number of works has also exploited the transparency and high surface area of GQDs for display and energy storage technologies. Most of the work that deal with GQDs in flexible energy storage can be broadly separated into two categories: using GQDs in conjunction with other active materials in EDLC systems and using GQDs by itself in micro-supercapacitor systems [87], [92]–[94]. Due to their electronic conductivity and high specific surface area, GQDs are an ideal candidate for use as active materials in EDLC or as an additive to improve electronic conductivity. Mondal et al. developed a composite material derived from doped polyaniline and GQDs with a specific capacitance of approximately 1044 F g^{-1} at a current density of 1 A g^{-1} [95]. Liu et al. synthesized GQDs using a solvothermal method from GO and used it to fabricate a symmetric microsupercapacitor. The supercapacitor was assembled by electrodeposition of GQDs, shown in **Figure 2-8**, onto interdigitated gold electrodes and achieved a high areal capacitance of 468.1 uF cm^{-2} [92].

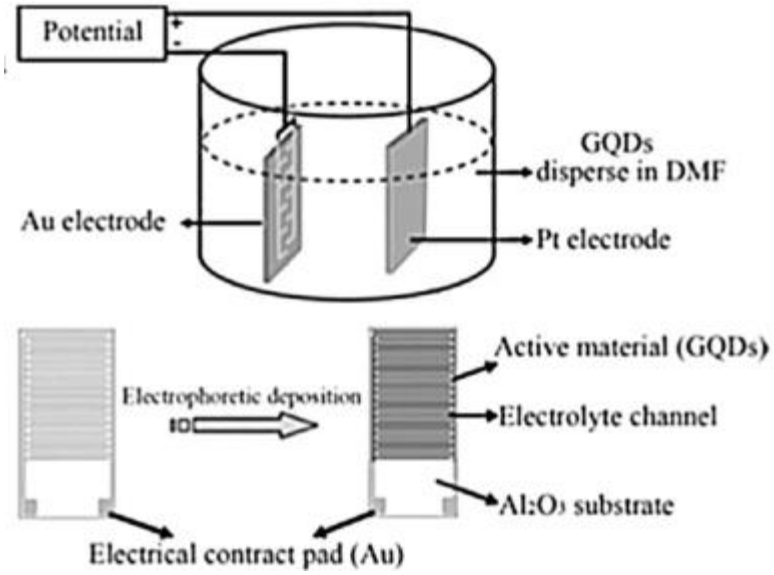

Figure 2-8 *Schematic Illustration of the electrodeposition of GQDs on the interdigitated gold electrodes [92]*

A limited number of reports have also focused on the use of GQDs in lithium-ion batteries. Ruiyi et al. synthesized a lithium titanate and nitrogen/sulfur co-doped GQDs and used it as an anode material for LIB. The GQDs was expected to enhance electron transfer and managed to improved the capacity of the LTO anode to 254.2 mAh g^{-1} at a discharge rate of 0.1 C [96]. To this date, there is little on the usage of GQDs as a standalone active material in flexible EDLC, which is addressed later in this thesis in **Chapter 6**.

GQDs Production

As with most nanomaterials, 2 strategies have been used to produce GQDs: top-down and bottom-up approaches. One bottom-up approach involves the assembly of small carbon molecules to form monodispersed GQDs with controllable sheet sizes[82]. This method is attractive because of the high degree of control, but requires a high degree of precision in reaction conditions in order to achieve the desired results. Another bottom-up approach is the direct carbonization of the small organic molecules. This method is simpler, requiring less

complicated steps but is less precise resulting in GQDs that are more polydisperse. In general, bottom-up approaches are usually more complicated and have low yields when compared to top-down approaches.

Although bottom-up approaches allow more precise size control, top-down approaches are the most popular methods of producing GQDs due to the ease of synthesis and scalability. Many top-down approaches can be used, but the general strategy is to break down "bulk" carbonaceous materials such as graphene, CNT, graphite, into smaller pieces using various chemical and physical methods. The most widely used top-down method is the oxidative cleavage method whereby oxidizers such as HNO_3 and H_2SO_4 break down the carbon-carbon bonds in the bulk material to obtain GQDs. Another popular method of producing GQDs is the hydrothermal/solvothermal method. This method uses high pressure and temperature in combination with various solvents in order to break down the carbon materials. The carbon materials used must be oxidized first before they can undergo cutting via the hydro/solvothermal reaction. Thus, the most common carbon material used in conjunction with this method is GO. It is expected that GO can be formed into GQDs because of the linear epoxy and carbonyl defects present on the surface that can be readily cleaved at high pressures and temperatures [85]. A schematic illustration of this process is shown in **Figure 2-9**.

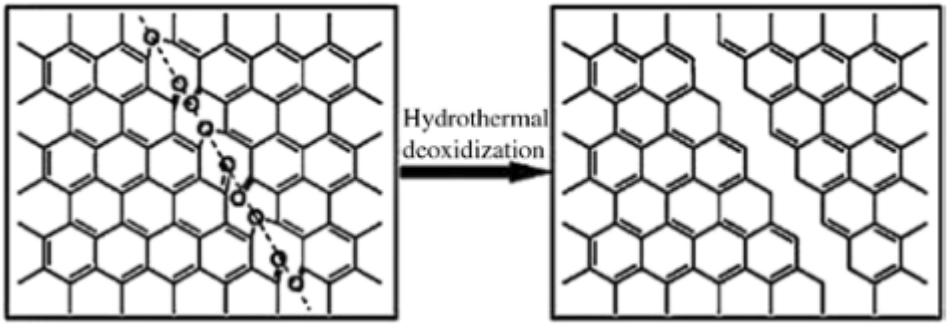

Figure 2-9 *Proposed Cutting Mechanism of GO into GQDs [85]*

H_2O_2 is also often added in order to increase the concentration of OH and O radicals that can attack these defect sites in GO and effectively cleave it into GQDs. Other less used GQDs production methods include ultrasonic/microwave exfoliation, chemical vapour deposition (CVD), electrochemical exfoliation and laser ablation [81], [82].

The current challenge with GQD production lies in the difficulty in synthesizing monodisperse GQD with high yields and low cost. Current methods shown in literature have succeeded at synthesizing GQDs that are monodisperse but have low yields and vice versa. As GQD is relatively new and is in the research phase, these methods for GQD production are acceptable. However, for GQDs to be a viable alternative as an active material, these production challenges have to be overcome.

2.3 Flexible Carbon-Based Electrochemical Energy Storage

Current electrochemical energy storage devices such as batteries and supercapacitors are commonly only available in rigid formats such as coin or cylindrical pouch cells. Even devices that are marketed as "polymer cells", which imply flexibility, cannot be bent and flexed without breaking [11], [13], [26]. The 2 main challenges that needs to be solved in order to reach a fully flexible device are the development of:

1. mechanically robust, flexible and high performance electrodes
2. high performance solid-state electrolytes

In conventional battery or supercapacitor electrode construction, the active materials are mixed in a slurry alongside binders and conductive agents before being pasted onto a metal foil current collectors. Despite the use of binders, the contact between the active material and the current collector is not strong enough to withstand the bending stresses without cracking or

delaminating, especially after repeated bend cycles. Furthermore, the metal foil itself cannot withstand repeated bending without breakage. Current devices also utilize liquid electrolytes, which pose a safety hazard if spilled. Therefore, the packaging of the device needs to be relatively robust in order to prevent leakage, which in most cases leads to an inflexible structure. For a fully flexible device to be realized, a concerted effort must be made to develop both electrodes and electrolytes that can be deformed repeatedly.

Among the most important components in any electrochemical energy storage system are the electrodes that make up the cathode and the anode. These are the materials responsible for storing and discharging the electrochemical energy in a storage device. As stated previously, current methods of producing electrodes for both LIBs and SCs involve mixing the active materials into a slurry along with polymeric binders (PVDF, PTFE, LDPE, etc.) and conductive agents (usually carbon-based materials such as carbon black or graphite). This active material slurry is then pasted onto a current collector in the form of a foil. Due to the way the electrodes are fabricated, repeated flexing or stretching will delaminate the active material layer from the current collector [10]. Much research has been put into developing new ways of fabricating electrodes that do not deteriorate mechanically and electrochemically when subjected to repeated physical deformation. Various approaches have been used to produce a flexible electrode architecture such as film/paper, cloth-like, fibrous/cable and foam structures, each with their own advantages and disadvantages. The next sections will give a brief overview of the different types of flexible electrode architectures that have been reported.

2.2.1 Planar Film/Paper Electrodes

Many attempts have been made to fabricate flexible electrodes using a free-standing membrane made from active materials. These electrodes are typically made with carbonaceous

nanomaterials such as CNT and graphene or conductive polymers such as PANI or PAN that has been formed into membranes. One of the earlier examples of paper-like flexible electrodes for electrochemical energy storage was investigated by Wallace et al in 2010 [16]. They prepared stable aqueous dispersions of graphene from commercial graphite and then used vacuum filtration in order to make graphene paper. The graphene paper was then used as the negative electrode for a LIB with a reversible capacity of 84 mAh g^{-1}. Our group has developed a graphene-film based electrode for EDLC supercapacitors. Davies et al fabricated a 25-nm transparent graphene film that had a specific capacitance of 135 F g^{-1} [70]. The major drawback of graphene in films is their low available surface area due to the compactness of the stacked layer. This leads to a non-ideal performance. To mitigate this, spacers have been used in order to open up regions between the layers for electrolyte access [26], [97]–[100]. For example, Wang et al. (2011) used carbon black nanoparticles in between layers of graphene in order to make a flexible graphene paper electrode (**Figure 2-10)** [100]. The carbon black nanoparticles prevent the graphene sheets from re-stacking due to Van der Waals interaction and successfully increased the capacitance by 700% over the non-carbon black-containing graphene paper.

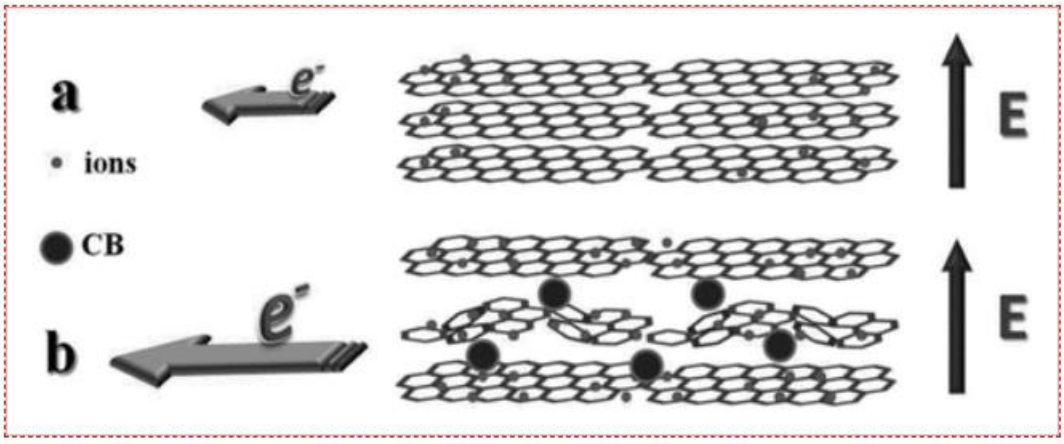

Figure 2-10 Schematic showing carbon black nanoparticles as a spacer to prevent restacking in graphene paper [100]

CNTs have also been used similarly to graphene. Cui et al fabricated free-standing CNT paper by first forming a CNT film on the surface of a stainless steel substrate shown in Figure **2-11** [11]. They then coated the surface of the CNT surface with lithium titanate (LTO) which is a common metal oxide used in LIB anodes. The subsequent composite CNT/LTO film was then peeled off and used as a free-standing electrode. The initial discharge capacity of the composite electrode was 147 mAh g^{-1}. They used the same method in order to make the cathode with lithium cobalt oxide (LCO) instead of LTO. The two electrodes were then laminated onto a piece of paper and sealed in a PDMS pouch to make a flexible full cell with a width of ~300 μm (**Figure 2-11)**.

Figure 2-11 *Flexible paper-like, CNT based supercapacitor. Reprinted (adapted) with permission from [11]. Copyright 2010 American Chemical Society*

Planar electrodes have also been used recently in microsupercapacitors, a type of electrochemical energy storage device characterized by their small, sometimes flexible, construction [92], [93], [101]–[104]. Microsupercapacitors are typically used to power small-scale electronics such as microelectromechanical systems (MEMS) and microsensors.

2.2.2 Cloth-like Electrodes

Cloth-like electrodes have similar 2-dimensional forms to paper/film electrodes. However, they are usually made from both natural and artificially occurring woven fibers. The simplest method

for fabricating cloth electrodes is to take pre-existing textiles such as cotton and coating them with conductive materials such as CNT or graphene [105], [106]. The conductive coating transforms the insulating substrate into a flexible, conductive one. As with paper electrodes, Cui et al. demonstrated that a fabric electrode can be made by taking CNT ink and painting it onto a polyester cloth [107]. This composite is not only flexible but also exhibited large electronic conductivity and porosity. Cui et al. used this CNT/cloth composite to fabricate stretchable SCs with a specific capacitance of 60 F g^{-1} even after stretching (**Figure 2-12)**.

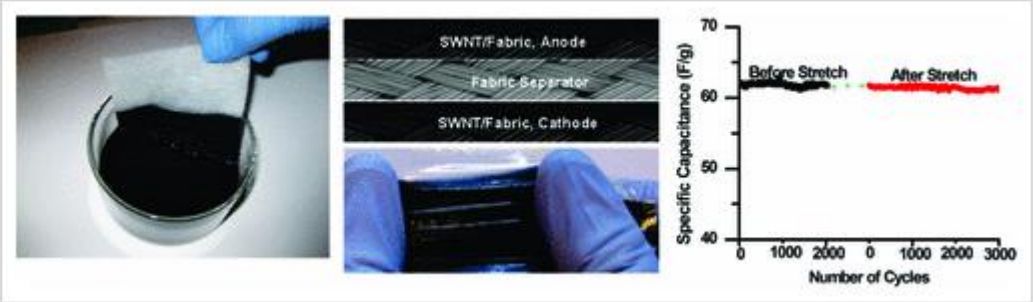

Figure 2-12 *Stretchable, cotton/CNT composite supercapacitor CNT based supercapacitor. Reprinted (adapted) with permission from [107]. Copyright 2010 American Chemical Society*

Liu et al. used a combination of PANI, cellulose fiber paper and rGO to develop a flexible electrode for supercapacitors through a simple dip coating method [108]. **Figure 2-13** shows a schematic illustration of their fabrication process.

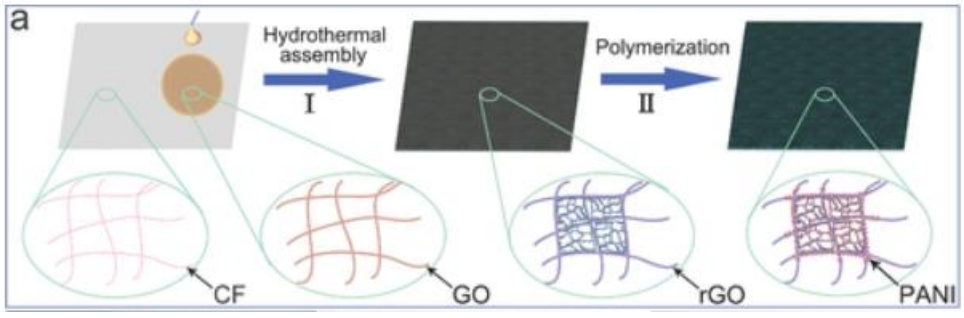

Figure 2-13 Fabrication process for PANI/Cellulose/rGO composite electrode[108]

First, they dip-coated a piece of cellulose paper in GO solution until it was saturated. Then GO was reduced to rGO by using a simple hydrothermal method. They also electrochemically deposited PANI on top of the rGO layer to boost the capacitance of the electrode. They fabricated a flexible EDLC capacitor which was able to reach a capacitance of 292 F g^{-1}.

Carbon fiber cloth has also been extensively used as a flexible current collector for LIBs and SCs due to its excellent electrical conductivity, mechanical robustness, corrosion resistance, low-cost and ease of production. Despite these properties, pristine carbon fiber has low capacitance which limit its applications as a free-standing electrode and is typically used as a current collector for other materials with high capacitance or capacity such as transition metal oxides or carbonaceous nanomaterials [109]–[114]. Research has also been conducted into improving the electrochemical activity of pristine carbon fiber cloth. One of the main ways of increasing its electrochemical activity is by increasing its specific surface area using various treatments[115]–[118]. Wang et al. boosted the capacitance of pristine carbon fiber cloth by conducting a simple electrochemical activation treatment [115]. Their process involved the electrochemical oxidation of of carbon fibers immersed in a mixture of HNO_3 and H_2SO_4 by applying 2V. The treatment etched the surface of the carbon cloth which roughened and increased the area of its surface. The oxidative treatment also introduced oxygen functional groups on the surface which allowed it to exhibit pseudocapacitative behaviour. These two factors allowed the carbon cloth to achieve an extremely high areal capacitance of 1.56 F cm^{-2}, a ~1700-fold increase over that of pristine carbon cloth.

2.2.3 Fibrous/Cable Electrodes

Fibrous/cable electrodes are attractive for flexible battery applications due to their inherent omni-directional flexibility. The shape also allows for configurations that planar electrodes

simply cannot attain. One of the very first fibrous/cable type batteries was made by Kim et al (**Figure 2-14**) [119]. Their design involves the twisting of several anode strands into a hollow core fiber structure with a tubular outer cathode coating. The anode strands were made by coating a strand of thin copper wire with a Ni-Sn composite. The use of the hollow core fiber structure allows greater penetration of the electrolyte solution which leads to a more consistent performance. This novel design allowed for unprecedented flexibility, allowing the battery to function even under extreme twisting and bending conditions.

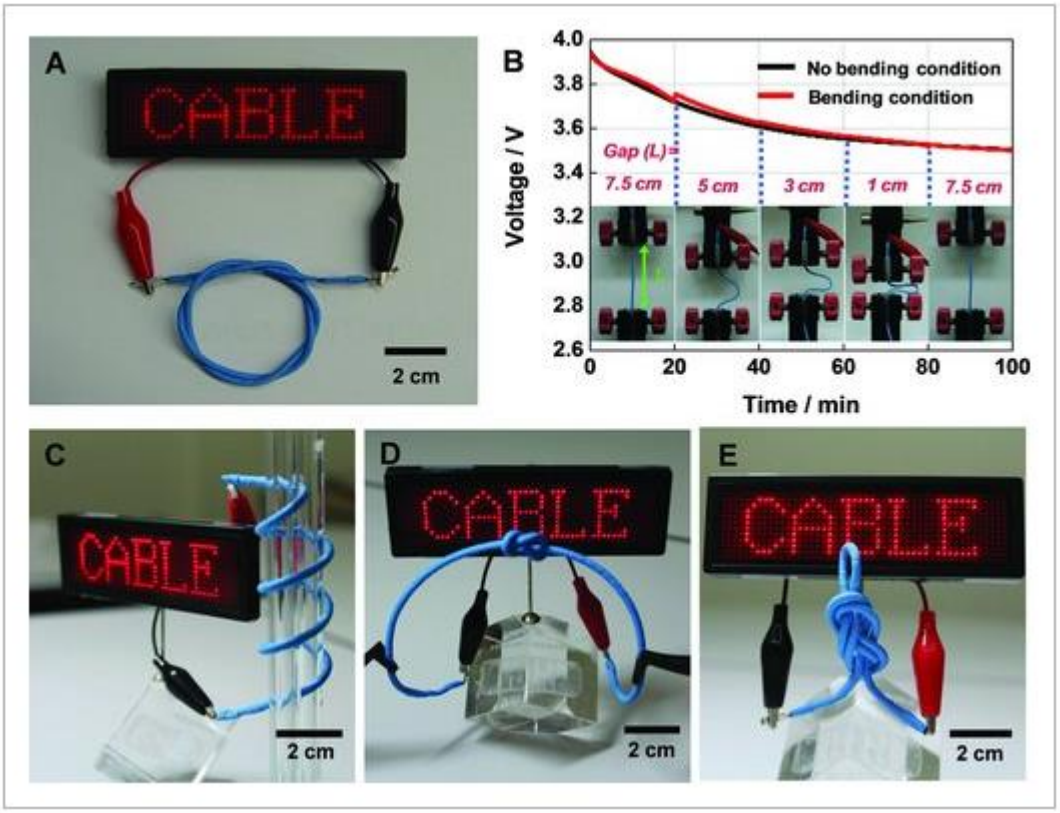

Figure 2-14 *Cable-type flexible LIB [119]*

Recently, wet-spun graphene was also shown to be a suitable alternative for fiber type batteries. Gao et al are pioneers of wet-spinning graphene into fibers [27]. In 2013, they made a parallel strand SC made from two parallel strands of graphene fibers and liquid electrolytes. Since then, Gao et al have improved their SC design by introducing a coaxial all-in-one device made from graphene and a polymer sheath as the separator (**Figure 2-15)** [29]. Their coaxial SC achieved a high areal capacitance of 204 mF cm^{-2} and a relatively high gravimetric capacitance of 185 F g^{-1}.

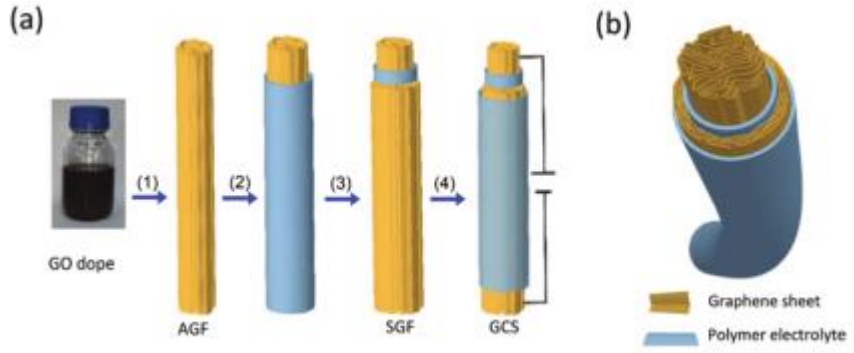

Figure 2-15 *Coaxial graphene fiber supercapacitor [29]*

Individual carbon fiber strands can also be utilized as current collectors for fiber-type electrochemical energy storage devices. Yadav et al. used carbon fiber strands in conjunction with lithium iron phosphate (LFP) and lithium titanate (LTO) to make a fibrous lithium-ion battery[120]. **Figure 2-16** shows a schematic illustration of the fabricated fibrous lithium-ion battery.

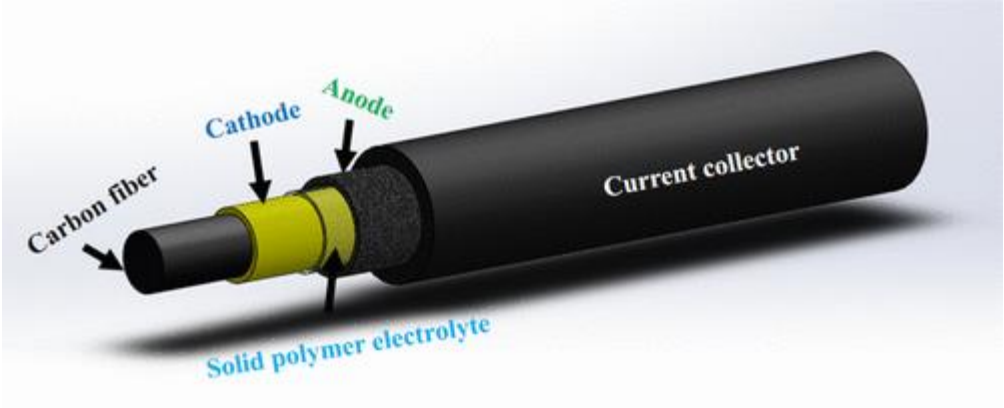

Figure 2-16 *Fibrous Lithium Ion Battery. Reprinted (adapted) with permission from [120]. Copyright 2019 American Chemical Society*

They achieved this by first coating a strand of carbon fiber with LFP through electrophoretic deposition. Then, a polymer electrolyte (polyethylene oxide, PEO, with a lithium salt) was coated via a simple dip method. Finally, the LTO anode and current collector (MWCNT, carbon black and PEO) were electrophoretically deposited as the final layer. The resulting flexible lithium-ion battery exhibited a discharge capacity of 4.2 μAh cm^{-2} at a current density of 13 μA cm^{-2} with a 85% capacity retention after 100 cycles. Although the capacity is low, this work shows a promising pathway for the fabrication of flexible, fiber-type batteries.

2.2.4 Foam Electrodes

Foam-type electrodes have also been explored as an option for flexible electrochemical energy storage. These electrodes are comprised of a 3-dimensional interconnected network usually comprised of carbonaceous materials. One of the most studied foam-electrode system is the graphene foam [23], [28], [31], [53], [71], [72], [121]–[126]. Graphene foam consists of a three-dimensional network of graphene sheets that is flexible, highly conductive and lightweight. Graphene foam is attractive because it has been shown to prevent re-stacking of the graphene sheets into graphite [53]. It also provides a high specific surface area and fast electron transfer

kinetics due to the interconnected graphene network [28], [123]. Its surface area is also advantageous when trying to incorporate other active materials on the surface in order to increase its electrochemical energy storage capabilities. Many studies have shown the use of graphene foams as conductive hosts for other active materials such as metal oxides [23], [28], [71], [126]. Fan et al used a graphene foam grown by chemical vapour deposition (CVD) as a support for Fe_3O_4 [71]. A schematic illustration of their process is shown in **Figure 2-17.** The CVD grown graphene foam has excellent electrical conductivity which facilitated the efficient transportation of both ions and electrons. The high surface area of the foam also allowed for a high loading of Fe_2O_3 with intimate contact. The resulting composite electrode had a stable reversible capacity of ~780 mAh g^{-1} for 500 charge and discharge cycles.

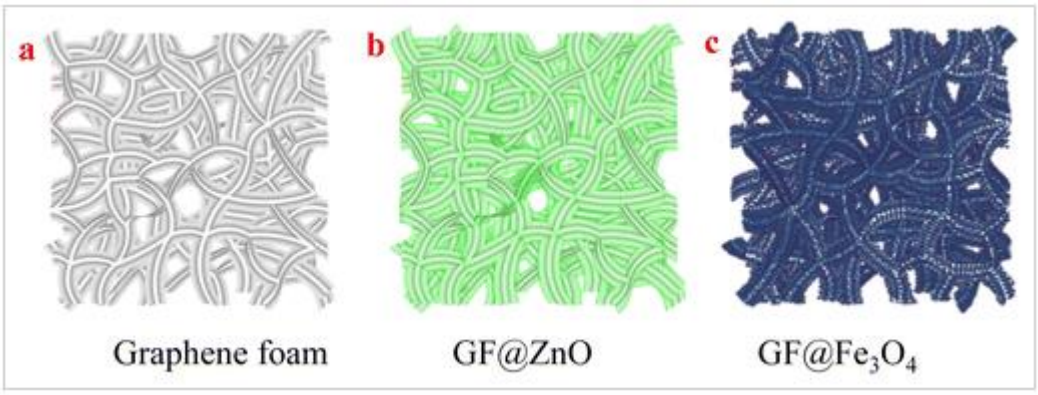

Figure 2-17 *Schematic illustration for the synthesis of graphene foam/Fe_2O_3 composite electrode. Reprinted (adapted) with permission from [71]. Copyright 2013 American Chemical Society*

Our group has also produced a graphene foam-based electrode that can be used as the negative electrode for LICs and LIBs (**Figure 2-18)** [28]. A graphene/MoO_3 foam composite was made using a one-step hydrothermal method in which graphene oxide was mixed with MoO_3 nanobelts in solution. The hydrothermal reaction caused the graphene oxide to simultaneously be reduced and self-assembled into a foam structure with MoO_3 decorating its surface. The foam

composite was then used as a negative electrode alongside a graphene/polyaniline (PANI) foam composite as the positive electrode. The resulting device achieved a high cycle life of 3000 cycles and a high energy density of 128.3 Wh kg^{-1}.

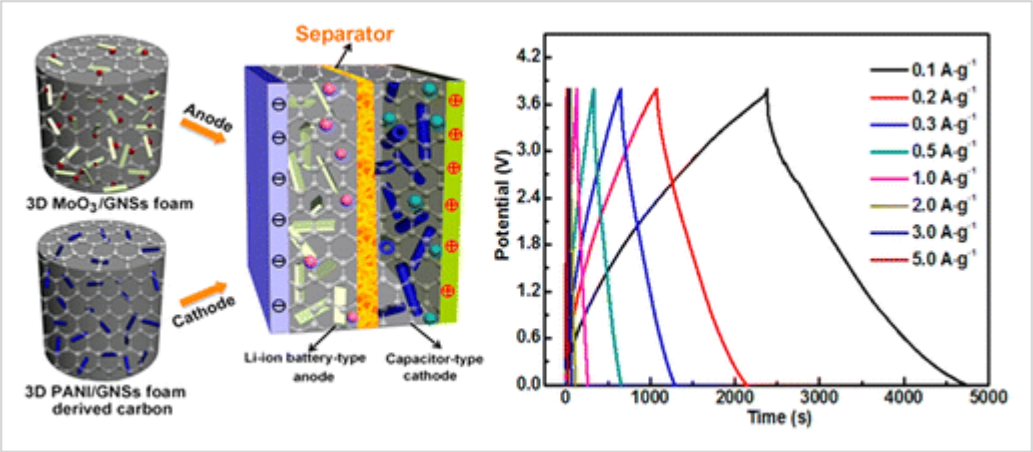

Figure 2-18 *Graphene Foam composites for LICs and LIBs. Reprinted (adapted) with permission from [28]. Copyright 2016 American Chemical Society*

Foam electrodes can also be made by carbonizing nonconductive polymer foams such as melamine formaldehyde or polyurethane [127]–[136]. Depending on the carbonization conditions, both the mechanical and electrical properties of the foam can be controlled to suit specific needs. Chen et al constructed a free-standing foam electrode by pyrolyzing melamine foam and growing $NiCo_2SO_4$ and Fe_2O_3 on its surface [127]. A schematic illustration of their synthesis process is shown in **Figure 2-19**. The neat melamine foam sample also has a high nitrogen doping content in the carbon foam after pyrolisis which increases wettability, electrical conductivity and capacitance [128]. The nitrogen-doped carbon foam was used as an SC electrode, exhibiting a large capacitance of 238 F g^{-1}. Chen et al also demonstrated that their carbon foam can be used as a conductive support for other metal oxides. They grew both

$NiCo_2SO_4$ and Fe_2O_3 on the surface of the carbon foam and used the resulting composites as electrodes in a hybrid SC device, achieving an energy density of 93.9 Wh kg^{-1}.

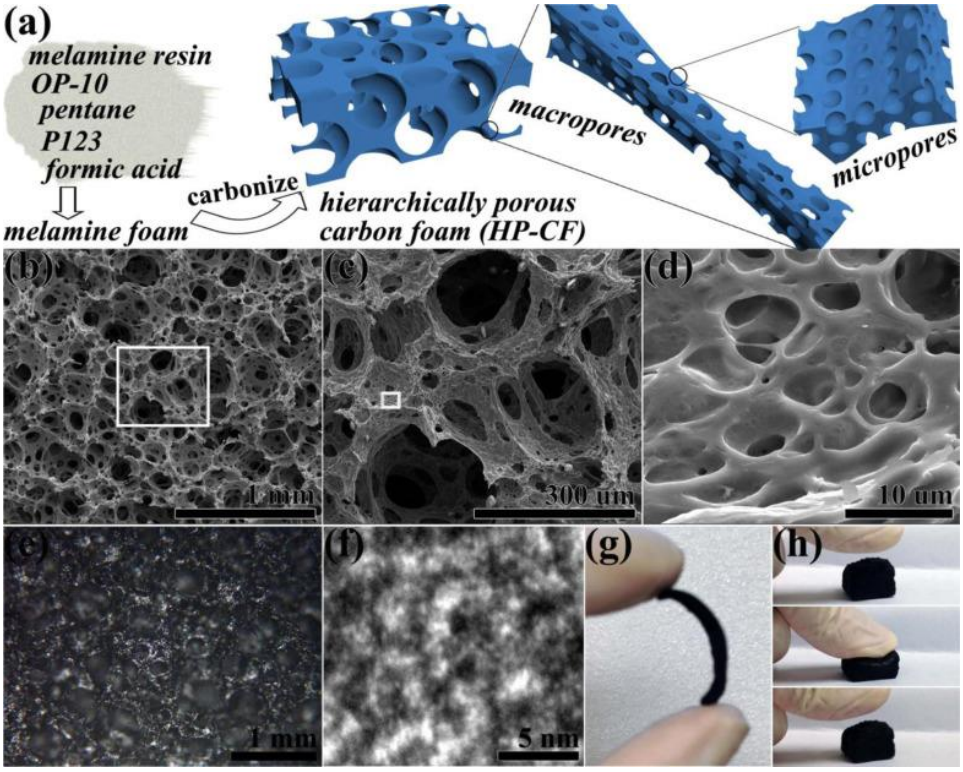

Figure 2-19 *Nitrogen-doped carbon foam from carbonized melamine foam [127]*

2.4 Summary

This section has given a brief background for electrochemical energy storage technologies including lithium-ion batteries, supercapacitors and hybrid lithium-ion supercapacitors. Background discussion on carbonaceous materials, including synthesis methods and applications used in these technologies was also provided in order to give context to the work presented in this thesis.

A review of different flexible electrodes based on carbonaceous materials was also covered, subdivided into 3 categories based on the electrode form. The basic attributes of a good flexible electrode materials, namely mechanical robustness, good electronic conductivity, high specific surface area and high electrochemical activity were also discussed.

3.0 Experimental Methods

Electroactive materials that are used in electrochemical energy storage systems as electrodes can be characterized in many ways. In this thesis, only the relevant characteristics and techniques to elucidate these characteristics will be discussed. The characterization of electroactive materials summarized below can be subdivided into 2 major categories: physical and electrochemical. Each technique shown in the table below will be explained in detail. The purpose of each technique will vary with each project and will be discussed in detail in **Chapters 4**, **5** and **6**.

Table 3-1 *Characterization methods used in this thesis*

Type	**Characteristic**	**Technique**
Physical	Morphology	SEM, TEM, optical microscopy, AFM
	Minimum bend radius	Physical measurement of bend radius at breaking point
	Crystal phase	XRD, TEM
	Degree of Carbonization/reduction	Raman spectroscopy
	Elemental composition	EDX, XPS
	Surface area/porosity	BET
	Particle size	AFM, SEM
Electrochemical	Capacitance, specific energy and power	Galvanostatic charge and discharge, cyclic voltammetry
	Electrochemical impedance	Eletrochemical impedance spectroscopy

Experimental Methods for Electrochemical Measurements	Capacitance, specific energy and power, impedance, cycling stability	Half-cell and full-cell studies

3.1 Physical Characterization

3.1.1 Morphology

The morphology of the electrode material can be probed using scanning electron microscopy (SEM). SEM is a relatively simple technique in order to glean information concerning the surface (physical and elemental make-up) of a material. SEM uses electron beams as a probe allowing much greater magnification and resolution. SEM obtains images from detecting the secondary electrons or back-scattered electrons that are produced after the electron beam strikes the sample. Depending on the imaging mode, the elemental composition of the material can show up as a difference in contrast, allowing for quick identification of different elemental distributions on the surface of the sample.

Transmission electron microscopy (TEM) is a similar technique to SEM but relies on the acceleration of the electrons through a thin sample. Since the accelerating voltage of the electron is inherently higher than SEM, TEM can resolve to even smaller dimensions.

Atomic force microscopy (AFM) can also be used to elucidate the morphological characteristics of a sample. Unlike TEM and SEM, AFM relies on a physical tip sensor in order to obtain information about the characteristics of a surface. AFM has several types of operation which can generally be categorized into contact and non-contact modes. In contact mode, an image is

obtained by dragging the tip across the sample surface, deflecting the cantilever. This deflection can be correlated to a height profile by Hooke's Law due to the known spring constant of the cantilever. A variation of the contact mode is the tapping mode, which is the most common operational method of AFM. In tapping mode, the cantilever is oscillated at its resonant frequency then brought down close to the surface of the sample. The interaction forces between the tip and the sample surface will cause the frequency of the cantilever to decrease. A servo motor then adjusts the height of the cantilever such that the frequency of the cantilever is maintained close to the set point. This variation in height can then be used to construct a topographical image of the sample. Non-contact mode works in similar fashion except that the tip never touches the surface of a sample. Instead, a set distance from the sample (typically in the order of few nanometers) is maintained. AFM can also be used to measure non-topographical information such as magnetic forces. It can also be used to manipulate single atoms or to provide precise reaction control by providing spatially specific stimuli.

3.1.2 Minimum Bend Radius

The bend radius of a material is simply the radius of the inside curvature in which a material can be bent without damaging or shortening its life span. The minimum bend radius is the radius below which said material should not be bent. The minimum bend radius for a flexible electrode can be determined experimentally by measuring the performance of the electrode after t bending at different radii.

3.1.3 Crystal Phase

X-ray diffraction (XRD) can be utilized in order to ascertain the crystal structure of a material using the Bragg equation. XRD works by bombarding a sample with a monochromatic beam

of X-rays. The interaction of the incident X-ray and the sample will produce interference and diffraction that satisfies Bragg's Law:

$$n\lambda = 2d\ sin\ \theta \qquad (3\text{-}1)$$

where λ is the wavelength of the beam, n is an integer, d is the spacing between the diffracting layers and θ is the incident angle of the beam. The X-ray beam and detectors are moved at θ and 2θ angles, respectively. When the incident angle of the beam satisfies Bragg's law, a spike in intensity occurs and is captured by the detector.

3.1.4 Degree of Carbonization

Raman spectroscopy is a technique that measures unique vibrational modes of a molecule in order to identify them. Raman spectroscopy is based on Stokes and anti-Stokes scattering. Stokes scattering occurs when photons of a lower energy level are shifted to a higher energy level due to interactions with the probed system. Conversely, anti-Stokes scattering occurs when photons of a higher energy are shifted to a lower energy level. The information from Raman spectroscopy can be used to identify the degree of carbonization in a sample by examining the G- and D- bands that are unique to graphitic structures. The G-band arises from the stretching of the C-C bond in graphitic structures and corresponds to a Raman shift of approximately 1583 cm^{-1}. The D-band arises from the disorder or discontinuities present in the sp_2-hybridized systems in graphitic structures and corresponds to a Raman shift of approximately 1332 cm^{-1}.

3.1.5 Elemental Composition

Energy dispersive X-ray spectroscopy (EDX) and X-ray photoelectron spectroscopy (XPS) are common techniques to identify the elemental composition of a material. Both of these techniques rely on the measurement of electromagnetic waves from the sample when bombarded with a radiation source. In EDX, the sample is hit with a radiation source that may eject an electron, forming a hole. A higher energy electron may fill this hole and emit its excess radiation in the form of x-rays. Since the x-rays that are emitted are unique for different elements, elemental composition of a specimen can be measured.

XPS works in a similar fashion, measuring the kinetic energies and the amount of electrons ejected by a sample under X-ray radiation. Since the energy of the incoming photon is known, the binding energy of the ejected electron can be calculated by the following equation:

$$E_{binding} = E_{photon} - (E_{kinetic} + \phi) \qquad (3\text{-}2)$$

where $E_{binding}$ is the binding energy of the ejected electron (which allows elemental identification), E_{photon} is the energy of the radiation source, $E_{kinetic}$ is the measured kinetic energy of the ejected electron and ϕ is the work function of the spectrometer and the material.

3.1.6 Surface Area/Porosity

The surface area and porosity of a given sample can be measured using a surface area and pore analyzer. The data obtained from the analyzer can then be interpreted using the Brunauer-Emmett-Teller (BET) theory. BET is an extension of the monolayer molecular adsorption theory proposed by Langmuir into multilayer adsorption. It assumes the following:

1. Gas molecules can adsorb onto the surface of a solid into an unlimited number of layers
2. Individual adsorption layers do not interact with each other

3. Langmuir theory still holds for each individual layer.
4. Adsorption onto the first layer is energetically different
5. Adsorption onto layers 2, 3,…n require similar energies and is similar to condensation

Based on the above, the BET equation is:

$$\frac{1}{v\left[\left(\frac{p_0}{p}\right)-1\right]} = \frac{c-1}{v_m c}\left(\frac{p}{p_0}\right) + \frac{1}{v_m c} \qquad (3\text{-}3)$$

Where p is the equilibrium pressure of the adsorbing species at a given temperature, p_0 is the vapour pressure of the adsorbant at the adsorption temperature, v is the total adsorbed volume, v_m is the monolayer adsorbed volume and c is the BET constant. The specific surface area of a sample can then be found from empirical determination of v_m and c.

3.1.7 Particle Size

The particle size distribution is important because it gives information on the reactivity of a material during an electrochemical reaction. Smaller particles are more reactive compared to larger ones due to the increased surface area to volume ratio. The particle size distribution of a nanosized sample can be measured by SEM/AFM imaging with image analysis software.

3.2 Electrochemical Characterization

3.2.1 Specific Energy and Power

Specific energy and power refer to the capacities to store and discharge energy per unit of mass. They are important units of measure when considering electrochemical energy storage devices. Various techniques can be used to measure the specific energy and power of a device, but the most commons methods are galvanostatic charge/discharge and cyclic voltammetry. Galvanostatic charge/discharge involves charging and discharging the device within a defined potential range using a fixed current. In cyclic voltammetry, a potential sweep is performed and

the current response of the electrode to the potential is measured. Both techniques can be used together in order to determine important electrochemical parameters of LIBs and SCs.

The specific energy (Wh kg^{-1}) of a battery can be calculated from the following equation:

$$E = \frac{\int_0^{tcutoff} V(t) i\, A\, dt}{3600\, m} \qquad (3\text{-}4)$$

where t_{cutoff} is the time over which the battery has completed a charge or discharge cycle, V(t) is the voltage of the battery at a specific time t, i is the current density, A is the area of the electrode and m is the mass of the electrode or battery. In practice, the specific energy of a battery can be approximated by multiplying the maximum capacity (in Ah) of the battery from a charge/discharge curve by the midpoint potential, in V. The practical specific power of a battery can calculated by dividing the specific energy by the time required to charge or discharge the battery.

3.2.2 Capacitance

The capacitance of the system is a measure of the charge accumulated at the electrode/electrolyte interface. In traditional parallel plate capacitors, the capacitance is defined as:

$$C = \varepsilon_0 \frac{A}{d} \qquad (3\text{-}5)$$

Where C is the capacitance in Farads (F), ε_0 is the vacuum permittivity, A is the overlapping area and d is the separation of the two plates. In EDLC supercapacitors, the capacitance is given by equation *(2-2).* Practically, the capacitance of a supercapacitor can be measuring using cyclic voltammetry and the following equation:

$$C = \frac{\int I\, dV}{2\Delta V r} \qquad (3\text{-}6)$$

where C is the capacitance in F, I is the current response in A g^{-1}, ΔV is the potential window used in V and r is the scan rate used in V s^{-1}.

3.2.3 Electrochemical Impedance

The impedance of an electrochemical system is usually measured using electrochemical impedance spectroscopy (EIS) that is sometimes referred to as dielectric spectroscopy. This technique measures a sample's dielectric properties as a function of alternating current (AC) frequency. An EIS measurement is conducted by applying an AC potential to an electrochemical system and then measuring the current response of the system. Due to the AC signal being applied, the output of the system will also result in an AC signal. This means that the impedance of the system can be represented by the complex number as follows:

$$Z(\omega) = Z_0\, exp(cos\, \phi + jsin\phi) \qquad (3\text{-}7)$$

The results of an EIS measurement is usually displayed in the form of a Nyquist plot, where the real component of the impedance is plotted on the x-axis and the imaginary component is plotted on the y-axis. The data from EIS can then be used to estimate important electrochemical properties of the system such as diffusion coeffients, charge transfer resistance and electrolyte resistance.

3.3 Experimental Methods to Characterize Electrochemical Performance

3.3.1 Half-Cell Studies

The electrochemical performance of a material can be measured directly by conducting a half-cell study. For lithium-ion batteries and hybrid capacitors, a half-cell study is conducted using a 2-electrode system in a CR2032 coin cell. In a typical study, the electrode of interest is used

as either the positive or negative electrode with lithium metal as the counter electrode and a separator (either Cellgard 2500 or a cellulose filter paper) sandwiched between them. The electrolyte used is solution of 1M $LiPF_6$ in a 1:1 mixture of ethylene carbonate (EC) and dimethyl carbonate (DMC). This procedure is conducted in glovebox under an inert argon atmosphere (<0.5 ppm O_2) and low ambient humidity (<0.5 ppm H_2O) to prevent electrolyte decomposition and lithium oxidation. A schematic illustration of the coin cell structure is presented in **Figure 3-1**.

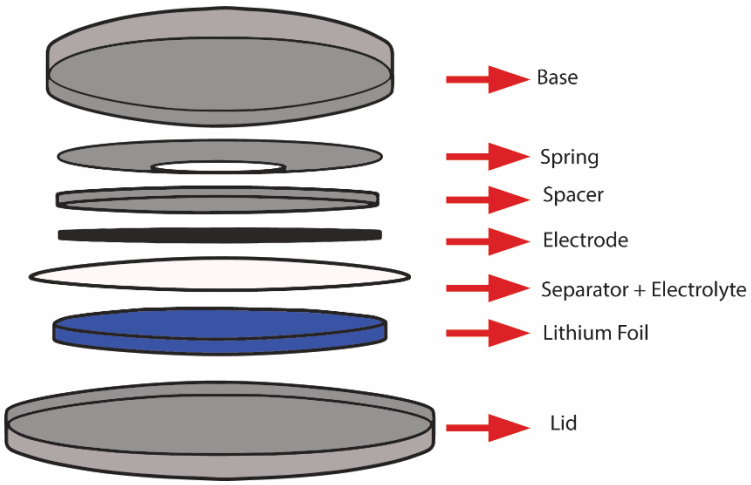

Figure 3-1 Schematic illustration of a CR2032 half-cell construction

For aqueous supercapacitors, the half-cell study is typically conducted using a three-electrode system. In a three-electrode setup, the electrode of interest is used as a working electrode and a platinum foil is used as the counter electrode. A reference electrode is used to provide a stable voltage reference and the type is dependant on the voltage window and type of electrolyte used. Ag/AgCl (0.197 V vs SHE) and saturated calomel electrode (SCE, 0.248 V vs SHE) reference

electrodes were used for neutral/acidic (1M Na_2SO_4/H_2SO_4) electrolytes and basic electrolytes (6M KOH) respectively.

Cyclic voltammetry, galvanostatic charge/discharge and EIS can be conducted on the half-cells to measure the electrochemical performance and characteristics of the cell. Half-cell studies were done in the work described in **Chapters 4, 5 and 6**.

3.3.2 Full-Cell studies

Full-cell studies can also be conducted using CR2032 coin cells. The construction of a lithium-ion battery/hybrid capacitor CR2032 full-cell is the same as a half-cell except that the lithium-metal counter electrode is replaced with the other positive or negative electrode material. In the case of lithium-ion hybrid capacitors discussed in **Chapter 5**, the lithium metal is replaced by an EDLC-type electrode (activated carbon) as the positive electrode. In **Chapter 6**, a flexible full cell is constructed by sandwiching a cellulose filter paper separator between two electrodes and soaking the whole assembly in a 2M KOH/PVA gel electrolyte. The gel electrolyte acts as both an electrolyte and a binder to ensure contact between the electrodes. The same tests conducted on the half-cells are also done on the full-cells.

4.0 Flexible high performance lithium-ion battery electrode based on free-standing TiO_2 nanocrystals/carbon cloth composite

---

Chapter 4 is based on published work by Tjandra et al. in the journal *RSC Advances*.

R. Tjandra, G. Li, X. Wang, J. Yan, M. Li, A. Yu. "Flexible high performance lithium ion battery electrode based on a free-standing TiO_2 nanocrystals/carbon cloth composite". *RSC Adv.*, 6 (42), 35479-35485. 2016

See **Statement of Contributions** for a detailed summary of contributions from each co-author.

In this chapter, a 2-phase solvothermal method is used to synthesize TiO_2 nanocrystals with oleic acid capping. These TiO_2 nanocrystals are then deposited onto carbon cloth to serve as a flexible lithium-ion battery anode. It has been shown that decreasing the size of TiO_2 particles allow them to achieve higher performance when used as anode materials. This is due to the increased volume fraction of the particle that can be lithiated and the smaller electron diffusion pathway through the particle. The oleic acid capping allows the particles to be completely dissolved in toluene, making it easier to disperse evenly on the surface of the carbon cloth without the use of any binders or additive. The subsequent carbonization process allows the nanocrystals to have intimate contact with the carbon cloth. The carbon cloth serves as a flexible current collector that is electrically conductive and mechanically robust. The resulting flexible composite electrode has an excellent reversible capacity of 270 mAh g^{-1} at a current density of

100 mA g^{-1} and excellent physical robustness, retaining its performance after 100 flexion cycles. The flexible composite electrode has more than double the discharge capacity compared to commercial P25 TiO_2 (100 mAh g^{-1} at 100 mA g^{-1}) deposited onto a conventional metal current collector. We believe that this work showcases the potential of carbon cloth as flexible current collector compared to a metal foil current collector. To the best of our knowledge, at the time of publication we achieved one of the highest performances amongst, flexible, free-standing, binder-free TiO_2 nanocrystal-based sanodes.

4.1 Introduction

In recent years, significant attention has been focused on the search for superior electrochemical energy storage devices due to the popularity of hybrid electric vehicles and wearable electronics[18], [39]. Currently, the gold standard for electrochemical energy storage is the lithium-ion battery (LIBs)[39], [137]. LIBs are more popular than other forms of electrochemical storage due to their high energy density, relatively long cycle lives and low self-discharge. These advantages make LIBs perfect for many broad applications such as hybrid electric vehicles and portable electronics. However, one of the limitations of LIBs is their rigidity which limits their application in emerging technologies such as flexible and wearable electronics[12], [138], [139]. Cui et al have shown that the crucial factor for achieving flexible LIBs is the development of flexible electrode materials[105]. Several important parameters must be considered when designing a flexible electrode for LIBs in order to achieve high performance. Numerous approaches to the development of flexible electrodes such as printable flexible batteries[138], paper based batteries[11], [105] and carbon based batteries[109], [140], [141] have been reported. The performance of the electrode relies on several properties of the material such as high electronic and ionic conducitivity, high surface area and good electrical

contact between the active material and current collector. As such, much of the focus has been on the search for materials or combination of materials with the aforementioned properties. Amongst the numerous strategies to obtain such materials, synthesis of nanostructured materials has been promising. Nanostructures provide high available surface area in addition to shortening the lithium ion diffusion path lengths, allowing for both greater energy and power density[142]. Carbon cloth has been a popular choice as current collector and substrate for the growth of various nanostructured active material. Its flexibility, relatively high electron conductivity and robustness makes it a great alternative to metal foils[109], [112], [141], which are conventionally used as a current collector in LIBs. Titanium dioxide (TiO_2) is a promising electrode material that has been used in a wide range of applications from photocatalysis[143], [144] to solar cells[145], [146] due to its low-cost, natural abundance, low toxicity and high stability in various solvents[147]. Most recently, TiO_2 and its associated polymorphs have been investigated for use in LIBs and supercapacitors[36], [148-152]. However, the use of bulk TiO_2 has its own drawbacks such as poor electronic conductivity and slow lithium-ion transport [149]. Therefore, many strategies have been developed to overcome the limitations of TiO_2 including the synthesis of novel TiO_2 structures[147], [153] and TiO_2 composites[69], [109], [143], [154] and decreasing the particle size of TiO_2[155], [156]. For example, Balogun et al synthesized a TiO_2 and titanium nitride composite nanowire that was used as a flexible anode for LIBs with a reversible capacity of 240 mAh g^{-1}[109]. Yang et al doped TiO_2 with Nb in order to form nanoplate composites that with a reversible capacity of 220 mAh g^{-1}[154]. Chen et al fabricated a free-standing carbon nanotube and TiO_2 composite that delivers a reversible capacity of 270 mAh g^{-1} [113]. Wang et al fabricated a hierarchical 3D structure of TiO_2 on

carbon nanowire arrays, achieving a flexible battery anode with a high capacity and cycling stability [157].

Herein, a novel flexible binder-free TiO_2 negative electrode material has been successfully prepared by directly growing TiO_2 nanocrystals on carbon cloth using a solvothermal process with the assistance of oleic acid. The oleic acid allows the TiO_2 nanocrystals to be well dissolved in organic solvents so that they can be dispersed more evenly on the surface of the substrate. This is an advantage as common electrode fabrication methods involve preparation of slurries which may have difficulty in dispersing the active materials, resulting in difference in performance from batch to batch. Carbon cloth was chosen as the substrate due to its flexibility, something that traditional current collectors such as copper foil collector lack. The resulting composite electrode exhibits an excellent reversible capacity of 270 mAh g^{-1} at current density of 100 mA g^{-1}, which is close to the theoretical capacity of TiO_2. The excellent performance is attributed to the unique structure and the small size of the TiO_2 nanocrystal. The method presented herein can be used to fabricate other flexible energy storage devices.

4.2 Experimental Methods

4.2.1 Materials Preparation

All chemicals were purchased from Sigma-Aldrich and used as-received unless otherwise noted. Commercial carbon cloth was treated as follows. First, carbon cloth was sonicated successively in ethanol, methanol and isopropanol for 15 min each, and then dried in an oven for half an hour. Next, the resulting clean carbon cloth was heat-treated at 900˚C in a tube furnace under an inert argon atmosphere.

TiO_2 was synthesized using a two-phase solvothermal method reported elsewhere[114]. The water phase was made by mixing 20 mL of distilled deionized water and 0.2 mL of tert-butylamine, while the oil phase was composed of 20 mL toluene, 330 μL of titanium isopropoxide and 2 mL oleic acid. The two separate phases were then transferred into a 100 mL steel autoclave with a Teflon liner. The autoclave was heated to 180˚C for 12 h and cooled down to room temperature. The resulting oleic acid-capped TiO_2 was washed with methanol and re-dispersed in toluene. This stock solution was then diluted to the desired concentration. The solution of nanocrystals in toluene was stable and did not observe any precipitates even after several weeks.

The fabrication process of flexible binder-free TiO_2 electrode proceeded as follows. First, carbon cloth was cut into 12 mm circular electrodes using a commercial electrode punch. Then, TiO_2/toluene solution was added dropwise using a pipette onto the carbon cloth. The resulting composite material was then annealed in a tube furnace under air atmosphere at 450˚C for 3 hours at a heating rate of 1˚C/min to remove the oleic acid capping agent. The approximate final TiO_2 loading of each electrode is 0.6 mg/cm^2. The composite electrode was then assembled into coin cells under an inert argon atmosphere with a cellulose separator and lithium metal counter-electrode.

4.2.2 Physical Characterization

The morphologies and nanostructures of the carbon cloth, TiO_2 nanocrystals and the composite electrodes were characterized using a field emission scanning electron microscope (FE-SEM, Zeiss LEO 1530, 10 kV). The crystal structure and purity of the synthesized TiO_2 crystals were determined using powder X-ray diffraction (XRD, Bruker AXS D8, 0.154 nm Cu-α source) and Raman spectroscopy (Brukker SENTERRA). Thermogravimetric analysis (TGA, TA Q500,

Ar atmosphere, 1°C min^{-1} ramp rate) was conducted to confirm the actual TiO_2 and oleic acid mass ratios. The mechanical stability of the electrode was tested by subjecting the as-prepared composite electrodes to 100 bend cycles, whereby each cycle involved of going from un-flexed (shown in **Figure 4-1 (a)**), to 180° flexion (shown in **Figure 4-1 (b)**) and back to the un-flexed position.

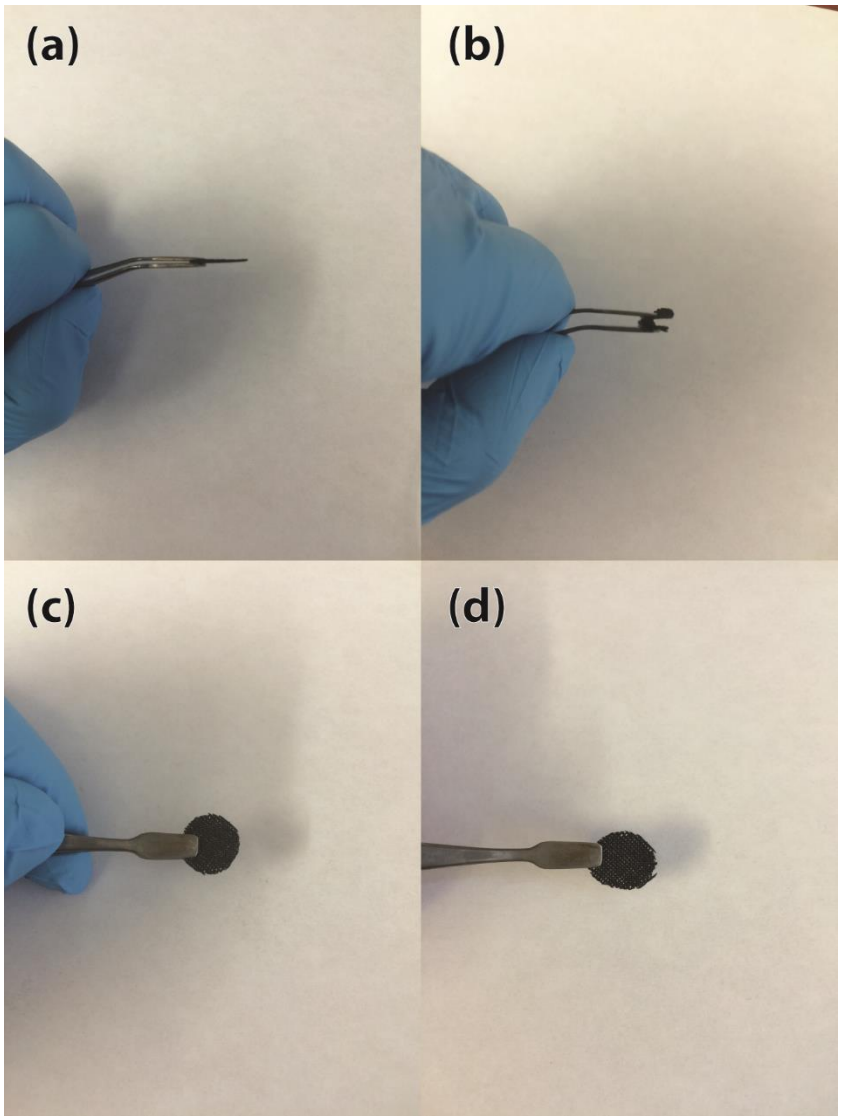

Figure 4-1 *Images of the flexible electrode (a) at "un-flexed" position, (b) at full, 180° flexion, (c) before 100 cycles of mechanical flexion, (d) after 100 cycles of mechanical flexion*

4.2.3 Electrochemical Characterization

All the electrochemical characterization in this work was conducted using a two-electrode system in the form of a CR3023 coin cell. The electrolyte consisted of 1 M of $LiPF_6$ salt dissolved in a 1:1 mixture of ethyl carbonate and dimethyl carbonate. Each cell was wetted with 50 μL of electrolyte solution. Galvanostatic charge and discharge (GCD) was performed using a Neware battery testing station from 1 V to 3 V at current densities ranging from 0.1 C to 20 C. To demonstrate another advantage of the binder-free flexible electrode, a flexible pouch half-cell was fabricated. As a comparison, electrodes were also made using via traditional slurry-based method using commercially available TiO_2 nanoparticles (Degussa P25) with an average diameter of 25 nm at a similar loading to the composite electrodes. Here, the TiO_2 nanoparticles, polyvinyldifluoride (PVDF) and conductive carbon at a weight ratio of 8:1:1 was homogeneously suspended in N-methyl-2-pyrrolidone.

4.3 Results and Discussion

Schematic illustrations of the composite electrode synthesis in shown by **Figure 4-2 (a)**. First, oleic acid-capped TiO_2 nanocrystals were drop-casted onto bare carbon cloth.

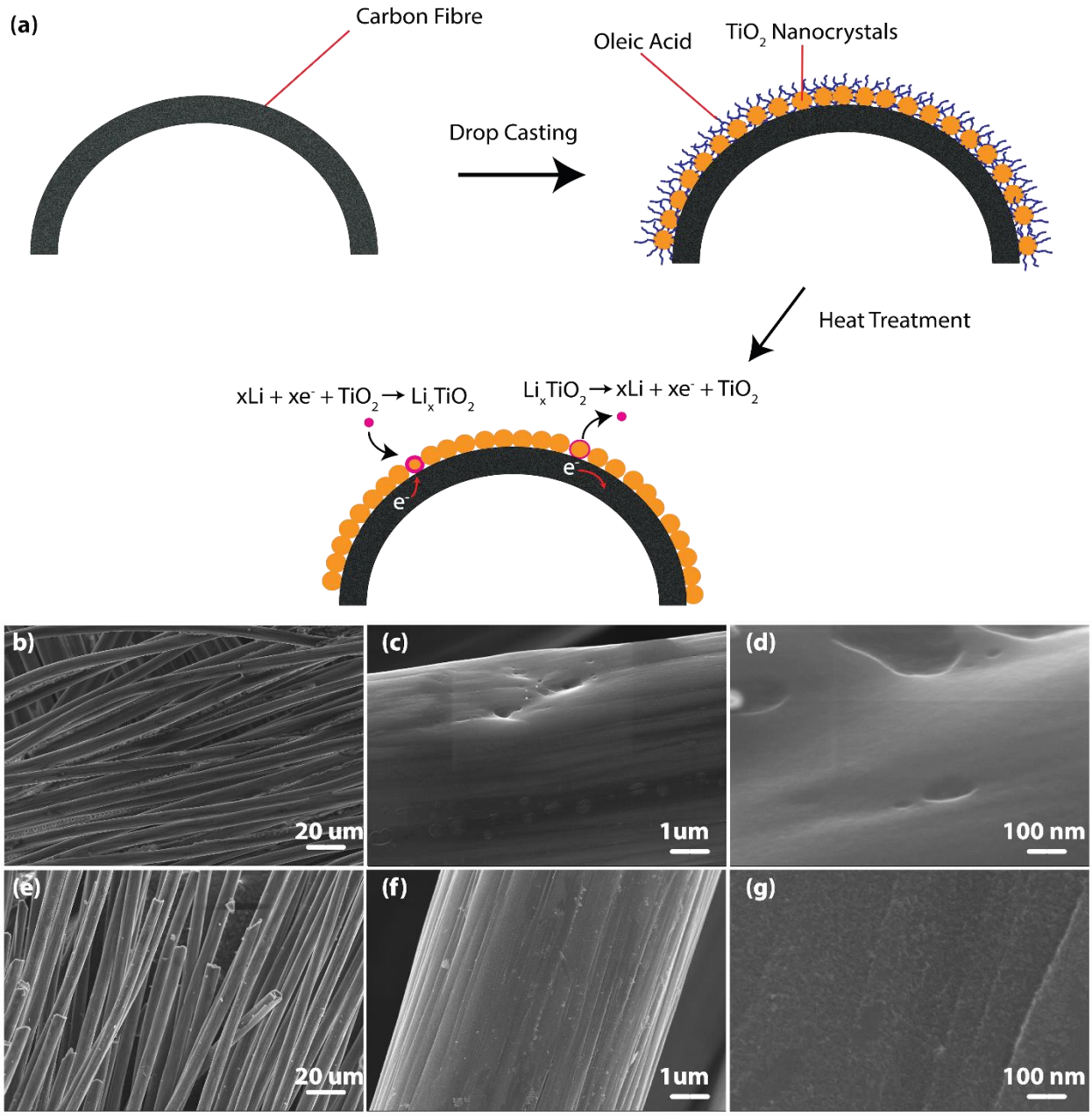

Figure 4-2 *(a) schematic illustration of the fabrication of the composite TiO_2/Carbon Cloth electrodes, (b)-(d) SEM images of pre-annealed TiO_2/Carbon Cloth, (e)-(g) SEM images of post-annealed TiO_2/CC.*

Then, the resulting composite was annealed in order to remove the oleic acid, which is non-conductive. **Figures 4-2 (b) – (d)** show SEM images of the surface of the composite TiO_2/CC

electrode before annealing and **Figures 4-2(e) – (g)** shows the surface of the composite electrode after annealing. It can be seen that the pre-annealed TiO_2 forms a uniform, smooth and polymer-like coating on the surface of the carbon fibers, which have a diameter of approximately 6 μm. This is due to the oleic acid capping that helps connect the TiO_2 particles seamlessly. When the electrode is annealed in air, the TiO_2 spheres are uniformly coated on the carbon fiber after the oleic acid capping is removed, as shown by the difference of smoothness shown in **Figures 4-2 (d) and (g)** with the surface of the post-annealed electrode becoming more rough and bumpy, indicating the presence of particles. **Figure 4-3** shows the TGA curve of pure TiO_2 nanocrystals which indicates that the oleic acid capping agent has been completely removed by 450°C, leaving behind TiO_2 particles. It can also be seen that the oleic acid comprises 20% of the mass of the nanocrystals. The amount of oleic acid was taken into account when calculating the TiO_2 loading masses cited in this work.

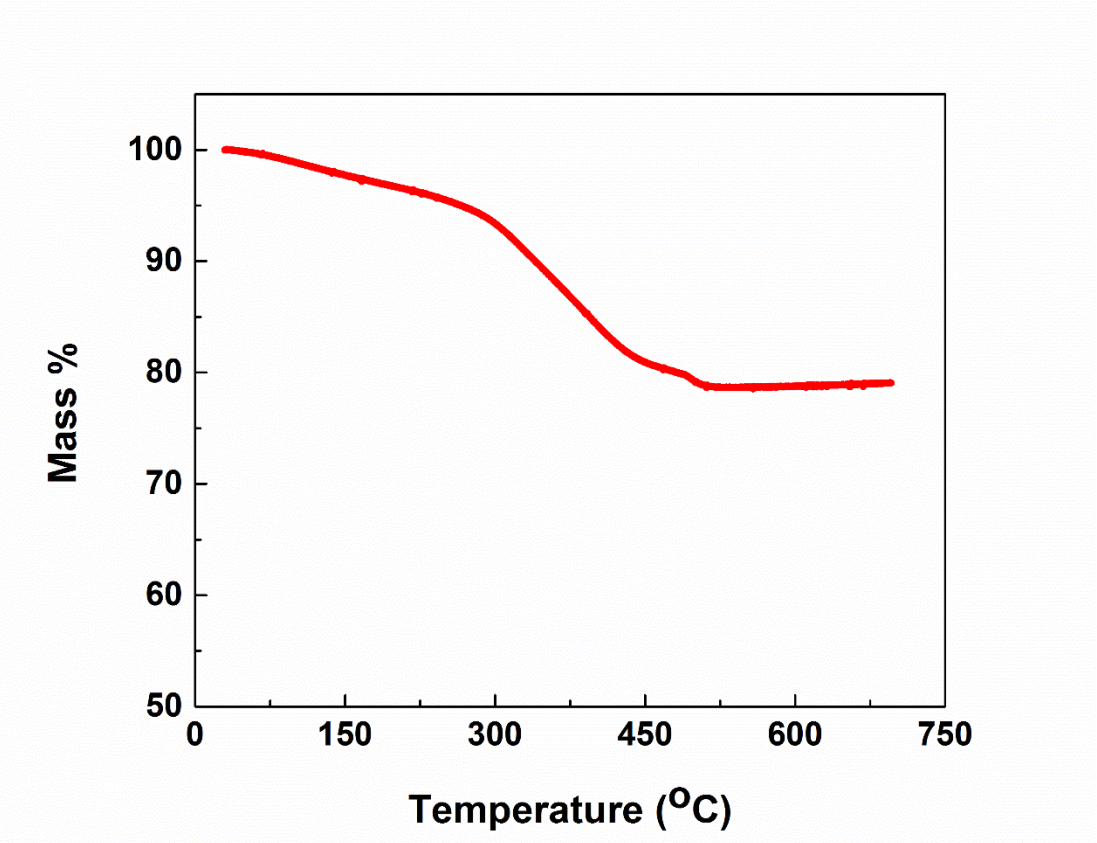

Figure 4-3 *TGA curve for the TiO_2/Oleic Acid nanocrystals*

From **Figure 4-2 (g)**, it appears that the TiO_2 nanocrystal spheres have a size of ~10 nm. The oleic acid helps distribute the particles uniformly on the carbon fibers to maximize the exposed surface area of the TiO_2 nanoparticles to electrolyte and allow greater lithium-ion access to the inner structure of TiO_2 which is beneficial for the improvement of specific capacity and rate capability. Additionally, the oleic acid also ensures intimate contact between the substrate and TiO_2, which can reduce the internal resistance and improve the cycling stability of the electrode. It is worth noting that no discernible change in mechanical properties of the carbon cloth was observed before and after annealing at 450°C in air. **Figure 4-4** shows the carbon cloth before it is annealed (**Figure 4-4 (a)**) and after (**Figure 4-4 (b)**) it is annealed in air.

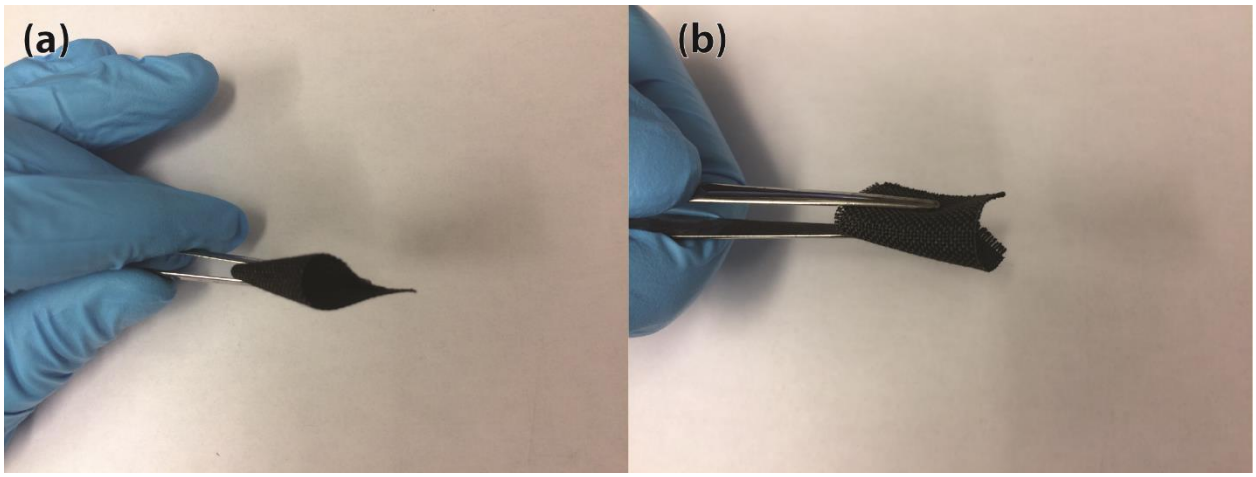

Figure 4-4 *Figure illustrating the similarity of flexibility of (a) un-annealed carbon cloth and (b) annealed carbon cloth*

Both pieces of carbon cloth are very similar in flexibility and apparent mechanical strength. Importantly, the post-annealed piece of carbon cloth does not show any signs of being more brittle than the pre-annealed piece.

Figure 4-5 shows the Raman spectrograph and x-ray diffractograms of bare carbon cloth and the various stages of the composite electrode. The Raman spectrograph shows both the G and D bands at ~1400 cm^{-1} and ~1600 cm^{-1} which comes from the graphitic structure found in carbonaceous materials. A sharp peak is also observed at ~150 cm^{-1} which is characteristic of anatase TiO_2. The Raman spectrograph shows that there is no change in the TiO_2 crystal structure after the electrode is annealed. It is clear from the differences in the peakts of the bare carbon cloth and the composite electrode that TiO_2 is present on the carbon cloth. The XRD diffractogram also confirms the presence of anatase TiO_2 on the surface of the carbon cloth. The XRD pattern of the pure TiO_2 nanocrystals matches well with that of bulk anatase TiO_2 (JCPDS Card No. 21-1272)[148] . The diffractogram also shows that the crystal structure of

the anatase TiO_2 remains unchanged after drop-casting and annealing to remove the oleic capping agent. The crystal domain size estimated from the (101) peak using the Scherrer equation is about 10.8 nm. This is consistent with the SEM images shown previously.

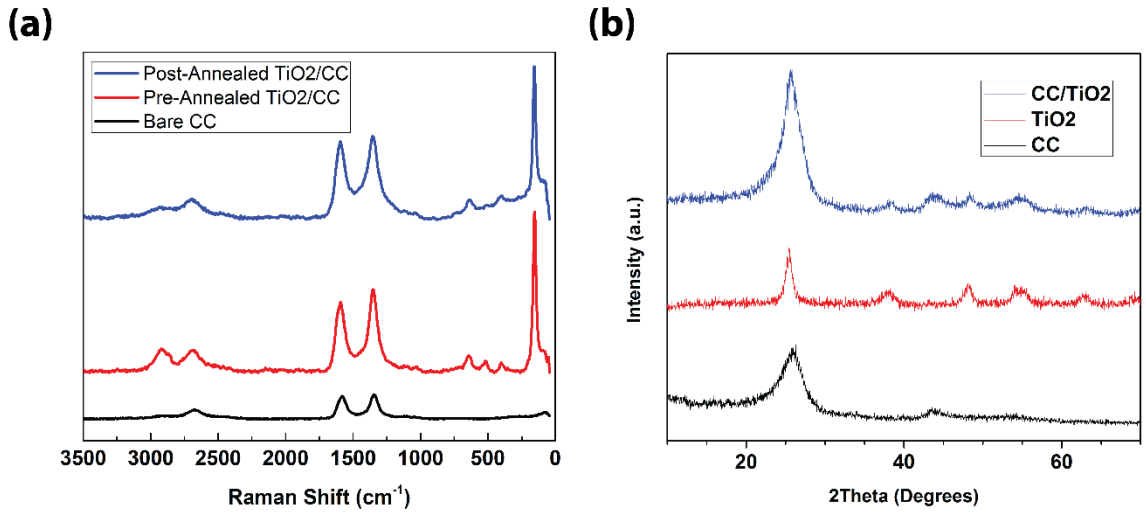

Figure 4-5 *(a) Raman spectrograph of neat carbon cloth (black), pre-annealed composite electrode (red) and post-annealed composite electrode (blue) (b) X-ray diffractogram of neat carbon cloth (black), post-annealed TiO_2 particles (red), post-annealed composite electrode (blue)*

Figure 4-6 shows the electrochemical performance data of the composite electrode. **Figure 4-6(a)** shows the discharge capacities of the TiO_2 nanocrystal and carbon cloth binder-free composite electrode while **Figure 4-6(b)** shows the discharge capacities of a commercial TiO_2 (25 nm in size) that was coated onto copper foil using the typical slurry-based fabrication method. In comparison, the binder-free composite electrode show better performance than that of the commercial TiO_2 nanoparticles at the same current density, which may be attributed to the unique structure of the binder-free TiO_2 that enhances the access of electrolyte and reduces the internal contact resistance. Another factor is the small size of the TiO_2 nanoparticles. As the particle sizes decreases below 10 nm, the lithium-TiO_2 intercalation compound starts to

behave similar to a solid solution which allows a higher density of lithium-ions to be packed and resulting electrode capacity [156].

Figure 4-6(c) shows the first charge and discharge curves of the composite electrode at a current density of 100 mA g^{-1}. The curves shows both the Li-ion insertion and extraction potentials, corresponding to ~1.7V and ~1.9V respectively, which matches with results shown in literature[36], [44], [113], [148], [151]. The discharge plateau of TiO_2 (at ~1.7 V) corresponds to the diffusion-controlled capacity[113], [114], [158]. In this region, the lithium ions are diffusing into the crystal structure of TiO_2 and the capacity is limited by the solid mass transport of the ions and diffusion length[148], [159], [160]. It has been previously shown that as the crystal size decreases, the capacity in this region increases as the diffusion length of the lithium ions decrease and vice versa [156]. The low-sloped, linear region of the discharge curve corresponds to the surface-controlled capacity[113], [114], [158]. In this region, the lithium ions react and adsorb on the surface/near-surface of the TiO_2 crystals at a rate limited by the available surface area. When the crystal size decreases, the surface-controlled region will generally also increase due to the increased surface area-to-volume ratio [114]. At higher current densities, the ratio of the diffusion-controlled capacity to the surface-controlled capacity will decrease since the lithium will have less time to fully permeate the crystal structure [156].

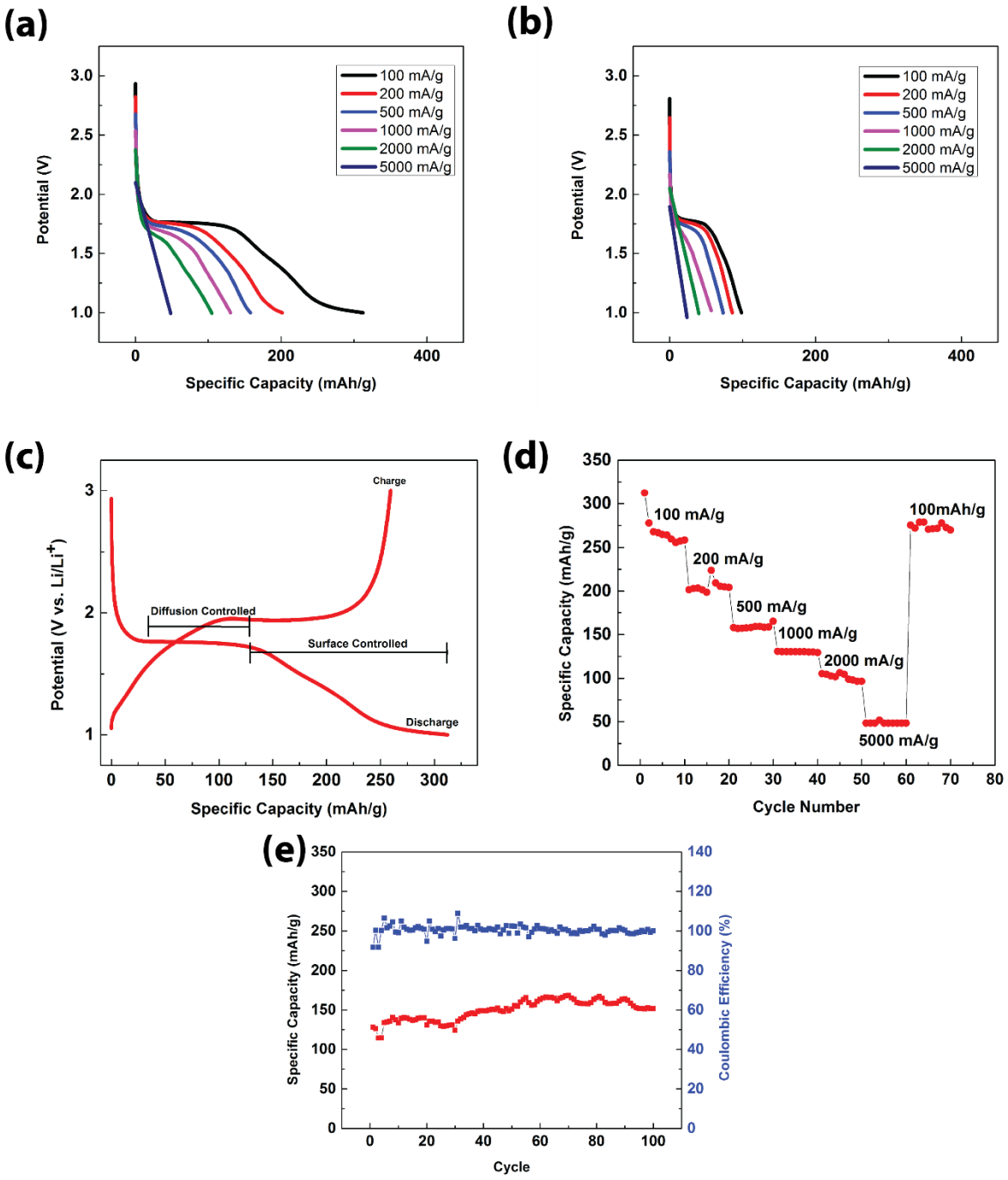

Figure 4-6 *(a) Discharge profiles of the composite electrode at different currents with a loading of ~0.5 mg cm-2 (b) Discharge profiles of commercial TiO_2 with a loading of ~0.5 mg cm-2 (c) First charge and discharge profile of the composite electrode (d) Rate performance of the composite electrode (e) Specific discharge capacity (red) and coulombic efficiency (blue) of the composite electrode over 100 charge and discharge cycles at a loading of ~0.5 mg cm-2 and current density of 500 mA g-1*

Another thing of note is that compared to the discharge curve of the commercial TiO_2 on copper foil at 100 mA g^{-1} shown in **Figure 4-6(b)** the TiO_2/carbon cloth composite has a significantly higher surface-controlled capacity. This effect may be explained by the increased surface area of the TiO_2 nanocrystals in addition to the increased available surface area of carbon cloth compared to copper foil. Thus, the carbon cloth has a synergistic effect on the nanostructured TiO_2, allowing a greater surface-controlled charge storage capacity. We have also measured the capacity of the neat carbon cloth, shown in **Figure 4-7**, in order to demonstrate the lithium-ion storage capacity is almost entirely due to the presence of TiO_2.

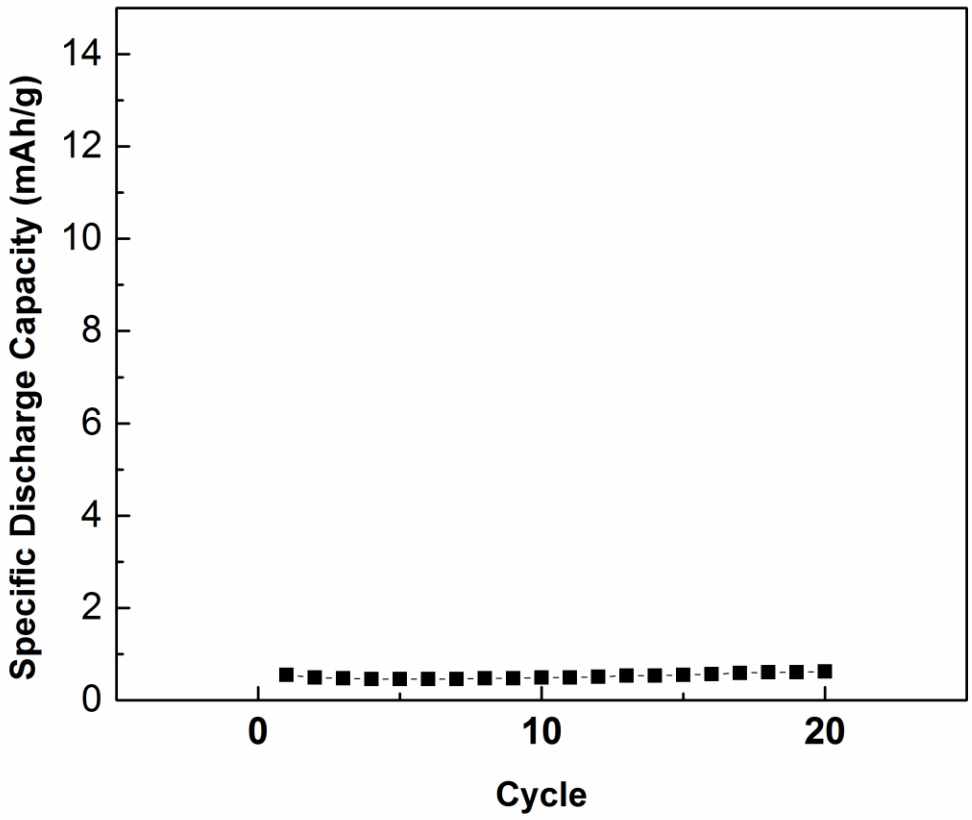

Figure 4-7 *Discharge capacity of neat carbon cloth over 20 charge and discharge cycles at a current density of 100 mA g-1*

Figure 4-6 (d) shows the discharge capacities of the composite electrode at different current densities. The first discharge capacity of the electrode at 100 mA g^{-1} is approximately 310 mAh g^{-1}, and still remains at 280 mAh g^{-1} after 10 cycles, [158], [161] As the current density increases, the capacity drops due to the aforementioned mechanisms. It can be seen that at each applied current densities, the charge and discharge capacity of the electrode remains relatively stable, revealing the high coulombic efficiency, which reflects the stability of electrode structure during lithium insertion and extraction. When the current returns to the initial value of 100 mA g^{-1}, the reversible capacity returns to 280 mAh g^{-1}, indicating a good rate performance. **Figure 4-6 (e)** shows the specific discharge capacity of the composite electrode and its coulombic efficiency over 100 charge and discharge cycles at a current density of 500 mA g^{-1}. We can see that the composite electrode exhibits good cycling stability after 100 cycles, demonstrating a discharge capacity of ~150 mAh g^{-1}. This is consistent with the discharge capacity exhibited by the electrode during rate performance tests. We also see that the coulombic efficiency of the composite electrode remains ~100% throughout the 100 cycles of charging and discharging.

Figure 4-8 shows the effect of the TiO_2 solution concentration when drop casting (with similar mass loadings) on the capacity of the electrode. As the concentration decreases, the performance of the electrode increases. This may be explained by particle aggregation on the electrode and the low conductivity of TiO_2. As the loading increases, the utilization of the TiO_2 for lithium ion storage decreases[149]. Although the particles are able to be fully dissolved in toluene, the high concentrations may lead to aggregation once the solvent evaporates.

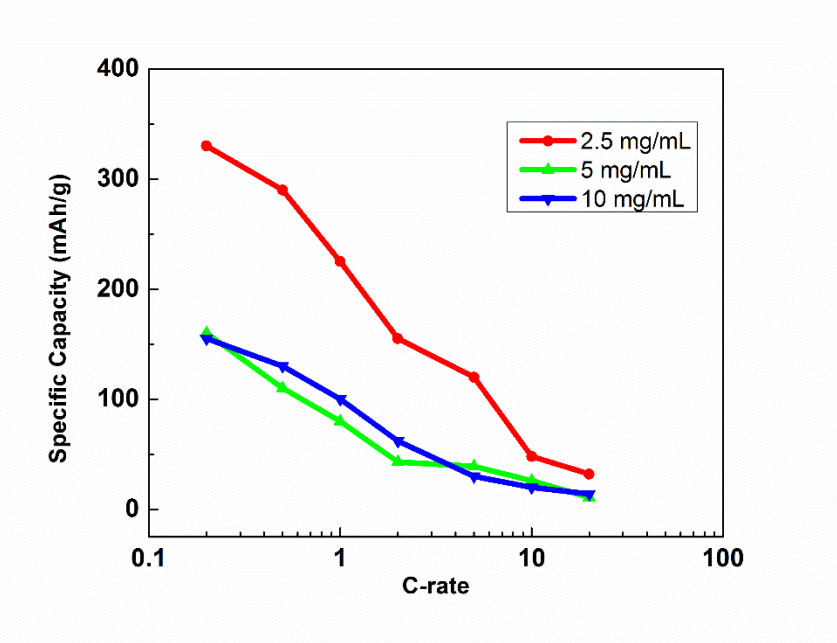

Figure 4-8 *Rate performance comparison between different electrodes made from various TiO_2 solution concentrations*

This result is confirmed by SEM imaging to probe the surface morphology of the electrodes with similar mass loadings but different casting concentrations as shown in **Figure 4-9**. **Figures 4-9 (a) – (b)**, **(c) – (d) and (e) - (f)** show the surfaces of the composite electrode made with casting concentrations of 2.5, 5 and 10 mg mL^{-1} respectively.

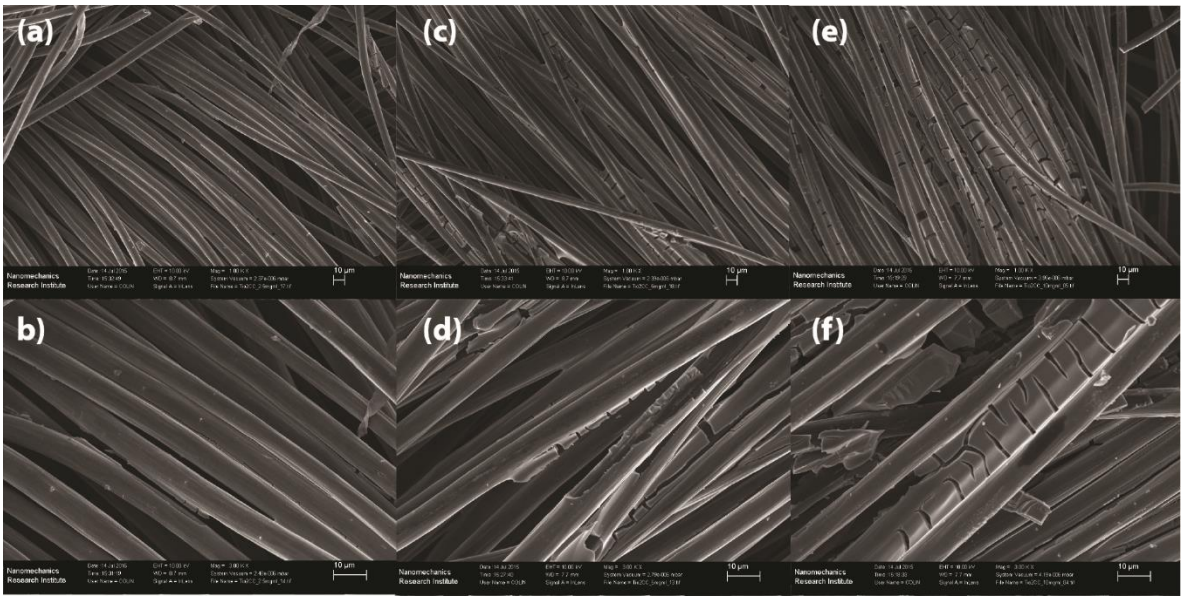

Figure 4-9 *SEM images of the surface of composite electrodes with similar loadings made with different TiO_2 nanocrystal casting concentrations (a)- (b) 2.5 mg mL-1, (c)- (d) 5 mg mL-1, (e)- (f) 10 mg mL-1*

It can be seen that higher casting concentrations leads to more aggregates of TiO_2, resulting in non-uniform thicknesses and cracking. This result is consistent with the performance of the electrodes as shown in **Figure 4-8**. The effect of lower concentrations was not investigated as it would be impractical to fabricate electrodes with higher loadings and a low solution concentration. However, it can be assumed that lower solution concentrations will increase the performance by ensuring an even distribution of the particles onto the surface of the current collector. The best drop casting concentration (2.5 mg/ml) was then used for subsequent electrode fabrication.

Figure 4-10 shows a proof-of-concept flexible half-cell made with the TiO_2/carbon cloth composite electrode. **Figure 4-10 (c)** shows a schematic illustration of the half-cell construction. The half-cell demonstrates the flexibility and performance of the composite

electrode under flexion. The pouch half-cell was able to power an LED bulb with and without flexion. In addition to the proof-of-concept flexible half-cell, the mechanical stability of the electrode was also tested. **Figure 4-1 (c) and (d)** shows the as-prepared composite electrode before and after 100 cycles of mechanical flexion. Besides a slight physical deformation of the electrode along the bend-axis, the electrode shows no other signs of wear. The mass of the electrode before and after 100 cycles of bending only changed by 0.30%, indicating that the composite electrode has good mechanical stability.

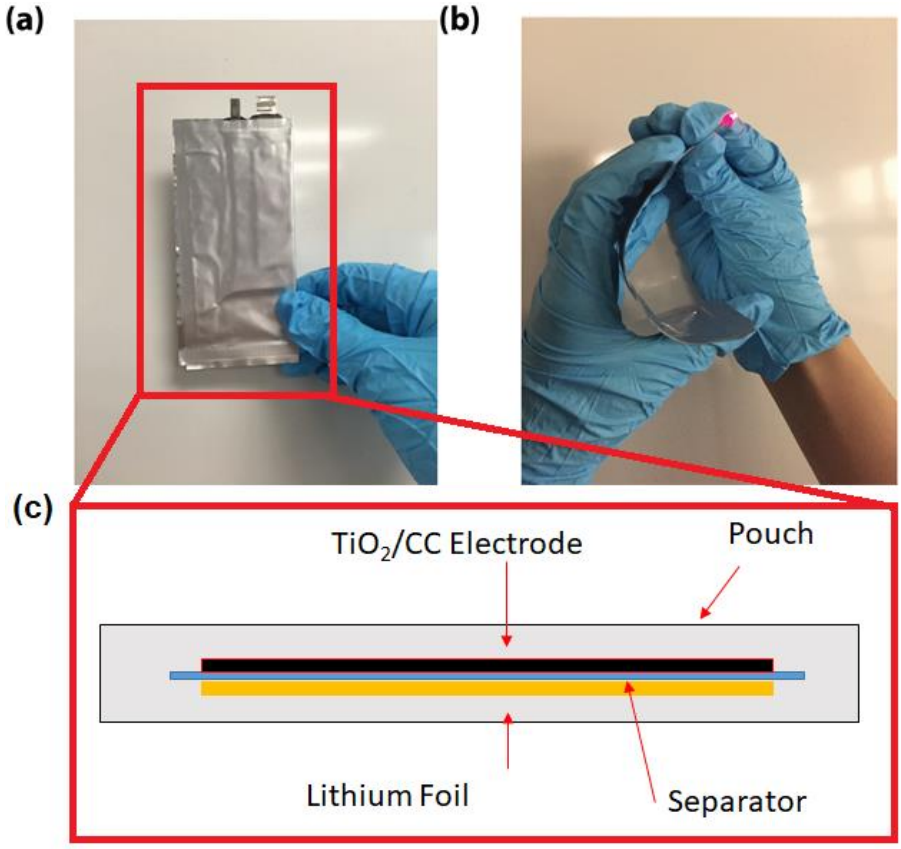

Figure 4-10 *(a) flexible pouch half-cell made using the composite anode, (b) flexible pouch half-cell powering an LED bulb under flexion, (c) schematic illustration of the pouch cell construction*

4.4 Conclusions

In this work, TiO_2 nanocrystals with sizes of about 10 nm were synthesized and drop casted onto carbon cloth to produce a composite flexible electrode material. Importantly, the electrode exhibited a reversible capacity of 270 mAh g^{-1} at a current density of 100 mA g^{-1}, which is close to the theoretical capacity of TiO_2. The excellent performances are attributed to the unique structure and the small size of TiO_2 nanocrystal. The TiO_2 nanocrystals were uniformly

deposited onto the carbon cloth substrate due to oleic acid capping that helps act as a surfactant to dissolve the crystals in toluene. This is beneficial to reducing the inner resistance and the access of electrolyte. Moreover, the small crystal size aids in shortening the lithium-diffusion pathway and also increasing the surface area available to the electrolyte solution. The work presented here may be applied to other metal oxides and other flexible substrates in order to further improve the performance of LIC anodes.

5.0 Melamine-based, N-doped carbon/reduced graphene oxide composite foam for lithium-ion hybrid supercapacitors

---

Chapter 5 is based on published work by Tjandra et al. in the journal *Carbon*.

R. Tjandra, W. Liu, L. Lim, A. Yu. "Melamine based, n-doped carbon/reduced graphene oxide composite foam for Li-ion Hybrid Supercapacitors. *Carbon* 129, 152-158. 2018

See **Statement of Contributions** for a detailed summary of contributions from each co-author.

In this chapter, a compression-tolerant, nitrogen-rich carbon/reduced graphene oxide composite foam was synthesized and used as a free-standing, binder-free electrode for lithium-ion hybrid supercapacitors. This involved loading a melamine formaldehyde foam with graphene oxide and then using a heat treatment process in order to carbonize the melamine and reduce the graphene oxide in one simple step. The resulting composite foam could be compressed to almost 100% of its original height without any loss of material or structural integrity. The reduced graphene oxide acts as the primary lithium-insertion host while the nitrogen rich carbon foam provides a conductive backbone that facilitates electron transfer. The electrode could achieve a reversible capacity of 290 mAh g^{-1} at a current density of 100 mA g^{-1} when used as the negative electrode for lithium-ion hybrid supercapacitors. The composite foam could also be used as a conductive, binder-free host for other active materials. To show the versatility of

the material, we fabricated a proof-of-concept lithium-ion hybrid supercapacitor that used the composite foam as both a stand-alone binder-free anode and a binder-free current collector for the activated carbon cathode. The resulting device shows excellent performance that matches that of other lithium-ion hybrid capacitors reported in the literature based on metal oxides (which are generally more energy dense than purely carbon materials).

We have also extended this work to show that the carbon foam can be used in other electrochemical energy storage systems. Specifically, we used the same composite foam as a free-standing, binder-free electrode in an EDLC supercapacitor system.

5.1 Introduction

Lithium-ion batteries (LIBs) are currently the gold standard for electrochemical energy storage[2], [9]. LIBs are ubiquitous in our daily lives, powering many electronic devices such as mobile phones and laptops. In addition to powering small consumer electronic devices, LIBs are also used in electric and hybrid electric vehicles and various hybrid-electric buses that are often operated in metropolitan areas [2], [39], [162] . Recently, improvements have been made to LIBs by combining LIB electrode materials with those of supercapacitors to create a hybrid device. One such device is the lithium-ion hybrid supercapacitor (LIHS) which combines the negative electrode of a LIB with the positive electrode of a supercapacitor[28], [33], [163], [164]. This allows the hybrid device to deliver a higher energy density than conventional supercapacitors while still retaining its power density [28], [33], [164]. An even greater advantage is its long-term cycling stability compared to that of a typical LIB, making it attractive for uses in which long-term reliability is key [164], [165]. Current commercial LIHSs utilize graphite as an anode material paired with activated carbon as the cathode. One major problem for LIHSs is that their energy density is still much lower than that of LIBs, limiting

their application [18], [33], [164]. Much effort has been made to develop new materials in order to improve the energy density and rate capability of LIHSs to meet the demands of new and applications.

Many strategies have been reported for the improvement of LIHSs electrodes, although most still rely on a conventional two-dimensional material coated on copper and aluminum foil. While two-dimensional electrodes are currently the standard, they limit the electrochemical storage performance due to the requirement of additional materials such as binders and conductive agents which do not contribute to the energy density of the device. Recently, significant attention has been put towards using three-dimensional electrode material as an alternative [23], [28], [71], [121], [122], [127], [129], [131]–[133], [136], [166], [167]. At the forefront, carbon foams have the most promise due to their high conductivity, high specific surface area, light weight and relatively high mechanical stability [31], [72], [121], [128], [134], [168]–[170]. In addition, carbon foams can also be made flexible and compressible which open up some interesting applications [135], [171], [172].

Carbon foams are defined as a three-dimensional, interconnected network of carbon materials. They are attractive as supports for active materials due to their much higher surface area than that of their two-dimensional counterparts. Generally, carbon foams can be made by using one of two methods: direct carbonization of a precursor template and bottoms-up assembly of a suspension of carbonaceous materials[31], [128]–[131], [135], [173], [174]. The first approach usually yields mostly amorphous carbons, though graphitic carbons can also be achieved by careful control of the carbonization conditions [128], [133], [135]. This method is less costly as the precursor templates are more often than not inexpensive and abundant. However it is difficult to form a highly conductive foam while preserving the mechanical properties of the

original template. The second approach typically makes use of graphene suspensions or freeze drying graphene oxide suspensions followed by thermal reduction [28], [122], [123]. The freeze-drying method is usually costly and time consuming due to the high concentrations of graphene oxide needed and the length of time to fully freeze-dry the sample. Furthermore, pure graphene foams are often mechanically fragile and delicate making handling very difficult. A combination of both approaches can be utilized in order to mitigate the disadvantages of each individual process. A composite carbon foam structure can be fabricated by coating graphene oxide onto the surface of a polymer template, followed by direct carbonization. Using this method, the polymer foam can act as an inexpensive, conductive backbone for the high surface area graphene. By using different starting polymer foams, the mechanical and electrochemical properties of the carbon foam can be engineered without costly processes and steps. The surface coating of graphene is less costly than a pure graphene foam while still offering increased conductivity and available surface area.

In this work, we present a facile method to produce a one-step nitrogen-doped melamine derived carbon/reduced graphene oxide composite foam for use in LIHSs. The melamine foam precursor which is cheap and widely available foam also is rich in nitrogen. The direct carbonization of the nitrogen-rich melamine foam enables the nitrogen-doping of the final carbon foam without any additional steps. The addition of a relatively small amount of rGO (compared to pure rGO foams) allows for a higher electrode capacity without a large increase in synthesis complexity or cost. These foams can either be used directly as a negative electrode material or used as a support for other active materials, eliminating the need for additional current collectors or binders. Furthermore, the open cell nature of the carbon foam allows for greater electrolyte accessibility, increasing the electrochemical activity of the foam. The

composite foams exhibit greater performance compared to their neat counterparts, up to 330 mAh g^{-1} at a current density of 0.1 mA g^{-1}. Furthermore, they exhibit great mechanical durability and are able to recover most of its height after being fully compressed. This work also shows that the foams can be a support material for other active materials such as activated carbon due to its high surface area compared to planar electrodes such as carbon cloth or metal foils. A proof-of-concept full-cell LIHS is fabricated that shows comparable energy and power densities compared to those reported in the literature.

5.2 Experimental Methods

5.2.1 Materials Preparation

All chemicals for GO synthesis were purchased from Sigma-Aldrich and used as-received, unless otherwise noted. Melamine foam was purchased from a local retailer and cleaned by sonication successively in solutions of distilled, deionized (DDI) water, ethanol and isopropanol for 15 minutes each. Graphene oxide (GO) was synthesized using a modified Hummers' method described previously [52], [62], [123].

Graphene-coated melamine foam was prepared by coating GO onto the surface of the neat melamine foam followed by heat treatment under an inert argon atmosphere at various temperatures. The surface of the melamine foam was coated by soaking the foam in a solution of GO at a concentration of 2.5 mg mL^{-1}. To ensure even coating on the inside surface of the foam, it was squeezed while submerged in GO and then left for 5 minutes to ensure adequate diffusion time of GO into the porous foam structure. The GO coated melamine foam (MeGO) was then dried for 12 hours in a vacuum oven at 75°C and carbonized at temperatures varying from 600 – 1000°C for 30 minutes at a ramp rate of 5°C min^{-1} under an argon atmosphere. The resulting foams were then used for further characterization and testing.

In this work, the different foam samples are denoted as cMeG X where X is the carbonization temperature of the sample. As a comparison, neat foams were carbonized under the same conditions as the coated foams and are denoted as cMe X, where X is the carbonization temperature used to prepare the sample. For example, cMeG 800 denotes an rGO/melamine-based carbon foam composite that was carbonized at 800° C. Un-carbonized GO coated melamine foam was also fabricated for comparison and is denoted as MeGO.

5.2.2 Physical Characterization

Field-emmision scanning electron microscopy (FE SEM, Zeiss LEO 1530, 10 kV) and optical photography were used to characterize the morphology of the samples. X-ray diffraction (XRD, Bruker AXS D8, 0.154 nm Cu-α source) was used to determine the crystal structure of the samples. Raman spectroscopy (Brukker SENTERRA) was used to characterize the degree of oxidation of the GO on the carbonized foams. X-ray photoelectron spectroscopy (XPS) and energy-dispersive X-ray spectroscopy (EDX) were conducted in order to investigate the elemental content of the carbonized composite foams. Brunauer-Emmett-Teller (BET) analysis using a surface/pore analyzer was done to determine the specific surface area and pore distribution of the composite foams.

5.2.3 Electrochemical Characterization

All of the electrochemical testing was conducted by assembling standard CR2032 coin cells. As-prepared cMeG foams were used as the negative electrode and lithium-metal foils were used as the positive electrode for the half-cell tests. Full-cell testing was done using cMeG foam as the negative electrode and activated carbon-coated cMeG foam as the positive electrode. In both half- and full-cells, 16mm Cellgard 2500 discs were used as separators while 1M $LiPF_6$ in 1:1 ethyl carbonate and dimethyl carbonate was used as the electrolyte. The cells were

galvanostatically charged and discharged to probe their capacities, cycling stability and rate capabilities.

5.3 Results and Discussion

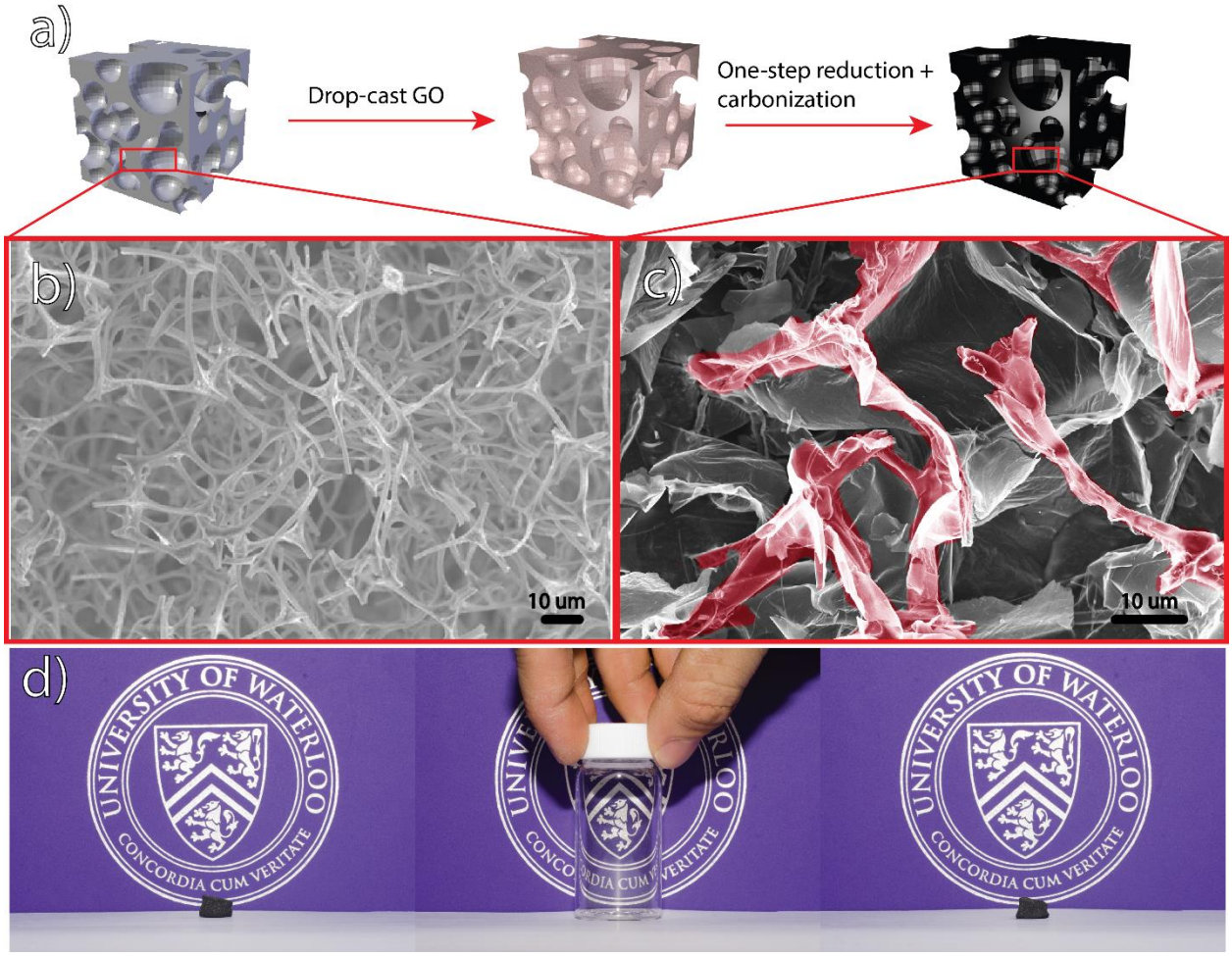

Figure 5-1 *(a) 3D representation of the cMEGX synthesis procedure, (b) SEM image of neat melamine, (c) SEM image of a representative cMEGX sample, (d) optical image of cMEG800 showing its compressibility*

Figure 5-1 shows SEM and optical images of the carbon foams. **Figure 5-1 (b)** shows the melamine foam without the addition of any graphene. The open cell structure of the carbonized melamine allows for the facile attachment of graphene onto its surface. Additionally, the

carbonized melamine foam shows good interconnectivity which helps improve electron conductivity. **Figure 5-1 (c)** shows an image of the carbonized rGO/melamine structure. The colourized portion of the image denotes the carbonized melamine framework while the rest of the image shows rGO which is identified by the characteristic wrinkling of large rGO sheets. The rGO also forms an additional interconnected network on top of the melamine framework, which can further improve electronic conductivity [121]. **Figure 5-1 (d)** shows the foam after undergoing one compression-decompression cycle. Despite being carbonized at a high temperature, the foam retains its compressive strength, able to recover 99% of its height after being fully compressed. This may be due to the short carbonization duration that preserves the structural integrity of the polymer foam backbone in addition to the added structural support provided by the rGO flakes.

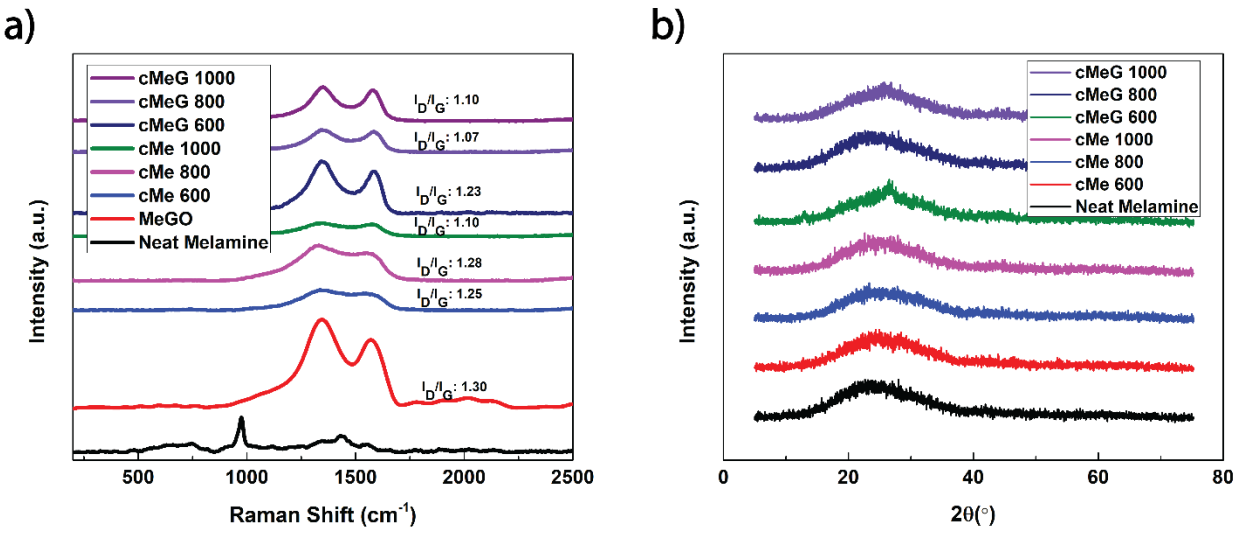

Figure 5-2 *(a) Raman spectra of neat melamine, MeGO, cMe X and cMeG X, (b) XRD spectra of neat melamine, cMe X and cMeG X*

Figure 5-2 shows the Raman spectroscopy and XRD curves of the neat melamine, MeGO, cMe X and cMeG X foams, where X denotes the temperature used to heat treat the sample. As shown in **Figure 5-2 (a)**, all samples except neat melamine exhibit peaks associated with the D and G

bands, arising from the disorder in the sp2-hybridized and stretching of the C-C structures, respectively [62], [123], [175]. The melamine sample does not exhibit these peaks because it does not possess the hybridized carbon structure. Although the cMe foams do not contain rGO, they still exhibit these peaks due to the heat treatment process in which partial graphitic structures have formed. These peaks are not well defined and are broader compared to the cMeG peaks due to the fact that the carbonization temperatures used are not high enough to induce significant graphitization. In comparison, the MeGO and cMeG samples have more clearly defined D and G peaks due to the presence of GO and rGO. In all of the aforementioned samples, the ratio of the D band intensity I_D, to the G band intensity I_G, can be calculated to estimate the degree of graphitization. It has been previously shown that the lower the I_D/I_G ratio, the greater is the graphitization of the sample [62]. The MeGO sample has the greatest I_D/I_G ratio due to the presence of GO, which has many functional groups on its surface that disrupts the graphitic structure. The I_D/I_G ratios of the cMe X samples are not significantly different than those of MeGO due to the relatively low temperatures used for the heat treatment which does not produce significant graphitization. However, the I_D/I_G ratios of the cMeG X samples are much lower than that of MeGO and cMe X samples due to the presence of rGO. The I_D/I_G ratio shows clear temperature dependence in both the rGO-containing (cMeG X) and rGO-free samples (cMe X). Generally, the extent of carbonization rises as the carbonization temperature is increased which is reflected by the decrease in I_D/I_G ratio. This decrease in I_D/I_G ratios can be explained by two different underlying mechanisms. In the cMe X samples, the decrease in I_D/I_G ratios can be attributed to the increase in graphitized carbon due to the increase in carbonization temperature. In the cMeG X samples, the decrease in I_D/I_G ratios can be explained by the same process as well as the increase in reduction of the rGO with temperature.

It is expected that the performance of the electrodes will increase with an increase of graphitic structures due to increased electrical conductivity. From the Raman data, we expect the cMeG X samples to outperform the cMe X samples. Furthermore, as the carbonization temperatures increases, we predict an increase in electrode performance.

Figure 5-2 (b) shows the XRD patterns of the cMeG 600-1000, cMe 600-1000 and neat foam samples. It can be seen that all of the samples exhibit broad peaks centered at 2θ=~25.8° which are (002) diffraction peaks typically present in carbonaceous materials. The broad peaks indicate that there may be a mixture of amorphous carbon and graphitic forms. This result is to be expected since the melamine foam will not be fully graphitized due to the relatively low temperatures used in the heat treatment process. In conjunction with the Raman spectra, this indicates that rGO is present in the samples [176].

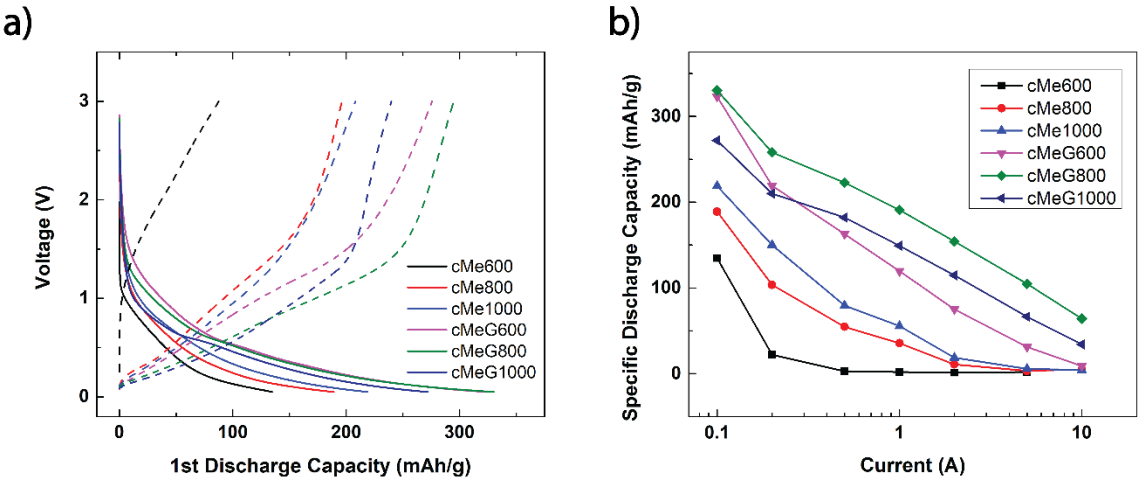

Figure 5-3 *(a) Representative charge (dotted) and discharge (solid) capacities of cMeX and cMeG at a current 0.1 A g^{-1}, (b) Specific discharge capacities of cMeX and cMeG at different currents*

Figure 5-3 (a) shows representative charge and discharge capacities of the neat and composite electrodes between 0.05 V and 3 V vs Li/Li^+ at a current of 0.1 A g^{-1}. The charge and discharge

curves shown conform to typical behaviours shown by carbonaceous materials. It can be seen that the majority of the electrodes' capacities occur below 0.5 V, which can be ascribed to two different mechanisms: lithium intercalation in-between graphene layers and lithium insertion and adsorption on non-stacked carbon layers ("house of cards" model) [4], [177]. The cMe X samples shows an increase of capacity with increasing carbonization temperature. As the temperature is increased, the fraction of melamine foam that will be carbonized increases, resulting in an increased lithium-ion storage capacity. This effect is also observed in the cMeG X samples. However, cMeG 1000 has a lower capacity than either cMeG 600 and 800 indicating that another factor is affecting the capacities which will be discussed later in this work. The capacity that occurs above 0.5 V can be ascribed to the adsorption of Li-ions on the surface of the electrodes or the basal plane of the graphene sheets [20], [177]. As the carbonization temperature increases, so does the capacity of the cMeX samples above 0.5 V. This may suggest that as the carbonization temperature is increased, so does the surface area of the sample. The trend is less apparent for the cMeG X samples which may imply that the surface area of the rGO on the sample does not change or affect the capacity after 600° C. **Figure 5-3 (b)** shows the specific discharge capacities at different currents of the neat and composite foams that were carbonized at different temperatures. A clear improvement is observed when comparing the neat carbonized foams to the composite foams. This improvement can be attributed to the additional capacity that rGO that adds to the carbon foam. Another apparent trend is the increase of the specific discharge capacity with increasing treatment temperature. This trend may be explained by the disappearance of nitrogen moieties as the temperature increases and the increase in electrical conductivity as the electrodes becomes more graphitized as explained previously. The nitrogen moieties present among the carbon structure has been shown to

improve the capacity [127], [133], [178]. However, the trend is not true for the composite foams containing rGO namely, cMeG800 and 1000. It can be seen from the graph that cMeG800 has a higher specific discharge capacity across all currents compared to other samples, which is attributed to the synergistic effect between the rGO and the nitrogen moieties in the melamine foam. As the carbonization temperature increases, the carbonized foam and rGO become more graphitic which improves conductivity and increases the capacity[127], [128], [179]. At the same time, the high temperature may decrease the amount of nitrogen moieties present in the composite foams. These two competing effects may explain why cMeG800 has higher discharge capacities when compared to cMeG1000.

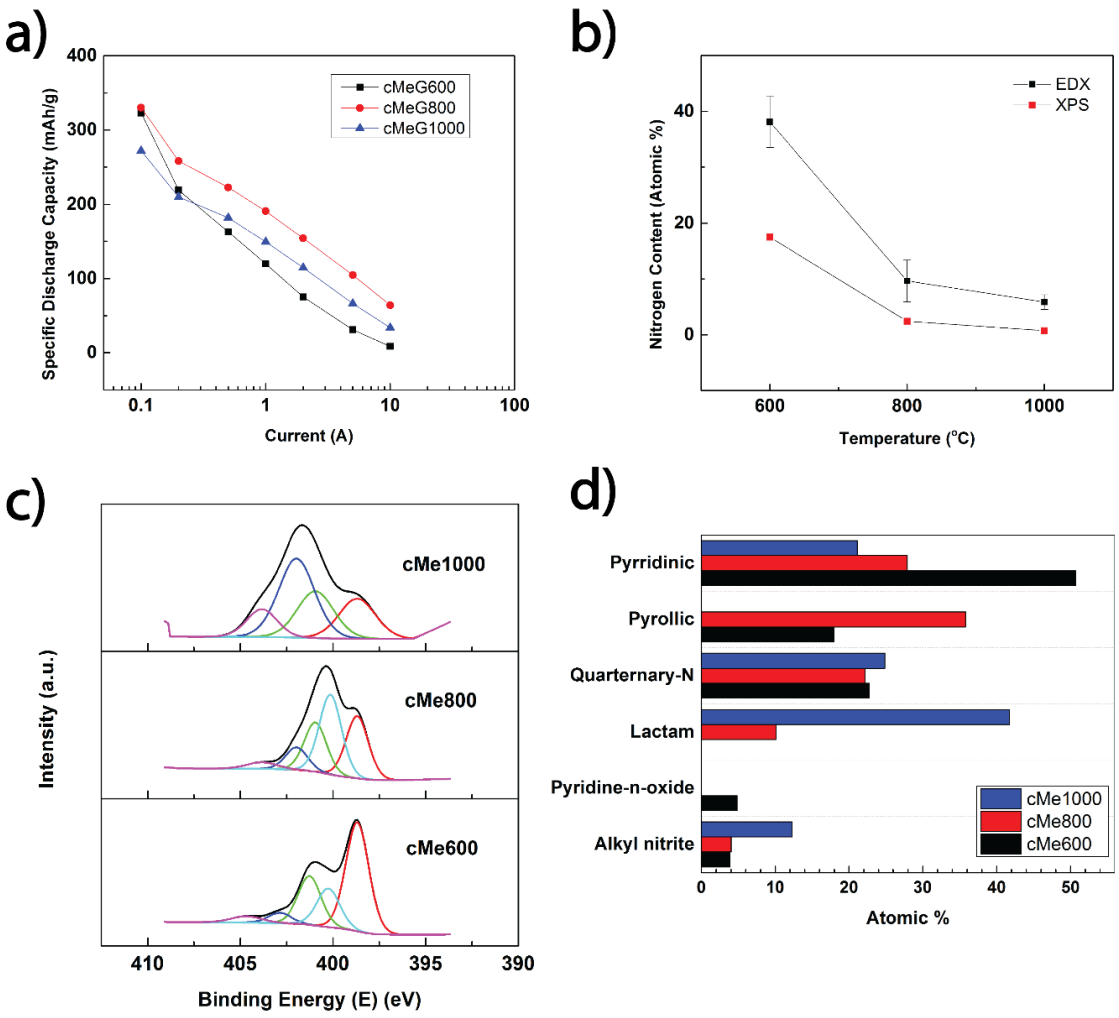

Figure 5-4 *(a) Specific discharge capacity of cMeG 600, 800 and 1000, (b) Atomic nitrogen content of the of cMeG 600, 800 and 1000 from EDX and XPS, (c) high resolution N1s peaks of cMeG 600, 800 and 1000, (d) Atomic percentages of different nitrogen moieties on cMeG 600, 800 and 1000*

To further characterize the relationship between carbonization temperature, nitrogen functional groups, and the discharge capacities, additional measurements were done on the composite foams. **Figure 5-4 (a)** shows the discharge capacities of the composite foams that were carbonized at different temperatures. **Figure 5-4 (b)** shows the effect of carbonization temperature on the nitrogen levels in these foams. The difference in the absolute values of the nitrogen in each sample can be explained by the difference in characterization technique used. XPS measures the energy of ejected electrons from the sample while EDX measures characteristic X-ray emissions from the sample. Due to the lower mean free path of electrons compared to X-rays, the penetration depth of XPS is less when compared to EDX. This difference in sampling volumes may give rise to the difference in measured nitrogen content in the composite foam. This implies that there is a much higher nitrogen content in the bulk of the foam compared to the surface. The trends with respect to the nitrogen contents is the same regardless of the characterization technique used. As the carbonization temperature increases, the nitrogen content generally decreases. Since nitrogen has been shown to help increase capacity [127], [178], [178], [179], [179]–[181], it can be expected that the capacities of the composite foams will decrease as the carbonization temperature increases. However, this is not the case as shown in **Figure 5-4 (a)**. As explained previously, the results shown in **Figure 5-4 (a)** may be explained by 2 factors. First, the degree of graphitization and reduction of GO tend to rise as the carbonization temperature increases. As the temperature increases, both of these effects lead to better electronic conductivity and performance. On the other hand, the degree of nitrogen doping is inversely related to the carbonization temperatrure. As the temperature

increases, the less stable nitrogen moieties will disappear or be converted into more stable nitrogen moieties which may affect the performance. In order to investigate this effect, XPS was used to analyze the types of nitrogen moieties present on the composite foams. **Figure 5-5 (c)** shows the deconvoluted high resolution N1s spectra for cMeG 600, 800 and 1000 while **Figure 5-5 (d)** shows the nitrogen moieties that are associated with the binding energies of the peaks. The deconvoluted spectra shows 6 distinct peaks that can be associated with the following nitrogen moieties: pyrridinic (~398.7 eV), pyrollic (~400 eV), quaternary-nitrogen (~401.2 eV), lactam (~402 eV), pyridine-n-oxide (~402.9 eV) and alkyl nitrites (~404.4 eV). As the two figures show, the composition of the nitrogen moieties changes with carbonization temperature which can be explained by their differing thermal stabilities. As shown in **Figure 5-5 (d)**, the most common form of nitrogen in the composite foams is pyrridinic. Pyrridinic nitrogen is also shown to be the least stable as the atomic percentage decreases with increasing carbonization temperature. Comparing this data to the **Figure 5-4 (a)**, it can be seen that at 600 and 800°C, the discharge capacities at low currents are actually similar but are higher than at 1000°C. However, as the current increases the performance of cMeG 600 starts to decrease when compared to cMeG 1000. Generally, pyrridinic nitrogen may help lithium-ion storage at lower currents but contribute less at higher currents. The data also suggests that quaternary nitrogen does not significantly alter the performance of the composite foams as all of the composite foams show similar atomic percentages of quaternary nitrogen. As the carbonization temperature is increased, the nitrogen moieties appear to preferentially convert into lactams and alkyl nitrites. Compared to cMeG800, cMeG1000 has a much higher atomic percentage of these nitrogen moieties while having a lower rate performance. This suggests that lactams and alkyl nitrites do not help improve the electronic properties of the sample nor does it improve the

lithium-ion storage capabilities. The data suggests that both degree of graphitization and nitrogen content (both type and amount) are affected by the carbonization temperature and that there reaches an optimal levels between 600°C and 1000°C.

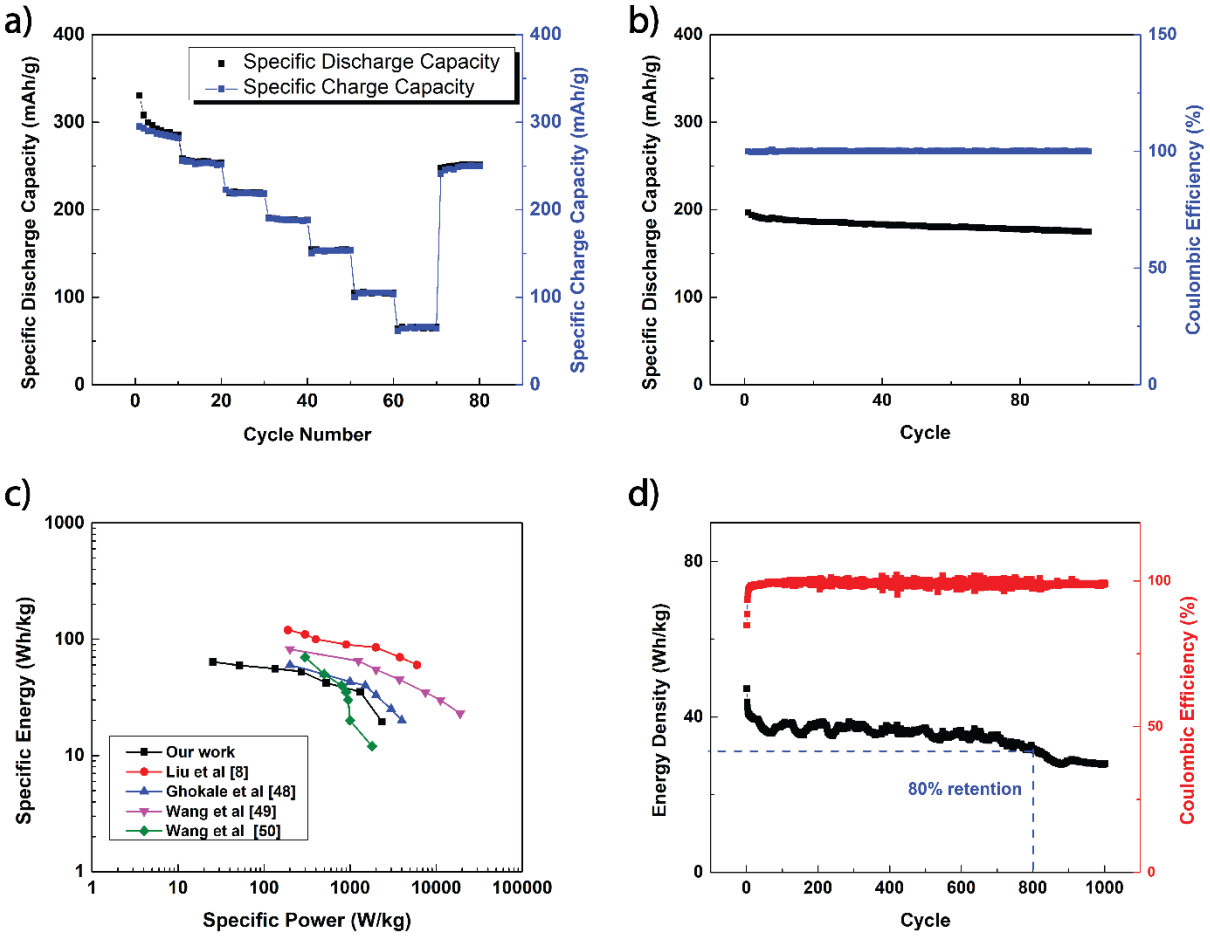

Figure 5-5 *(a) Specific charge and discharge capacities of cMeG 800 at different currents, (b) Specific discharge capacity and coulombic efficiency of cMeG 800 at 1 A for 100 cycles, (c) Ragone plot of different LIHSs in literature compared to the present work, (d) Energy density and coulombic efficiency of an LIHS full made from cMeG800 at 1 A over 1000 cycles.*

Figure 5-5 shows additional electrochemical characterization using of best performing sample shown previously i.e, cMeg 800. **Figure 5-5 (a)** shows the specific discharge capacities of the electrode at different currents. The initial discharge capacity of the electrode reaches 330 mAh g^{1} before quickly decreasing, stabilizing at 290 mAh g^{-1}. The initial rapid drop of capacity can

be attributed to an irreversible reaction whereby the solid electrolyte interphase (SEI) is formed. **Figure 5-5 (b)** shows the specific discharge capacity of the electrode at 1 A over 100 cycles. Even after 100 cycles, the discharge capacity is still stable and retains 89% of its initial value (197 mAh g^{-1}) while maintaining 100% coulombic efficiency. This shows that the electrode has excellent stability. A LIHS was also fabricated using cMeG 800 as the negative electrode and commercially available activated carbon coated onto cMeG 800 as the positive electrode. During charging, Li^+ ions intercalate into the cMeG negative electrode while PF_6^- ions form a double-layer on the interface of activated carbon that has been pasted onto cMeG and the electrolyte. During discharge, the opposite occurs where Li^+ ions are driven out of the cMeG electrode and PF_6^- ions desorb from the activated carbon/electrolyte interface. The voltage window of the LIHSs in this work has been constrained to lie between 2 V and 3.9 V. **Figure 5-5 (c)** shows a Ragone plot comparing the performance of this cell to that of recent LIHSs reported in the literature. The energy density of the cell is calculate via the following formula:

$$E = \frac{\int_0^t V(t) i \, dt}{3600 \, m} \qquad (5\text{-}1)$$

Where E is the specific energy of the cell, V(t) is the voltage profile of the cell during discharge, i is the current drawn and m is the combined whole electrode mass of both the cathode and anode (~10.8 mg). The practical specific power of the cell can be calculated by:

$$P = \frac{E}{t} \qquad (5\text{-}2)$$

where P is the specific power of the cell, E is the specific energy of the cell and t is the discharge time of the cell. Note that the electrode mass only includes the mass of the active materials since the composite foam does not require any binders, conductive agents or current collectors. The work presented in this paper is comparable to those in literature [28], [45], [153], [182],

especially when taking into account the absence of metal-oxides in this work. The performance of the cMeG electrodes can be further improved by incorporating metal oxides or other active materials. The porous structure of the 3D cMeG makes it easier to deposit or grow other materials on the surface in order to further tailor its electrochemical properties. **Figure 5-5 (d)** shows the energy density of the full cell based on the discharge cycle at 1 A for 1000 cycles. The full cell maintains an energy density of approximately 40 Wh kg^{-1} and coulombic efficiency of 100% even after 500 cycles, highlighting the one of the main advantages of the LIHS. The stability exhibited by the full-cell device is typically seen only in supercapacitor devices and not LIBs but still requires further improvement order to meet the current standards. The LIHS also retains 80% of its initial energy density after 800 cycles and decreases to 68% after 1000 cycles.

5.4 Conclusions

In this work, we have successfully synthesized compressible carbon/graphene composite foam by direct carbonization of melamine foam combined with graphene oxide. As-prepared foam can be used directly as an electrode in LIHSs and LIBs as an anode material, giving a capacity of 330 mAh g^{-1} at 0.1 A. The composite foam can also be used as a supporting framework for other active materials such as activated carbon and other metal oxides. We have shown that a full-cell LIHS using the as-prepared composite foam as the negative electrode combined with the same foam covered with activated carbon as the positive electrode has comparable performance to those reported in literature. Furthermore, the electrodes presented in this work required no binders or extra additives. The facile preparation allows for easy addition of other active materials without the need for complicated synthesis steps.

5.5 Further Work

At the time of writing, the work and data presented in the following section has not been published in a refereed journal.

To further show the versatility of the composite material, we explored its capabilities for use in a EDLC supercapacitor system. Interestingly, we have found that the electrode that performs the best as an negative electrode was not the same electrode that provides the best performance when used as an EDLC electrode. **Figure 5-6** shows a comparison of CMEG800 and CMEG900 when used in an EDLC system with a 6M KOH electrolyte. We can observe that there is a clear increase in capacitance, shown by the increased area under the curve, when the carbonization temperature is increased.

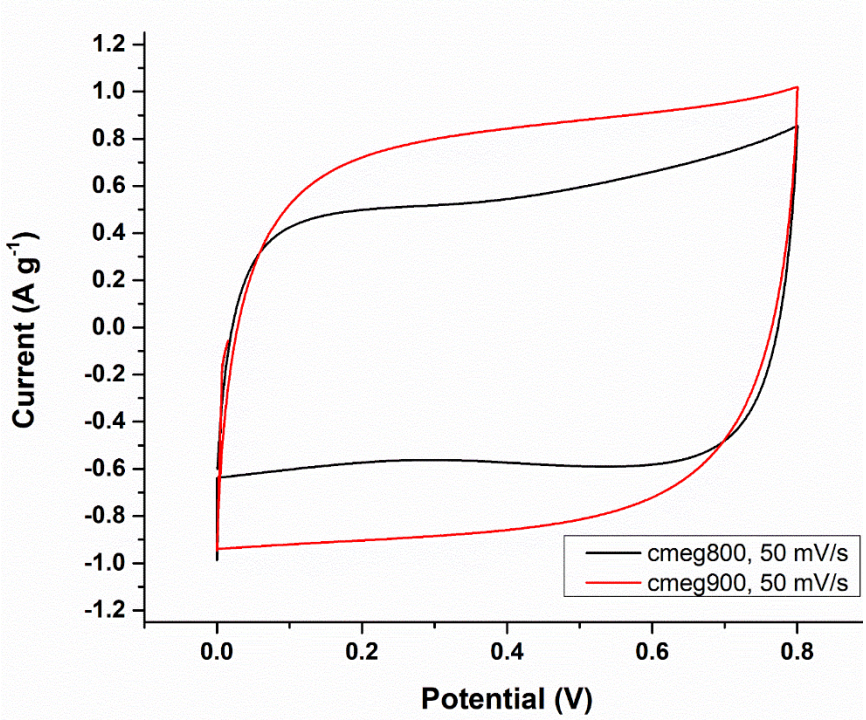

Figure 5-6 *CV Curves of EDLC supercapacitors made with composite foams carbonized at 800ºC and 900ºC*

The presence of graphene in the composite foam also increases capacitance of the composite foam. **Figure 5-7** shows the CV curves and the Nyquist plots of the full cell supercapacitors made with CME900 and CMEG950. **Figure 5-7 a)** clearly shows that the presence of graphene nearly doubles the capacitance (area under the curve). **Figure 5-7 b)** shows the Nyquist plot obtained from EIS and shows that the composite foam has lower charge transfer resistance, approximated by the width of the semi-circle portion of the plot, compared to the carbonized melamine foam without graphene. This can be explained by the presence of the graphene on the surface of the foam which has a synergistic effect with the underlying carbon foam to facilitate electron transfer for ion adsorption.

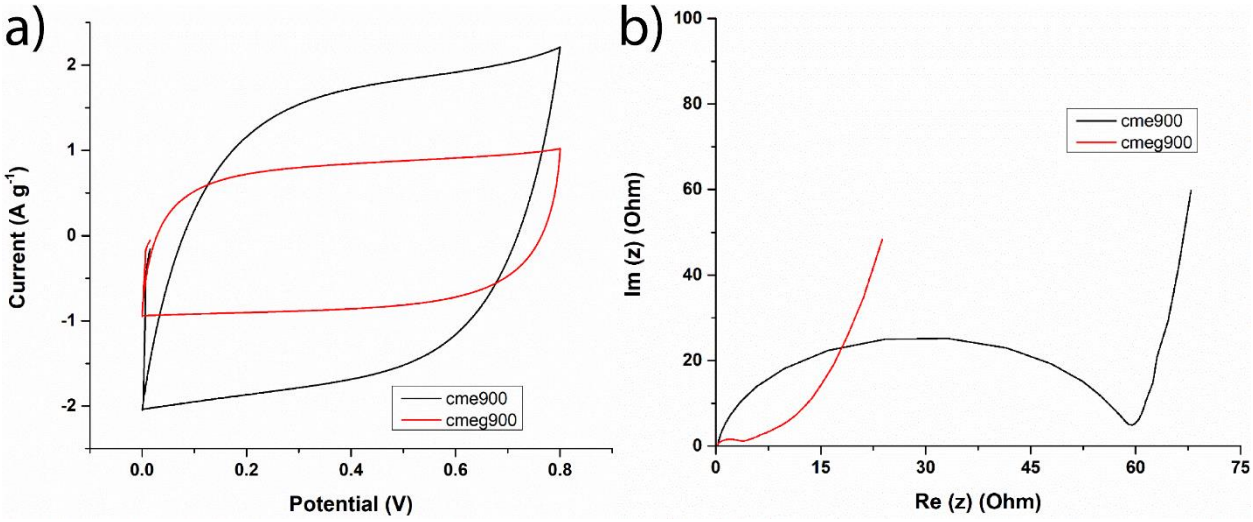

Figure 5-7 *Comparison between CMEG900 and CME900 supercapacitors, a) CV curves, b) Nyquist plot*

We propose that an optimal carbonization temperature for optimal performance in EDLC supercapacitors may exist. Consequently, we tested this hypothesis by fabricating EDLC supercapacitors using composite foams carbonized at different temperatures. **Figure 5-8** shows the CV curves of EDLC supercapacitors made with as-prepared composite foams carbonized at different temperatures with a 6M KOH electrolyte in a coin cell. While CMEG800 performs the best as a negative electrode in a lithium-ion hybrid supercapacitor, CMEG950 performs the best in the EDLC system. This can be explained by the increase in conductivity due to the increased carbonization of the sample when the heat treatment temperature is increased. In similar fashion to the lithium-ion hybrid supercapacitor system that will be discussed later in the chapter, an optimal carbonization temperature exists as the performance of the foam carbonized at 1000^{o}C decreases when compared to the lower temperatures. Since the higher carbonization temperature decreases nitrogen content in the composite foam (**Figure 5-4 (b)**), this suggests that the nitrogen moieties is beneficial to the performance of the EDLC and the higher carbonization temperature causes too much of the nitrogen to be driven off, causing a decrease in performance.

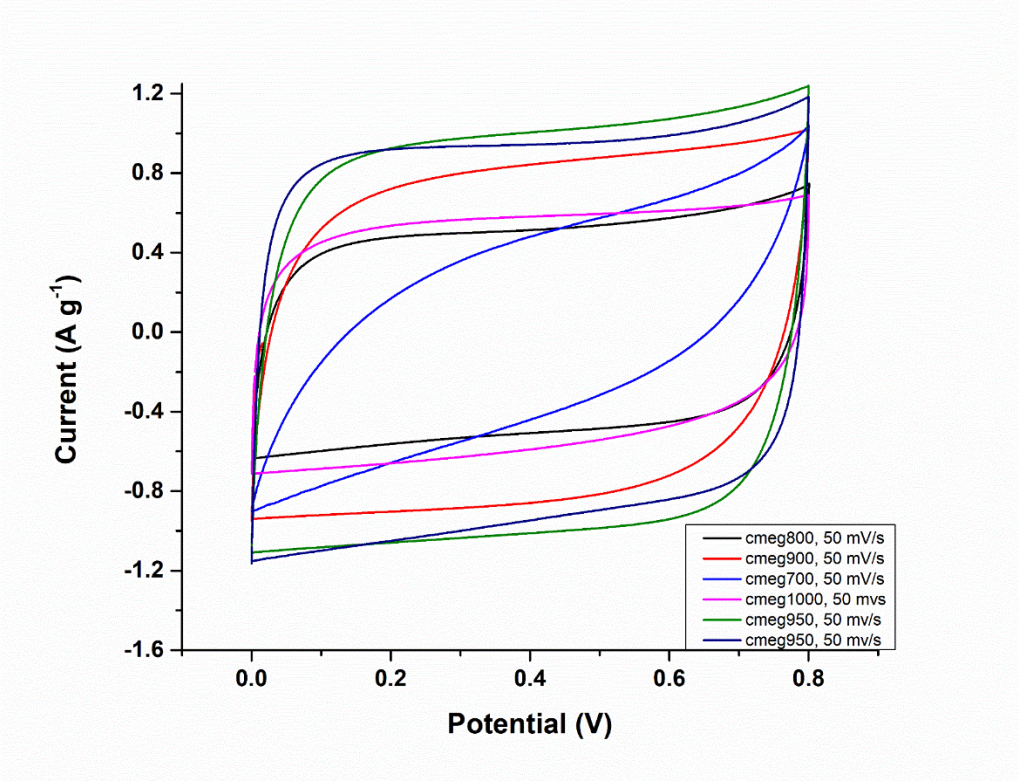

Figure 5-8 *CV curves of a full EDLC supercapacitor system based on the composite foams carbonized at different temperatures using a coin cell*

The best performing composite foam, CMEG950, was then used to fabricate a flexible full-cell device. **Figure 5-9** shows a schematic illustration of the flexible cell configuration. Instead of a monolithic composite foam piece, each electrode is comprised of smaller pieces of the foam that is backed with a flexible polymer substrate. This allows for the distribution of the mechanical bending stresses to the polymer backing instead of the foams, mitigating the risk of breaking when compared to a single monolithic foam design.

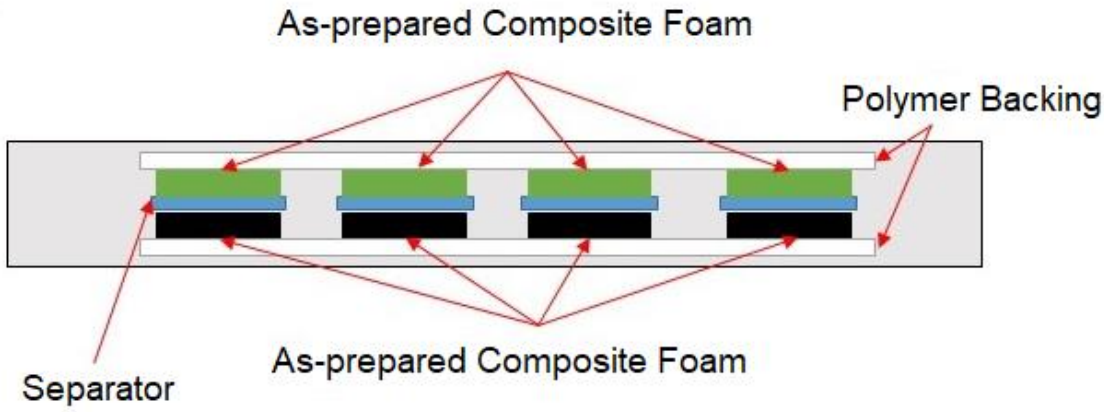

Figure 5-9 *Schematic Illustration of the flexible cell configuration using the composite foam*

Figure 5-10 a) shows the proof-of-concept electrode fabricated using CMEG950 on a PET backing with a copper current collector. The 2 electrodes shown in the figure were then soaked with 2M KOH/PVA electrolyte and sandwiched with a cellulose separator in between without any additional pressure. **Figure 5-10 b)** shows the CV curves for the device at different scan rates from 20 to 500 mV s^{-1}. The shape of the curve is rectangular only at the lower scan rates, showing a more resistive behaviour as the scan rate is increased. This result is contrary to the half-cell electrode data which was obtained using a coin cell system with 6M KOH as the electrolyte.

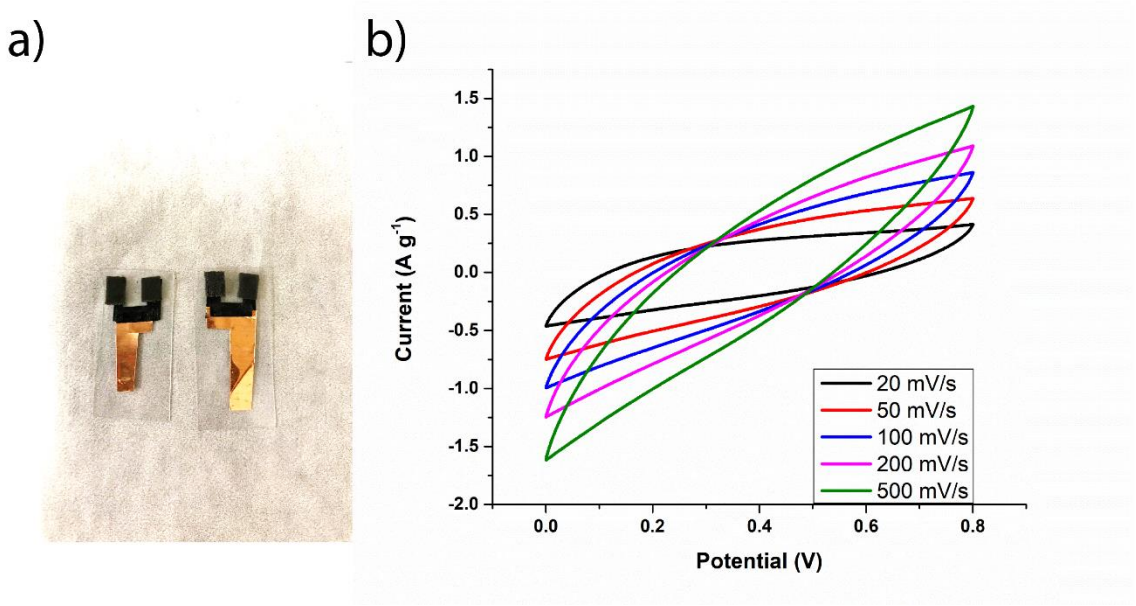

Figure 5-10 *a) EDLC electrodes made from CMEG950 with a PET backing and a copper current collector, b) CV curves of the as-prepared electrodes with 2M PVA/KOH and a cellulose separator*

We suspect that the problem is caused by two factors: the low amount of pressure present in the system, leading to contact resistance between the electrodes and the PVA/KOH electrolyte compared to aqueous KOH. **Figure 5-11** shows full-cell CVs fabricated using CMEG950 with different configurations (coin cell and flexible cell shown previously) and electrolytes (6M KOH and 2M KOH/PVA). **Figure 5-11 a)** shows the best performing full cell which was operated with an aqueous 6M KOH solution. The shape of the CV curve shows a typical rectangular shape which is expected in supercapacitor systems. **Figure 5-11 b)** shows the full cell fabricated in a coin cell format with the gel electrolyte. The shape of the curve is less rectangular than that of the coin cell with an aqueous electrolyte. Additionally, the areas under the curve is less, corresponding to lower capacitance. These two differences can be explained by the difference in electrolyte. The aqueous system will exhibit less ionic resistances and faster ion diffusion, resulting in better overall performance. Comparison of **Figures 5-11 b)** and **c)**,

shows evidence of degradation in performance which can be explained by the lack of pressure in the flexible cell compared to the coin cell.

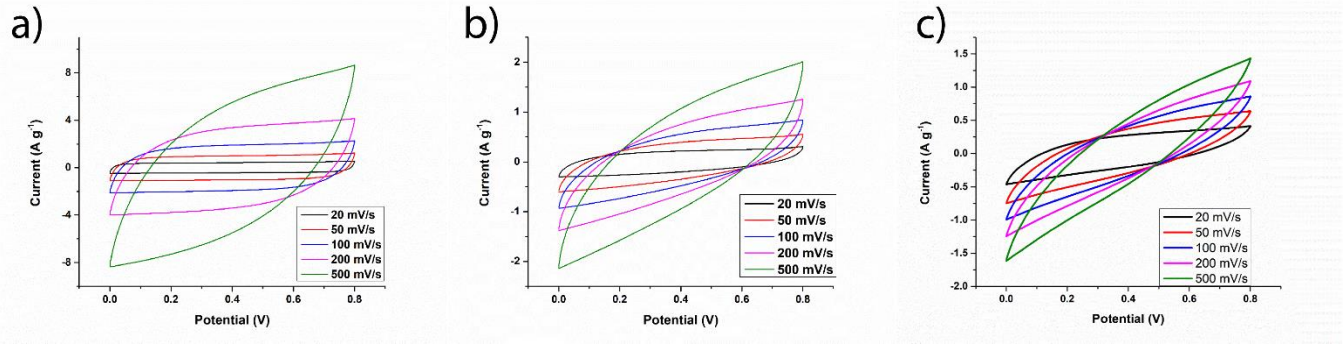

Figure 5-11 Full-cell CVs with CMEG950 with different electrode and cell configurations. a) 6M KOH, coin cell, b) 2M KOH/PVA, coin cell, c) 2M KOH/PVA flexible cell

Table 5-1 shows a summary of the capacitance values obtained with the 3 different cells. We can see that the coin cell with 6M KOH performs the best at low and high scan rates. Both the coin cell and the flexible cell with 2M KOH/PVA exhibits similar performances at the lower scan rate. However, the coin cell retains more of its initial capacitance at the higher scan rate which is due to the lack of contact pressure in the flexible cell, which increases contact resistance as previously mentioned. However, even the capacitance of the coin cell with 6M KOH is low compared to that of other carbonaceous materials, such as activated carbon, which have typical practical capacitances of about 100 F g^{-1} [183]. This may be due to the low accessible surface area for ionic adsorption, which is especially important for EDLC supercapacitors. Therefore, one major area of improvement would be to increase the surface area of the foam, possibly by an activation process that forms pores on the graphene surface or by introducing other high surface area and porous carbon materials such as activated carbon.

Table 5-1 *Summary of capacitance values obtained from the different cell configurations with CMEG950*

Sample	**Scan Rate (mV s^{-1})**	**Capacitance (F g^{-1})**
Flexible Cell, 2M KOH/PVA	20	9.2
Coin Cell, 2M KOH/PVA	20	8.7
Coin Cell, 6M KOH	20	20.3
Flexible Cell, 2M KOH/PVA	200	1.5
Coin Cell, 2M KOH/PVA	200	2.8
Coin Cell, 6M KOH	200	13.5

6.0 All-carbon flexible supercapacitors based on electrophoretic deposition of graphene quantum dots on carbon cloth

---

Chapter 6 is based on submitted work by Tjandra et al. in the journal *Journal of Power Sources*.

R. Tjandra, W. Liu, M. Zhang, A.Yu. "All-carbon flexible supercapacitors based on electrophoretic deposition of Graphene quantum dots on carbon cloth". (Submitted to *Journal of Power Sources*)

See **Statement of Contributions** for a detailed summary of contributions from each co-author.

In this chapter, graphene quantum dots are produced via a simple peroxide-assisted hydrothermal cutting of graphene oxide. The resulting graphene quantum dots have lateral sizes of less than 20 nm and are composed of few layered graphene sheets. Electrophoretic deposition is used to deposit the quantum dots onto the surface of carbon cloth. Carbon cloth was chosen due to its inherent mechanical stability, flexibility and electronic conductivity, as shown previously in **Chapter 4**. We can produce an even coating of quantum dots on the surface of the carbon cloth; however, we encountered difficulty in obtaining high mass loadings. Despite the low mass loadings, we can achieve high areal capacitances of approximately 70 mF cm^{-2}. At the time of writing, our performance ranks among the highest in flexible electrodes using graphene quantum dots as an active material. We also used the as-prepared electrodes in flexible full cells that exhibits remarkably high rate performance, can bescanned at a rate of up to 5000 mV s^{-1}.

6.1 Introduction

Supercapacitors are a type of electrochemical energy storage device that have high power densities and low energy densities compared to conventional batteries [184], [185]. Supercapacitors can be broadly categorized in the way the active materials store energy. electric double layer capacitance (EDLC) supercapacitors store charge by physical adsorption of ions on the surface of a high surface area material. Pseudocapacitors store charge through redox reactions, similar to conventional batteries. However, the difference between pseudocapacitors and batteries is that the redox reactions in pseudocapacitors occur on a faster time scale and are usually confined to the surface of the active materials. In either case, both EDLC and pseudocapacitors can reach higher power densities than batteries due to the fast reactions. Recently, a great deal of effort has been put put into flexible energy storage systems, including flexible supercapacitors [29], [69], [93], [109], [122], [128], [186]–[191]. Research on flexible energy storage systems has been on the upswing especially with the recent surge in popularity of wearable and flexible electronics and sensors. Flexible energy storage systems are defined as energy storage systems that can be mechanically flexed, stretched or twisted without significant performance degradation. Supercapacitors have the potential to be made flexible but face certain challenges that must be overcome before they can be commercially realized. One of the current challenges is to develop flexible electrodes that can match the performance of the conventional electrodes. Typically, supercapacitor electrodes are constructed by pasting active materials onto a metal foil current collector. These electrodes are then wound or stacked together and separated by a polymer separator. The electrolyte, usually in liquid form is then added and the assembly is packaged to form individual cells. These cells are usually packaged

in a sealed aluminum can or a laminated aluminum pouch. The former packaging method is inherently rigid while the latter can be used for flexible cells. The two main roadblocks to flexible cells are the development of flexible electrodes and the development of non-liquid electrolytes[191]–[193]. Much effort has been devoted to the development of flexible electrodes using carbon based nanomaterials. These efforts can generally be categorized by the dimensionality of the resulting flexible electrode: 1-D to 3-D. 1-D electrodes usually are made by using a polymer fiber as a supporting material for the active material which is decorated on its surface or by fabricating a free-standing fiber using the active material itself[29], [190], [194]–[197]. 2-D electrodes usually involve the formation of a fibrous mat or paper electrode with or without additional active materials [70], [93], [189], [198], [199]. 3-D electrodes are usually made by fabricating a carbonaceous foam which can be used as-is or combined with additional active materials[28], [77], [121], [127], [127], [129], [167], [200], [201]. Although each format has their own advantages and disadvantages, this work focuses on the use of carbon cloth (2-D) due to its mechanical robustness, electrical conductivity, low cost and ease of handling[109], [192], [202]–[204]. The main disadvantage of carbon cloth is that it has a low-surface area compared to some other materials. However, by combining it with a high surface area material, it is possible to greatly increase the performance of carbon cloth as a supercapacitor electrode while still retaining its flexibility and robustness.

GQDs are a relatively new class of carbonaceous nanomaterials with several interesting properties such as high surface area and photoluminescence[81], [83], [86], [92], [186], [205]–[207]. GQDs can be synthesized using the bottom-up method by the controlled assembly of small carbon molecule such as citric acid. The bottom-up approach is advantageous because of its high degree of controllability and precision at the expense of more complicated reaction

steps. The top-down approach involves the exfoliation and subsequent cutting of bulk graphite into GQDs, often with GO or rGO as an intermediate[85], [87], [92], [206]–[208]. Due to its high surface area-to-volume ratio, GQDs are an excellent candidate materials for use in supercapacitors. In this work, GQDs produced via a one-pot, hydrogen-peroxide assisted hydrothermal reaction are used in conjunction with carbon cloth in order to form a flexible supercapacitor electrode with high rate capabilities. Electrophoretic deposition is used to deposit nano-sized GQDs onto the surface of carbon cloth, greatly increasing its capacitance without modifying its mechanical properties. We have produced a fully flexible, free-standing, binder free electrode that shows excellent performance even at a low mass loading, especially compared to other purely carbon based material, achieving a relatively high areal capacitance of 70 mF cm^{-2}. A symmetric full-cell was also fabricated using 2 as-prepared electrodes. The symmetric capacitor which achieved a high areal capacitance of 24 mF cm^{-2} and is also fully flexible, showing similar areal capacitances in its flexed and un-flexed states.

6.2 Experimental Methods

All chemicals were purchased from Sigma Aldrich and used as-is. Carbon cloth was purchased from Fuel Cell Earth and treated with concentrated HNO_3 to remove any manufacturing residues and make it hydrophilic.

6.2.1 Graphene Oxide and Graphene Quantum Dots Synthesis

GO was synthesized by a modified Hummers' method previously published [201]. In short, small flake graphite (2-15 um flake size, Alfa Aesar) was oxidized using a mixture of H_3PO_4 (85 wt%, Sigma Aldrich), H_2SO_4 (98 wt%, Sigma Aldrich) and $KMnO_4$ (Sigma Aldrich) for 16 hours while being continually stirred at 50°C. Distilled, de-ionized (DDI) water was then added to dilute the acid and stop the reaction. H_2O_2 (30%, Sigma Aldrich) was then added to remove

any unreacted $KMnO_4$. The resulting GO suspension was then washed with ethanol and water and finally freeze-dried for storage.

To produce the GQDs, 50 mg of freeze-dried GO was mixed with DDI water and 30% hydrogen peroxide in various ratios for 30 minutes while being stirred. The resulting mixture was then transferred to a Teflon-lined steel autoclave and placed in an oven at 170°C for 5 hours and then naturally cooled to room temperature.

6.1.2 GQDs/Carbon Cloth Electrode Preparation

To produce the composite electrodes, electrodeposition was conducted using a 2-electrode system. Carbon cloth was used as the working electrode, platinum as the counter electrode and the as-prepared GQDs suspension as the electrolyte. The deposition was conducted at 10 VDC over various durations ranging from 30s to 3 hours. The as-prepared carbon cloth/GQDs electrodes were then gently washed using DDI water to remove any excess GQDs solution.

6.2.1 Physical Characterization

UV-Vis absorbance spectra of the GQDs were measured using a UV-Vis spectrophotometer (Thermoscientific Genesys 10, 190 nm – 800 nm scan range). The photoluminescence characteristics of the GQDs were measured using a fluorescence spectrometer (Perkin-Elmer LS 55, xenon lamp, 240 nm – 800 nm scan range, various excitation wavelengths). The lateral and vertical size of the GQDs were measured using atomic force microscopy (Bruker Innova). The morphology and nanostructure of the GQDs/carbon cloth electrodes were characterized using field-emission scanning electron microscopy (FE-SEM, Zeiss LEO 1530, 7 kV).

6.2.2 Electrochemical Characterization

Half-cell characterization was done using a 3-electrode configuration with a potentiostat (Biologic VSP-300) to obtain cyclic voltammograms (CV) and electrochemical impedance spectroscopy (EIS) curves. The cell consisted of as-prepared carbon cloth/GQDs samples were used as the working electrode, platinum foil as the counter electrode, Ag-Ag/Cl as the reference electrode with 1M H_2SO_4 as the electrolyte.

A full-cell supercapacitor was made using two carbon cloth/GQDs composite electrodes in a sandwich configuration separated by cellulose filter paper with a PVA/H_2SO_4 gel as the electrolyte. The gel electrolyte was made by dissolving 10 wt% of PVA in water at an elevated temperature. Once the PVA was fully dissolved and cooled to room temperature, 10 wt% concentrated H_2SO_4 was added under vigorous stirring. The full-cell was characterized using CV, chronopotentiometry and EIS (Biologic VSP-300).

6.3 Results and Discussion

Figure 6-1 a) shows a schematic illustration of the synthesis of the GQDs. The H_2O_2 acts as a chemical scissor which cuts the GO along the epoxide functional groups [88], [209]. This results in small GO particles that are less than 20 nm in both lateral and vertical directions. **Figure 6-1 b)** shows an AFM scan of the as-prepared GQDs deposited on a piece of mica. It can be seen that the GQDs form small aggregates, likely due to the solution casting method in order to prepare the sample for AFM. Using software analysis, the lateral size of the GQDs is between 10-20 nm which is orders of magnitude smaller than the starting graphite material (2-15 μm). The height of the individual GQDs also show that the GO was further exfoliated during the hydrothermal synthesis process. The sizes of the GQDs presented here fit well with the sizes of

GQDs reported in the literature [208], [209]. To further confirm that the GQDs synthesis was successful, the UV-Vis absorbance and photoluminescence (PL) characteristics of the GQDs were investigated. **Figure 6-1 c)** shows a representative PL spectrum of the GQDs with a stimulation wavelength of 310 nm and the resulting UV-vis absorbance. The absorbance spectrum exhibits a sharp peak around 254 nm. It has been shown that GO shows an absorbance peak around 230 nm that shifts to around 260nm when it is reduced to rGO. Based on this, the GQDs have an absorbance closer to that of rGO, suggesting that the hydrothermal cutting of GO to GQDs also has leads to some reduction.

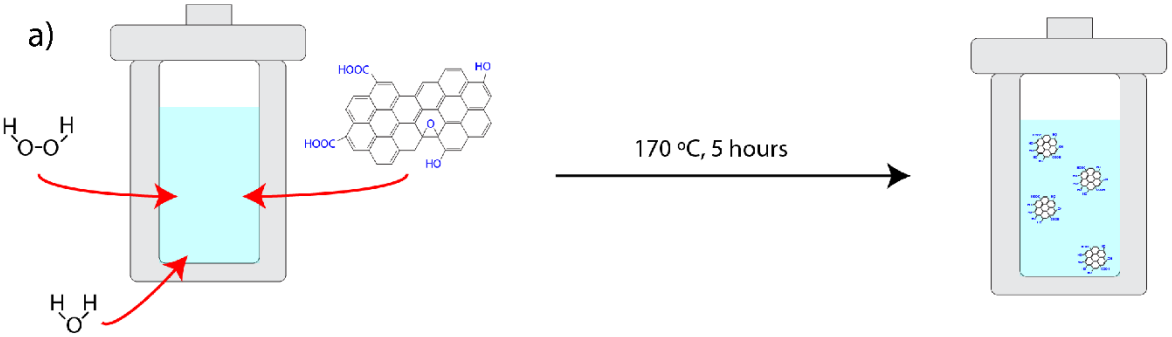

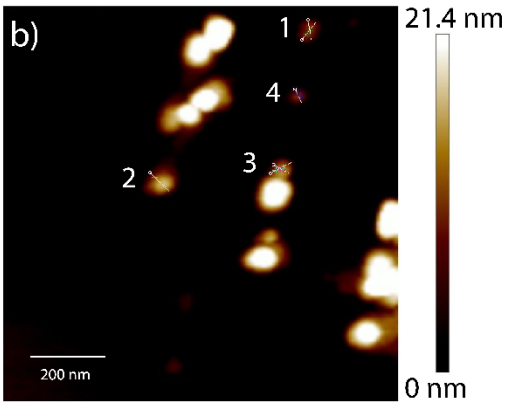

Particle	Lateral Size (nm)	Height (nm)
1	16	1.43
2	10	3.13
3	21	5.63
4	9	1.34

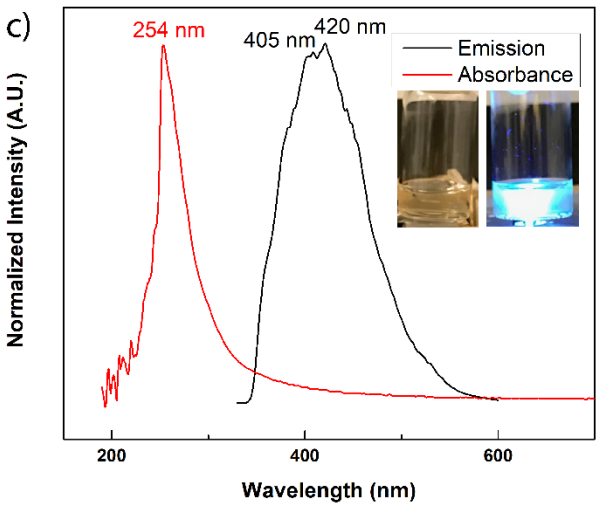

Figure 6-1 *a) Schematic illustration of GQDs synthesis, b) AFM image of GQDs with particle size analysis, and c) UV-Vis absorbance spectra (red) and photoluminescence spectra (black) of the GQDs with the inset showing the neat GQDs solution (left) and photoluminescence of the same solution under illumination with UV light at a wavelength of 365 nm (right).*

In order to test the GQD viability as a supercapacitor electrode, the as-prepared samples were electrodeposited onto carbon cloth. Carbon cloth was chosen due to its conductivity, flexibility and ease of handling. In order to improve the wettability of the carbon cloth, it was subjected to a nitric acid pre-treatment. The nitric acid treatment renders the carbon cloth hydrophilic due to the introduction of oxygen functional groups on its surface. The nitric acid treated carbon cloth was then used as the working electrode in a 2-electrode setup with a piece of platinum foil as the counter electrode. A potential of 10 VDC was then applied across the setup using a potentiostat which induces a the accumulation of positive charge in the carbon cloth electrode. This charge accumulation induces an electric field which attracts the negatively charged GQDs to the surface of the carbon cloth. **Figure 6-2 a)** shows a schematic illustration of the electrodeposition process). SEM images of neat carbon cloth and the resulting GQDs/carbon cloth composites were obtained in order to confirm the successful deposition of GQDs. **Figure 6-2 b) - c)** show the surface of the neat carbon cloth while **Figure 6- 2 d) – e)** show the surface of a representative GQDs/carbon cloth sample (the same GQDs were used in the AFM scan). **Figure 6-2 b) and c)** shows that the surface of the neat carbon cloth is relatively smooth and free of surface features, even after nitric acid treatment. Particles can be clearly seen in **Figures 6-2 d) and e)** (coloured for clarity), indicating that GQDs was successfully deposited on the surface of carbon cloth. The SEM images show that a relative uniform, monolayer coverage of the GQDs on the surface of carbon cloth has been achieved. This allows for a greater surface area of the GQDs to be accessed by the electrolyte during charge and discharge. The monolayer coverage also explains the low mass loadings of GQD on the carbon cloth in the final composite electrode. The SEM confirm that the GQDs are ~10 nm in size which corroborates the estimates from the AFM scans.

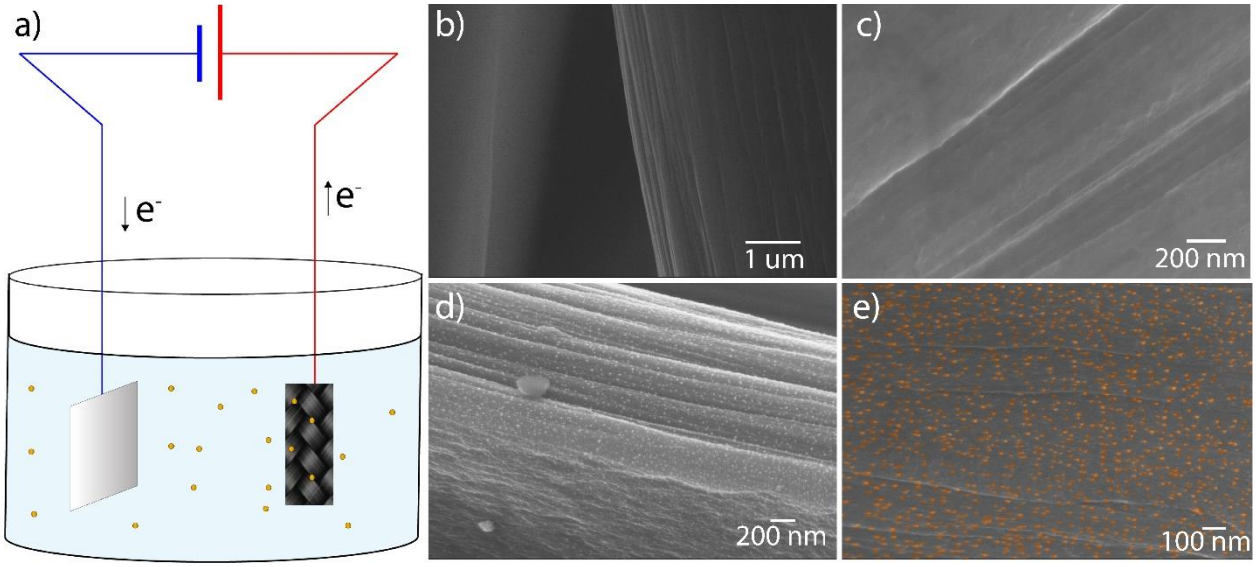

Figure 6-2 *a) Schematic illustration of GQDs deposition onto carbon cloth, and SEM images of b)-c) neat carbon cloth, d) – e) GQDs/Carbon cloth composite electrode.*

The as-prepared GQDs/CC electrodes were then used as the working electrode in a 3-electrode setup with platinum foil as counter electrode, Ag/AgCl reference and 1M H_2SO_4 as the electrolyte. Generally, the electrodes exhibit rectangular CV shapes which conforms to the behaviour of typical supercapacitor electrodes. The CV curves also include redox peaks which may be attributed to the oxygen functional groups present on the GQDs from the GO synthesis process. The deposition times of the GQDs on CC was varied in order to investigate the effects on the capacitance of the electrodes. **Figure 6-3 a)** shows the CV curves of the composite electrodes with different deposition times at a constant voltage of 10 VDC at a scan rate of 50 mV s^{-1}. **Figure 6-3 a)** clearly shows that the capacitance of the electrodes increases with the deposition time up to 1800s while the capacitance of the electrode decreases when the deposition time is further increased. This decrease may be caused by the agglomeration of the GQDs agglomerate with extended deposition times, reducing their available surface area for

ion adsorption. It can also be seen that the sample obtained after a deposition time of 1800s exhibits a broad redox peak at ~0.5 V and 0.35 on the reverse scan. The broad peaks suggest a pseudocapacitative component that could arise from the reactions involving oxygen functional groups present on the surface of the GQDs [94], [210], [211]. It is interesting to note that the sample produced by our 3600s deposition exhibits no such peak while the 300s and 1200s samples exhibit small peaks suggesting a different redox mechanism at play. The different peaks can be explained by the change of functional groups formed on the GQDs caused by the reduction process during electrodeposition [212]. Since the applied potential have a reductive effect, a chance in deposition times will cause a change in composition in oxygen functional groups. As the deposition times increase, the GQDs will be reduced further, inducing a change in both the type and amount of oxygen functional groups on the surface. We propose that this mechanism is the cause for the difference in redox peaks between the samples.

The amount of H_2O_2 used was also varied in order to investigate its effect on the electrode capacitance. Interestingly, the capacitance of the electrode increases greatly when 2 mL of H_2O_2 is used compared to 0.5 and 1 mL. Presumably this is caused by an increase in the generation of GQDs by raising the amount of H_2O_2 added during synthesis. This is corroborated by the colour of the as-synthesized GQD suspension. The suspension made with 2 mL H_2O_2 is completely transparent, while the 0.5 and 1 mL suspensions appear more brown, indicating the presence of a greater amount of uncut GO sheets (inset of **Figure 6-3 b)**).

From these two experiments, it was determined that the best performing GQDs samples were made with 2 mL H_2O_2 and the optimal deposition time was 1800s at 10 VDC. The capacitance of this sample was compared to that of neat carbon cloth in order to determine the capacitance contributions of each component in the composite electrode. **Figure 6-3 c)** shows the CV curves

of neat CC, HNO_3-treated CC and the best performing GQDs/CC composite electrode scanned at 50 mV s^{-1}. A slight improvement in capacitance is observed when the carbon cloth is treated with nitric acid due to the improved electrolyte wettability. The capacitance of the GQDs/CC composite is dramatically higher than that of both the neat CC and HNO_3-treated CC. This graph shows that the capacitance increase can be directly attributed to the deposition of the GQDs on the surface of the CC since the capacitance contribution of the neat CC, even after HNO_3 treatment, is negligible. The HNO_3 treatment improved the wettability of the CC which made it easier to deposit the GQDs on the surface. All samples discussed after this point were fabricated using HNO_3-treated CC but will have it omitted from the nomenclature for simplicity.

Figure 6-3 d) shows the CV curves of the GQDs/CC composite sample at a scan rate of 10 mV s^{-1} to 5 V s^{-1}. The GQDs/CC electrodes exhibit redox peaks during both forward and reverse scans which indicate the occurence of reversible redox reactions. These redox peaks are only prominent at low scan rates due to the slow nature of the Faradaic redox reactions compared to the adsorption and desorption of ions on the double layer surface. This results in the disappearance of the redox peaks as the scan rate is increased. At higher scan rates, the capacitance of the electrode material is dominated by super-capacitive behaviour in which the shape of the CV curves tend to be more rectangular in shape. The capacitance of the half-cell can be calculated by the following formula:

$$C_e = \frac{\int I\, dV}{2A\Delta V r} \tag{6-1}$$

where C_e is the areal capacitance of the electrode (mF cm^{-2}), $\int I\, dV$ is the area under the CV curve, A is the surface area of the electrode (cm^2), ΔV is the potential window (V) and r is the

scan rate used (mV s^{-1}). Based on this formula, the electrode has a capacitance of 70.7 mF cm^{-2} at a scan rate of 50 mV s^{-1}. This value is comparable with those reported previously featuring flexible supercapacitor electrodes with or without carbonaceous nanomaterials as shown in **Table 6-1**. The outlier in **Table 6-1** is the work presented by Yang et al [213] who achieved an areal capacitance of 6 F cm^{-2}. This high areal capacitance stems from the high loading (approximately 24 mg cm^{-2}) of CNT/rGO that they were able to achieve. Comparatively, the mass loading of GQDs shown in this work is negligible as shown by the SEM images shown in **Figure 6-2 (e)**. The negligible mass loading is due to the difficulty of depositing high amounts of GQDs via electrophoretic deposition on the surface of the carbon cloth. It is worth noting that a relatively high areal capacitance can be achieved despite this low loading of GQDs, which highlights the superior electrochemical performance of GQDs as an active material. Furthermore, our electrode can retain its capacitive behaviour even at high scan rates of 5000 mV s^{-1}, indicating the excellent rate capability of the resulting GQDs/CC composite electrode.

Table 6-1 *Capacitance values of various flexible electrode materials in literature compared to this work*

Materials	Capacitance (mF cm^2)	Reference
CC + GQDs	70.7	This work
Ag NW + PET	0.6	[214]
Cotton + MWCNT/RGO	6000	[213]
GQDs on interdigitated Au electrodes	0.53	[92]

GQDs/SWNT paper	55	[215]
CNT/GQDs	44	[216]
Graphene/GQDs chelate	0.007	[186]

Full-cell supercapacitors were made using the as-prepared composite electrodes as the positive and negative electrodes in a sandwich configuration containing a PVA/H_2SO_4 (10 wt% H_2SO_4) gel-electrolyte. A piece of filter paper that was soaked overnight in the gel electrolyte was used as a separator between the two electrodes. A schematic illustration of the full-cell configuration is provided in the inset of **Figure 6-4 a)**. **Figure 6-4 a)** shows the CV curve obtained at a scan rate of 10 mV s^{-1} of the supercapacitor made with the GQDs/CC composite electrodes. The square shape of the CV curve is indicative of super-capacitive behaviour. **Figure 6-4 b)** shows the CV curves of the same cell with different scan rates from 100 mV s^{-1} to 5000 mV s^{-1}. Similar to the half-cell, the supercapacitor made from the composite GQDs/CC electrodes exhibit the typical rectangular CV curves even at a high scan rate of 1000 mV s^{-1}. At 5000 mV s^{-1} the CV curve is slightly distorted but still presents a semi-rectangular curve due to the slow ion diffusion process. Typically, the highest scan rates shown in literature for supercapacitors with a sandwich configuration are in the range of 100 to 200 mV s^{-1} which makes the 5000 mV s^{-1} shown in our work remarkably high.

Figure 6-4 c) shows CVs of the supercapacitors during cycling, specifically the 1^{st}, 1000^{th} and 3000^{th} cycles. It can be seen that the supercapacitor is stable up to 1000 cycles but has degraded significantly by the 3000^{th} cycle. It was suspected that the PVA gel electrolyte was the culprit

of the decay and indeed it was the case. The PVA gel electrolyte on the same supercapacitors was re-hydrated and then a CV test was performed again at the same scan rate. **Figure 6-4 d)** shows the initial capacitance of the supercapacitor versus the re-hydrated supercapacitor after 3000 cycles. As the figure shows, the shape and size of the curve are similar, indicating that the electrolyte was the root cause of the decrease in capacitance, not the degradation of the electrodes themselves.

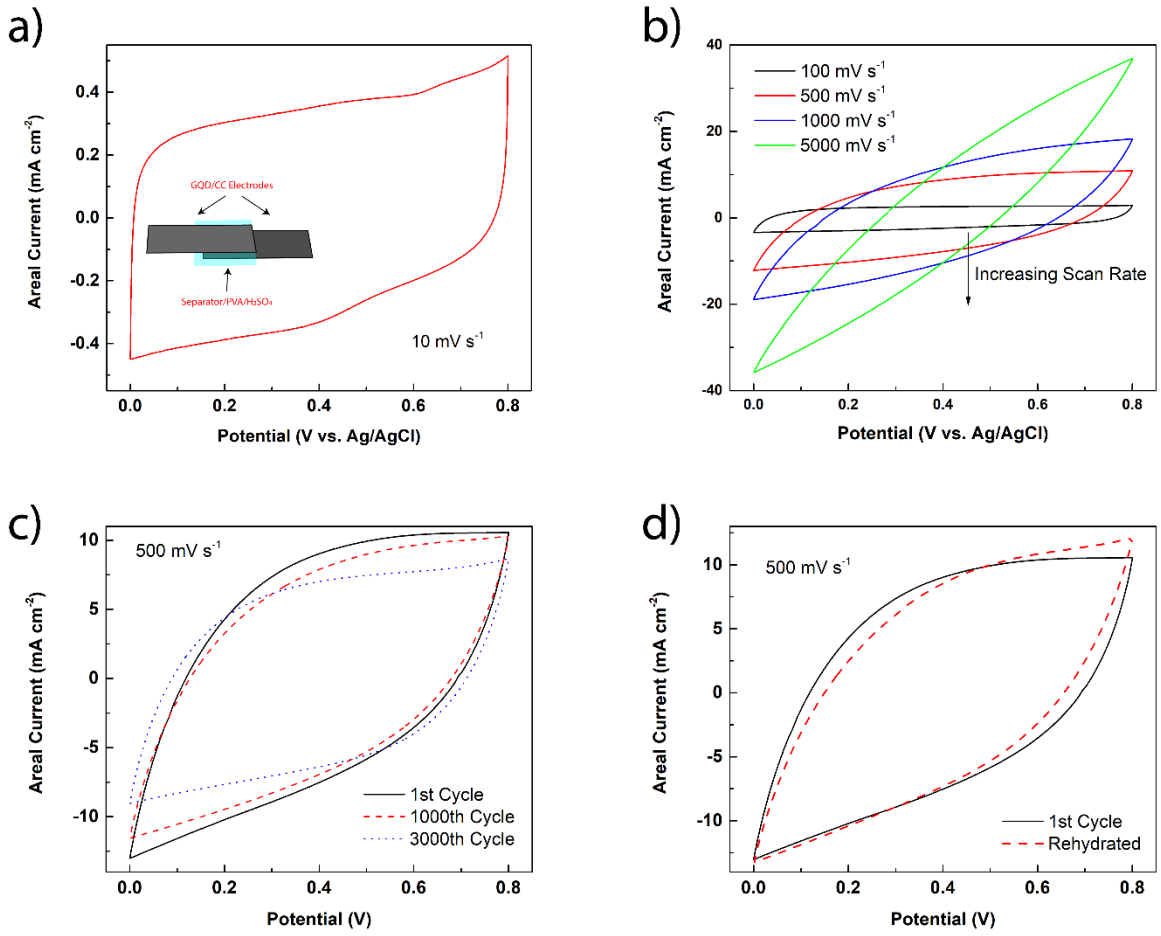

Figure 6-3 *Electrochemical characterization of the full-cell made with the GQDs/CC composite electrodes: a) CV of the full-cell at a scan rate of 10 mV s^{-1} with the inset showing a schematic illustration of the cell construction, b) CV of the full-cell collected at various scan rates from 100 – 5000 mV s^{-1}, c) CV of the full-cell after the 1st, 1000th and 3000th cycles collected at 500 mV s^{-1}, d) CV of the of the full-cell after the 1st and 3001th cycle (after the electrolyte was rehydrated) collected at 500 mV s^{-1}*

The capacitance of the supercapacitors can be calculated from the CVs using a similar expression to equation (6-1). However, more accurate values of the capacitance of the supercapacitors can be obtained using the charge and discharge curves shown in **Figure 6-5 a)** using the following equation:

$$C_s = \frac{I\Delta t}{A\Delta V} \qquad (6\text{-}2)$$

where C_s is the areal capacitance of the supercapacitor (mF cm^{-2}), I is the discharge/charge current used (mA cm^{-2}), Δt is the time it takes to charge/discharge the supercapacitor to a specified voltage (s), A is the overlapping surface area of the two electrodes (cm^2) and ΔV (V). is the potential window that was used in the test. **Figure 6-5 b)** shows areal capacitance of the supercapacitor at different discharge areal currents from 0.2 to 5 mA cm^{-2}. At 0.2 mA cm^{-2}, the supercapacitor exhibits a high areal capacitance of 77.5 mF cm^{-2} which is higher than other supercapacitors in literature with GQDs as a sole active material. The areal energy and power density of the supercapacitor can be calculated using the equations below:

$$E_{areal} = \frac{1}{2}\frac{C_s\ \Delta V^2}{A} \qquad (6\text{-}3)$$

$$P_{areal} = \frac{E_{areal}}{\Delta t} \qquad (6\text{-}4)$$

where E_{areal} is the areal energy density of the supercapacitor (mWh cm^{-2}), P_{areal} is the areal power density of the supercapacitor (mW cm^{-2}), C_s is the capacitance of the supercapacitor (mF cm^{-2}), V is the potential window (V) and A is the active surface area (cm^2). **Figure 6-5 c)** shows a Ragone plot that shows the dependence of the energy density on power density for the supercapacitor at different discharge currents. Due to its high capacitance, the supercapacitor also exhibits high areal energy and power densities of 24.8 mWh cm^{-2} and 288 mW cm^{-2} respectively at a discharge current of 0.2 mA cm^{-2}. EIS was conducted in order to further

understand the impedance and ion diffusion processes in the supercapacitor which may help explain the high performance of the device. **Figure 6-5 d)** shows the Nyquist plot of the GQDs/cc composite supercapacitor. The diameter of the semi-circle shown in the inset of **Figure 5 d)** represents the charge transfer resistance, R_{ct}, which relates the resistances present at the electrolyte/composite electrode and GQDs/CC interfaces. The full cell exhibits an R_{ct} of approximately 17 ohms, which is a relatively high value suggesting non-perfect contact between the GQDs and CC. This is corroborated by the fact that the CVs at higher scan rates deviate from the rectangular shapes shown at the lower scan rates. The equivalent series resistance (ESR), R_s, can also be found by taking the intercept of the curve on the Re(z) axis on the high frequency portion of the Nyquist plot. The ESR of the supercapacitor is approximately 13 ohms which explains the large drop in areal power and capacitance at higher discharge currents. The relatively high ESR may be due to the poor contact between the two electrodes in the supercapacitor resulting in a higher electronic resistance and the higher ionic resistance of the gel electrolyte.

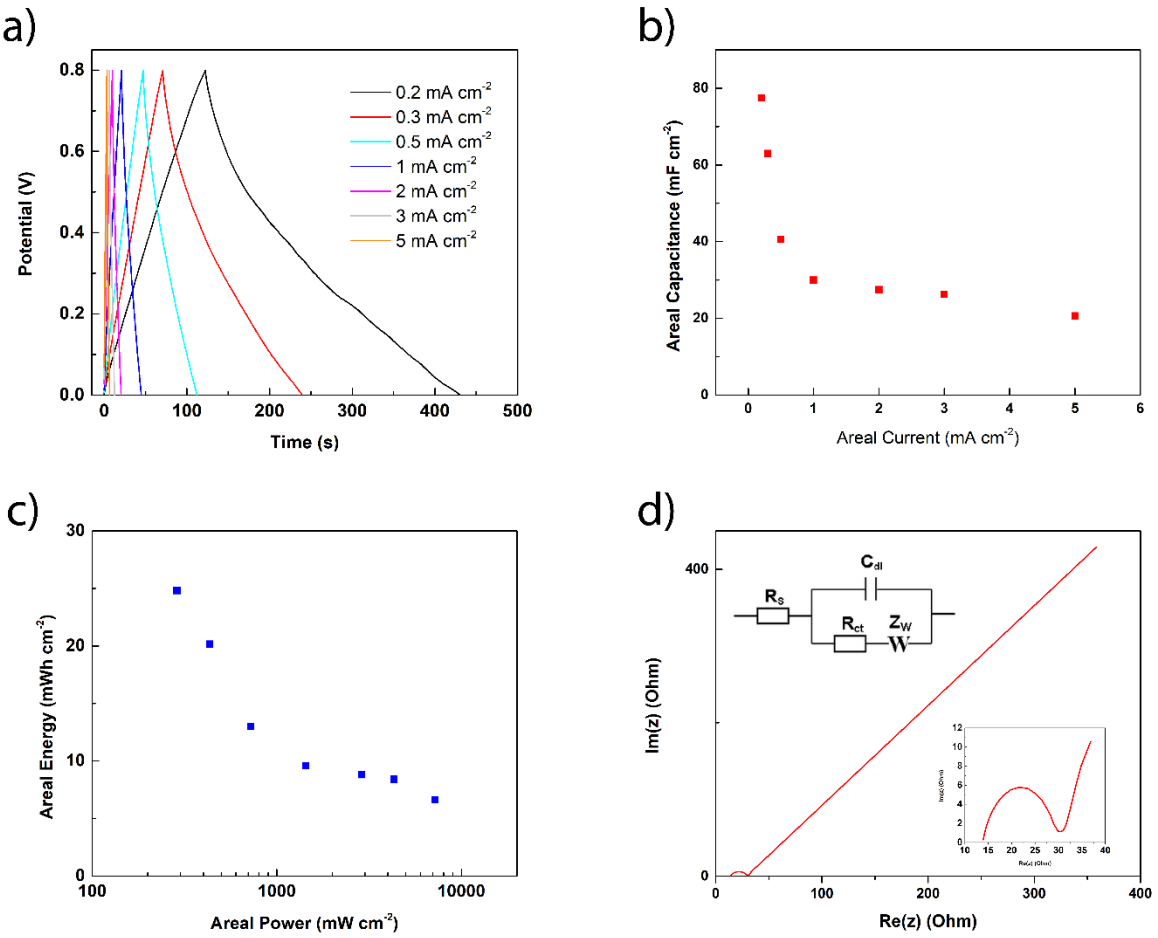

Figure 6-4 *a) galvanostatic charge discharge curves of the full-cell at various areal currents from 0.2 – 5 mA cm^{-2}, b) Areal capacitance of the full-cell versus the areal current used to discharge it, c) Ragone plot showing relationship between the areal power and areal energy of the full cell, and d) Nyquist plot of the full cell supercapacitor with the inset showing an expanded view of the high frequency region.*

Figure 6-5 a) shows a photograph of the full-cell under flexion with a radius of curvature, r_c, of 5 cm. **Figures 6-5 b) and c)** shows the CV curves of the cell under flexion. As shown in **Figure 6-5 b)**, the cell still retains its rectangular CV shape up to 1000 mV s^{-1}. While it also exhibits supercapacitive behaviour at 5000 mV s^{-1}, the shape of the CV curve is distorted more compared to the non-flexed state. This may be explained by the increase in resistance due to

the decrease in contact pressure between the two electrodes when the cell is flexed. **Figure 6-5 c)** shows the CV curves of the cell with and without flexion at a scan rate of 500 mV s^{-1}. It can be seen that the shapes of the CV curves are very similar, indicating that the cell is truly flexible. However, the flexed state does have a slightly smaller area compared to the unflexed state. This slight difference may have arisen due to the decreased contact between the electrodes due to the curvature induced under flexion.

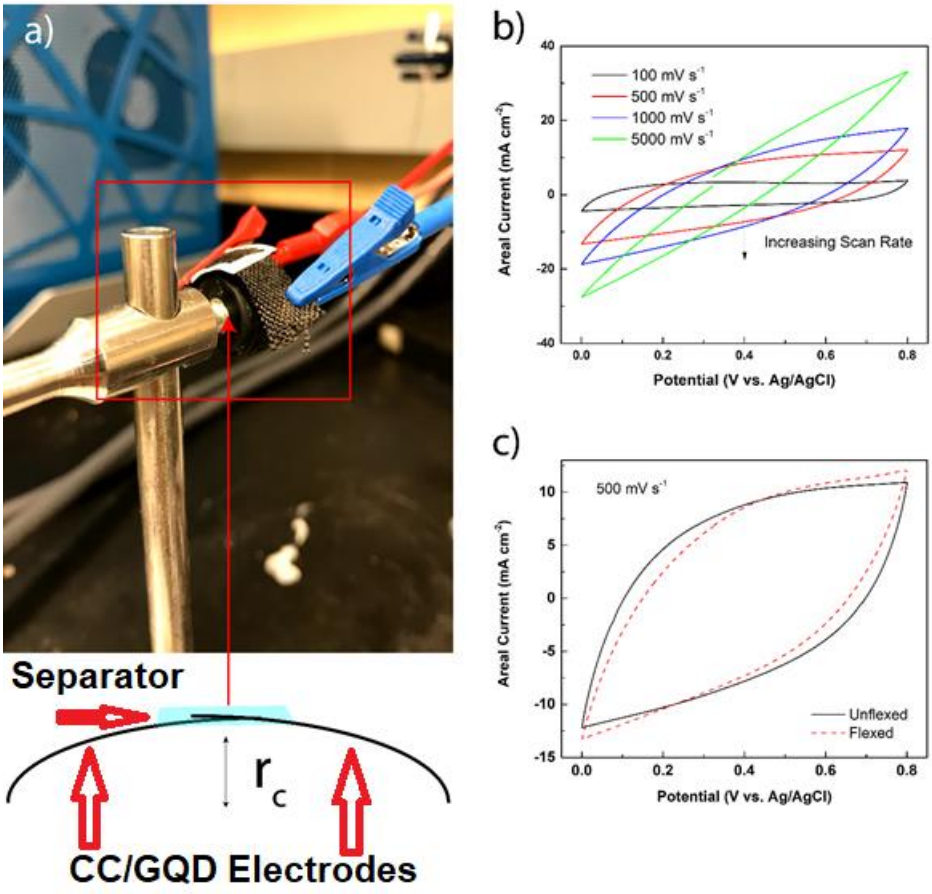

Figure 6-5 *a) Image showing the experimental setup to test the performance of the full cell under flexion at a specified radius of curvature, b) CV curves of the full-cell under flexion collected at different scan rates from 100 – 5000 mV s^{-1}, and c) Comparison of the CV curves of the full-cell with (red) and without flexion (black)*

6.4 Conclusions

We have successfully demonstrated the use of GQDs synthesized using a simple peroxide-assisted hydrothermal method in a high-performance flexible supercapacitor. Carbon cloth was used as a flexible, conductive substrate for the GQDs which acted as the active material. The composite electrode has a capacitance of 70.7 mF cm^{-2} at a scan rate of 50 mV s^{-1} while the full-cell supercapacitor made with the same composite materials exhibited a capacitance of 77.5 mF cm^{-2} at discharge current of 0.2 mA cm^{-2}. The composite electrode and supercapacitor are also able to retain a rectangular CV shape even at remarkably high scan rates of 5000 mV s^{-1} which is more than 10 times the typical scan rates previously reported. Furthermore, we have demonstrated that the supercapacitor retains its performance even when flexed, opening up the potential for it to be used in next-generation flexible electronic and wearable applications.

7.0 Conclusions & Future Work

In this thesis, various carbon materials have been explored for use as components of a flexible electrochemical energy storage electrode, from current collector to active material. Specifically, we have used these carbon materials in the pursuit of a flexible electrode for lithium-ion batteries, supercapacitors and a hybrid lithium-ion supercapacitor. We have synthesized and used various carbon materials, including carbon cloth, GO and its derivatives and amorphous carbon foams. This chapter outlines the conclusions from the previous chapters and discuss proposed future work based on the work shown in this thesis.

7.1 Conclusions

7.1.1 Flexible high performance lithium-ion battery electrode based on free-standing TiO_2 nanocrystals/carbon cloth composite

In this work, we have fabricated an oleic acid capped TiO_2 nanocrystal/carbon cloth composite flexible electrode for lithium-ion batteries. The anatase TiO_2 nanocrystals were synthesized using a one-step, 2-phase solvothermal method resulting in particle sizes of ~10 nm. The small particle size of the TiO_2 allows for better performance by decreasing the electron and lithium ion diffusion pathways. Additionally, oleic acid capping allows the particles to be dissolved in toluene and facilitates an even coverage over the carbon cloth surface. Half-cell studies were done in order the characterize the electrochemical performance of the composite electrode. It was found that the electrode exhibited a reversible capacity of 270 mAh g^{-1} at a current of 100 mA g^{-1} (close to the 330 mAh g^{-1} theoretical capacity of anatase TiO_2 for lithium insertion), outperforming commercial P25 electrode made with a conventional slurry casting method. This work establishes the viability of carbon cloth as a flexible electrode. At the time of writing, this

represents some of the best performances shown by flexible electrodes with TiO_2 as an active material.

7.1.2 Melamine based, N-doped carbon/reduced graphene oxide composite foam for lithium-ion hybrid Supercapacitors

A compression-tolerant, N-doped carbon/reduced graphene oxide composite foam was synthesized and used as a free-standing, binder-free negative electrode for lithium-ion capacitors. The foam was synthesized by direct carbonization and reduction of graphene oxide-coated melamine formaldehyde foam using a one-step heat treatment process. The nitrogen-rich carbonized melamine foam provides a robust conductive framework while the reduced graphene oxide provides most of the capacity for lithium insertion. A half-cell study was conducted using the as-prepared composite foam in order to determine its performance as a lithium-ion insertion host. The composite foam exhibits an excellent reversible capacity of 330 mAh g^{-1} at a current of 100 mA g^{-1} and good cycling stability. A lithium-ion hybrid capacitor was fabricated using the composite foam for both the positive and negative electrodes. The foam was used as-is as negative electrode and as a current collector for activated carbon on the positive side. The resulting lithium-ion hybrid capacitor achieved an energy density of 40 Wh kg^{-1} and energy density of 2000W kg^{-1} which matches the performance of non-flexible lithium-ion hybrid capacitors reported in the literature. We have also shown that the composite foam can also be used in other electrochemical energy storage systems, such as EDLC supercapacitors, further highlighting its versatility as an electrode material.

7.1.3 All-carbon flexible supercapacitors based on electrophoretic deposition of graphene quantum dots on carbon cloth

In this work, a flexible EDLC capacitor was made using a composite of carbon cloth and graphene quantum dots. The graphene quantum dots were synthesized using a simple peroxide-assisted hydrothermal method and deposited onto the flexible current collector via electrophoretic deposition, ensuring intimate contact. The composite electrode exhibits a half-cell capacitance of 70.7 mF cm^{-2} at a scan rate of 50 mV s^{-1} and a full-cell capacitance of 77.5 mF cm^{-2} when discharged with a current of 0.2 mA cm^{-2}. At the time of writing, this performance is amongst the highest in the literature for flexible electrodes with graphene quantum dots as the active material. The composite electrode and supercapacitor was also able to retain its rectangular shape at remarkably high scan rates of 5000 mV s^{-1} and 3000 charge discharge cycles, further showcasing the its high performance as an active material. We also showed that the supercapacitor made with the composite electrode is able to retain its performance under flexion, demonstrating its potential as a flexible energy storage device.

7.2 Recommendations and Future Work

7.2.1 Cell configuration and packaging

Chapter 5 has shown that the composite foam shows promise as an electroactive material and a current collector for flexible electrochemical energy storage devices. However, challenges still must be overcome. Optimal cell configuration and packaging must be determined in order to be able to take advantage of the foam electrode structure.

Both **Chapter 4 and 6** show flexible electrodes based on carbon cloth composites. We have demonstrated that flexible electrodes can attain performance levels that match those of conventional electrode fabrication techniques. However, work is still required to improve the performance of these devices and to ensure that the cloth-type electrodes are being used to their full potential. One of the attractive features of using cloth electrodes is the potential ability to directly integrate them with other textiles. However, this presents a challenge with the design described in **Chapter 4**, due to the need for vacuum sealing, and **Chapter 6**, due to the use of concentrated KOH. One possible solution is to change from organic and acidic/basic electrolytes to aqueous, neutral ones. However, this approach has obvious drawbacks such as the decreased voltage window. Another possible solution is to develop solid state electrolytes to replace the gel electrolytes that may still leak out and cause skin contact.

7.2.2 Hierarchical nanostructuring of carbonaceous materials

The foam presented in **Chapter 5** exhibits great promise as an electroactive material for lithium-ion capacitors due to the combination of macropores provided by the carbon foam and the surface area provided by the wrinkled rGO. It achieved an energy density of 40 Wh kg^{-1} which is comparable to that of other carbon-based lithium-ion capacitors but can certainly be improved. Additionally, its performance as an EDLC electrode is still lacking, only managing to achieve 20 F g^{-1}**.** Strategies to improve both the energy density and capacitance of the composite foam are to increase the inherent surface area and to improve the accessibility of ions this surface. This can be achieved by specifically tailoring the material to have specific pore distributions that facilitate ion diffusion and increase the available surface area. This strategy has led to a class or carbon materials called hierarchical porous carbons [183], [217]–[220].

These carbon materials contain interconnected multi-scale pores ranging from macropores to micropores. Althoughhe carbon foam shown in **Chapter 5** is macroporous due to its open cell structure, it does not likely contain the optimum amount and size of meso and micropores, which are necessary for ideal ion adsorption. Thus, future work should focus on the investigation of the exact pore distribution on the carbon foam. This information can then be used to tailor the specific pore size and distribution by using methods such as chemical activation or introducing of meso/microporous materials onto the surface of the composite carbon foam such as the GQDs we synthesized in **Chapter 6**.

7.2.3 Free-standing electrode for vanadium flow batteries

Chapter 5 shows that the foam can be successfully utilized as an active material for lithium-ion battery anodes, EDLC electrodes and as a conductive support for other active materials. One area of research that the foam electrode can be applied to is to all-vanadium flow batteries.. Vanadium flow batteries consists of two electrolytes separated by a proton exchange membrane as well as 2 carbon-based electrodes. Currently, these batteries use carbon materials such as carbon cloth and graphite felt as the electrodes due to their low-cost, chemical stability and electrochemical activity. Research has suggested that using carbonaceous nanomaterials as stand-alone electrodes or adding it to current electrode materials may increase the electroactivity of the electrodes due to the increased specific surface area, conductivity and ion/electron diffusivity [221]. Based on these criteria, the carbon foam described in this thesis may be a suitable candidate for this application due to its porosity (macropores from the open cell foam) and surface area (provided by the wrinkly rGO) and electronic conductivity.

7.2.4 GQDs scalable production and deposition methods

The work shown in **Chapter 6** is promising and shows that GQDs/carbon cloth composites are viable electrode materials for use in flexible EDLC supercapacitors. However, there approach has two deficiencies, namely:

1) non-scalable production of GQDs using the described synthesis procedure
2) low deposition mass of GQDs on the surface of carbon cloth

Although the top-down strategy shown in **Chapter 6** is relatively simple, it will be difficult to scale up due to the high-cost of operating large autoclave reactors [222]. Additionally, scaling up high-pressure and high-temperature processes tend to be expensive due to the additional safety and process controls required. At the time of writing, a few studies have been reported that offer alternative scalable methods of producing GQDs [222]–[224]. However, to our knowledge, none of this research involved GQDs for electrochemical energy storage applications which makes this topic suitable for future research.

The second deficiency is the low deposition mass of the GQDs on the carbon cloth. Although the performance of the electrode is still remarkable, further improvements can be made. We have shown in **Chapter 6** that the deposition time and hence mass loading can be optimized, to obtain the best performance. Further study needs to be conducted on why this optimal performance occurs at such a low loading and to develop strategies to mitigate the low performance at higher mass loadings.

8.0 References

[1] M. Agostini, B. Scrosati, and J. Hassoun, “An Advanced Lithium-Ion Sulfur Battery for High Energy Storage,” *Adv. Energy Mater.*, p. n/a-n/a, Jun. 2015.

[2] M. Amereller *et al.*, “Electrolytes for lithium and lithium ion batteries: From synthesis of novel lithium borates and ionic liquids to development of novel measurement methods,” *Prog. Solid State Chem.*, vol. 42, no. 4, pp. 39–56, Dec. 2014.

[3] J. Chatterjee, T. Liu, B. Wang, and J. P. Zheng, “Highly conductive PVA organogel electrolytes for applications of lithium batteries and electrochemical capacitors,” *Solid State Ion.*, vol. 181, no. 11–12, pp. 531–535, Apr. 2010.

[4] J. R. Dahn, T. Zheng, Y. Liu, and J. S. Xue, “Mechanisms for Lithium Insertion in Carbonaceous Materials,” *Science*, vol. 270, no. 5236, pp. 590–593, Oct. 1995.

[5] S. Flandrois and B. Simon, “Carbon materials for lithium-ion rechargeable batteries,” *Carbon*, vol. 37, no. 2, pp. 165–180, Feb. 1999.

[6] H. Gwon, J. Hong, H. Kim, D.-H. Seo, S. Jeon, and K. Kang, “Recent progress on flexible lithium rechargeable batteries,” *Energy Environ. Sci.*, vol. 7, no. 2, pp. 538–551, Jan. 2014.

[7] G. Zhu *et al.*, “Materials insights into low-temperature performances of lithium-ion batteries,” *J. Power Sources*, vol. 300, pp. 29–40, Dec. 2015.

[8] J. Zhang, Z. Shi, and C. Wang, “Effect of pre-lithiation degrees of mesocarbon microbeads anode on the electrochemical performance of lithium-ion capacitors,” *Electrochimica Acta*, vol. 125, pp. 22–28, Apr. 2014.

[9] Y. Sun *et al.*, “Coral-Inspired Nanoengineering Design for Long-Cycle and Flexible Lithium-Ion Battery Anode,” *ACS Appl. Mater. Interfaces*, vol. 8, no. 14, pp. 9185–9193, Apr. 2016.

[10] W. Liu, M.-S. Song, B. Kong, and Y. Cui, “Flexible and Stretchable Energy Storage: Recent Advances and Future Perspectives,” *Adv. Mater.*, vol. 29, no. 1, p. n/a-n/a, Jan. 2017.

[11] L. Hu, H. Wu, F. La Mantia, Y. Yang, and Y. Cui, “Thin, Flexible Secondary Li-Ion Paper Batteries,” *ACS Nano*, vol. 4, no. 10, pp. 5843–5848, Oct. 2010.

[12] L. Li, Z. Wu, S. Yuan, and X.-B. Zhang, “Advances and challenges for flexible energy storage and conversion devices and systems,” *Energy Environ. Sci.*, vol. 7, no. 7, pp. 2101–2122, Jun. 2014.

[13] G. Zhou, F. Li, and H.-M. Cheng, “Progress in flexible lithium batteries and future prospects,” *Energy Environ. Sci.*, vol. 7, no. 4, pp. 1307–1338, Mar. 2014.

[14] A. H. Castro Neto, F. Guinea, N. M. R. Peres, K. S. Novoselov, and A. K. Geim, “The electronic properties of graphene,” *Rev. Mod. Phys.*, vol. 81, no. 1, pp. 109–162, Jan. 2009.

[15] A. K. Geim, “Graphene: Status and Prospects,” *Science*, vol. 324, no. 5934, pp. 1530–1534, Jun. 2009.

[16] C. Wang, D. Li, C. O. Too, and G. G. Wallace, “Electrochemical Properties of Graphene Paper Electrodes Used in Lithium Batteries,” *Chem. Mater.*, vol. 21, no. 13, pp. 2604–2606, Jul. 2009.

[17] Z. Fan, J. Yan, G. Ning, T. Wei, L. Zhi, and F. Wei, “Porous graphene networks as high performance anode materials for lithium ion batteries,” *Carbon*, vol. 60, pp. 558–561, Aug. 2013.

[18] Y. Ma, H. Chang, M. Zhang, and Y. Chen, “Graphene-Based Materials for Lithium-Ion Hybrid Supercapacitors,” *Adv. Mater.*, vol. 27, no. 36, pp. 5296–5308, Sep. 2015.
[19] N. Li, Z. Chen, W. Ren, F. Li, and H.-M. Cheng, “Flexible graphene-based lithium ion batteries with ultrafast charge and discharge rates,” *Proc. Natl. Acad. Sci.*, vol. 109, no. 43, pp. 17360–17365, Oct. 2012.
[20] G. Wang, X. Shen, J. Yao, and J. Park, “Graphene nanosheets for enhanced lithium storage in lithium ion batteries,” *Carbon*, vol. 47, no. 8, pp. 2049–2053, Jul. 2009.
[21] E. Yoo, J. Kim, E. Hosono, H. Zhou, T. Kudo, and I. Honma, “Large Reversible Li Storage of Graphene Nanosheet Families for Use in Rechargeable Lithium Ion Batteries,” *Nano Lett.*, vol. 8, no. 8, pp. 2277–2282, Aug. 2008.
[22] Z. Zuo, T. Y. Kim, I. Kholmanov, H. Li, H. Chou, and Y. Li, “Ultra-light Hierarchical Graphene Electrode for Binder-Free Supercapacitors and Lithium-Ion Battery Anodes,” *Small*, vol. 11, no. 37, pp. 4922–4930, Oct. 2015.
[23] H.-P. Cong, S. Xin, and S.-H. Yu, “Flexible nitrogen-doped graphene/SnO2 foams promise kinetically stable lithium storage,” *Nano Energy*, vol. 13, pp. 482–490, Apr. 2015.
[24] A. Davies *et al.*, “Graphene-Based Flexible Supercapacitors: Pulse-Electropolymerization of Polypyrrole on Free-Standing Graphene Films,” *J. Phys. Chem. C*, vol. 115, no. 35, pp. 17612–17620, 2011.
[25] J. Kim, W.-H. Khoh, B.-H. Wee, and J.-D. Hong, “Fabrication of flexible reduced graphene oxide–TiO_2 freestanding films for supercapacitor application,” *RSC Adv.*, vol. 5, no. 13, pp. 9904–9911, Jan. 2015.
[26] M. Mao, J. Hu, and H. Liu, “Graphene-based materials for flexible electrochemical energy storage,” *Int. J. Energy Res.*, vol. 39, no. 6, pp. 727–740, May 2015.
[27] T. Huang *et al.*, “Flexible high performance wet-spun graphene fiber supercapacitors,” *RSC Adv.*, vol. 3, no. 46, pp. 23957–23962, 2013.
[28] W. Liu *et al.*, “Advanced Li-Ion Hybrid Supercapacitors Based on 3D Graphene–Foam Composites,” *ACS Appl. Mater. Interfaces*, vol. 8, no. 39, pp. 25941–25953, Oct. 2016.
[29] X. Zhao, B. Zheng, T. Huang, and C. Gao, “Graphene-based single fiber supercapacitor with a coaxial structure,” *Nanoscale*, vol. 7, no. 21, pp. 9399–9404, May 2015.
[30] X. Tang, F. Yan, Y. Wei, M. Zhang, T. Wang, and T. Zhang, “Encapsulating SnxSb Nanoparticles in Multichannel Graphene-Carbon Fibers As Flexible Anodes to Store Lithium Ions with High Capacities,” *ACS Appl. Mater. Interfaces*, vol. 7, no. 39, pp. 21890–21897, Oct. 2015.
[31] P. Zhang, R. Wang, M. He, J. Lang, S. Xu, and X. Yan, “3D Hierarchical Co/CoO-Graphene-Carbonized Melamine Foam as a Superior Cathode toward Long-Life Lithium Oxygen Batteries,” *Adv. Funct. Mater.*, vol. 26, no. 9, pp. 1354–1364, Mar. 2016.
[32] M. O. Adebajo, R. L. Frost, J. T. Kloprogge, O. Carmody, and S. Kokot, “Porous Materials for Oil Spill Cleanup: A Review of Synthesis and Absorbing Properties,” *J. Porous Mater.*, vol. 10, no. 3, pp. 159–170, Sep. 2003.
[33] S. R. Sivakkumar and A. G. Pandolfo, “Evaluation of lithium-ion capacitors assembled with pre-lithiated graphite anode and activated carbon cathode,” *Electrochimica Acta*, vol. 65, pp. 280–287, Mar. 2012.
[34] N. A. Kaskhedikar and J. Maier, “Lithium Storage in Carbon Nanostructures,” *Adv. Mater.*, vol. 21, no. 25–26, pp. 2664–2680, Jul. 2009.
[35] K. Persson *et al.*, “Lithium Diffusion in Graphitic Carbon,” *J. Phys. Chem. Lett.*, vol. 1, no. 8, pp. 1176–1180, Apr. 2010.

[36] V. Aravindan, J. Gnanaraj, Y.-S. Lee, and S. Madhavi, “Insertion-Type Electrodes for Nonaqueous Li-Ion Capacitors,” *Chem. Rev.*, vol. 114, no. 23, pp. 11619–11635, Dec. 2014.
[37] P. Simon and Y. Gogotsi, “Charge storage mechanism in nanoporous carbons and its consequence for electrical double layer capacitors,” *Philos. Trans. R. Soc. Lond. Math. Phys. Eng. Sci.*, vol. 368, no. 1923, pp. 3457–3467, Jul. 2010.
[38] B. Fang, A. Bonakdarpour, M.-S. Kim, J. H. Kim, D. P. Wilkinson, and J.-S. Yu, “Multimodal porous carbon as a highly efficient electrode material in an electric double layer capacitor,” *Microporous Mesoporous Mater.*, vol. 182, pp. 1–7, Dec. 2013.
[39] H. S. Choi and C. R. Park, “Theoretical guidelines to designing high performance energy storage device based on hybridization of lithium-ion battery and supercapacitor,” *J. Power Sources*, vol. 259, pp. 1–14, Aug. 2014.
[40] V. Augustyn, P. Simon, and B. Dunn, “Pseudocapacitive oxide materials for high-rate electrochemical energy storage,” *Energy Environ. Sci.*, vol. 7, no. 5, pp. 1597–1614, Apr. 2014.
[41] T. Aida, I. Murayama, K. Yamada, and M. Morita, “High-energy-density hybrid electrochemical capacitor using graphitizable carbon activated with KOH for positive electrode,” *J. Power Sources*, vol. 166, no. 2, pp. 462–470, Apr. 2007.
[42] D. Cericola and R. Kötz, “Hybridization of rechargeable batteries and electrochemical capacitors: Principles and limits,” *Electrochimica Acta*, vol. 72, pp. 1–17, Jun. 2012.
[43] J. Zhang, Z. Shi, J. Wang, and J. Shi, “Composite of mesocarbon microbeads/hard carbon as anode material for lithium ion capacitor with high electrochemical performance,” *J. Electroanal. Chem.*, vol. 747, pp. 20–28, Jun. 2015.
[44] Y. Cai, B. Zhao, J. Wang, and Z. Shao, “Non-aqueous hybrid supercapacitors fabricated with mesoporous TiO_2 microspheres and activated carbon electrodes with superior performance,” *J. Power Sources*, vol. 253, pp. 80–89, May 2014.
[45] R. Gokhale *et al.*, “Oligomer-salt derived 3D, heavily nitrogen doped, porous carbon for Li-ion hybrid electrochemical capacitors application,” *Carbon*, vol. 80, pp. 462–471, Dec. 2014.
[46] M. Kim *et al.*, “A fast and efficient pre-doping approach to high energy density lithium-ion hybrid capacitors,” *J. Mater. Chem. A*, vol. 2, no. 26, pp. 10029–10033, Jun. 2014.
[47] K. Naoi, “‘Nanohybrid Capacitor’: The Next Generation Electrochemical Capacitors,” *Fuel Cells*, vol. 10, no. 5, pp. 825–833, Oct. 2010.
[48] X. Yu *et al.*, “Ultrahigh-rate and high-density lithium-ion capacitors through hybriding nitrogen-enriched hierarchical porous carbon cathode with prelithiated microcrystalline graphite anode,” *Nano Energy*, vol. 15, pp. 43–53, Jul. 2015.
[49] X. Sun, X. Zhang, K. Wang, N. Xu, and Y. Ma, “Temperature effect on electrochemical performances of Li-ion hybrid capacitors,” *J. Solid State Electrochem.*, vol. 19, no. 8, pp. 2501–2506, May 2015.
[50] S. R. Sivakkumar, J. Y. Nerkar, and A. G. Pandolfo, “Rate capability of graphite materials as negative electrodes in lithium-ion capacitors,” *Electrochimica Acta*, vol. 55, no. 9, pp. 3330–3335, Mar. 2010.
[51] J. Zhang, X. Liu, J. Wang, J. Shi, and Z. Shi, “Different types of pre-lithiated hard carbon as negative electrode material for lithium-ion capacitors,” *Electrochimica Acta*, vol. 187, pp. 134–142, Jan. 2016.

[52] R. Tjandra, G. Lui, A. Veilleux, J. Broughton, G. Chiu, and A. Yu, "Introduction of an Enhanced Binding of Reduced Graphene Oxide to Polyurethane Sponge for Oil Absorption," *Ind. Eng. Chem. Res.*, Mar. 2015.
[53] Y. Gong, S. Yang, Z. Liu, L. Ma, R. Vajtai, and P. M. Ajayan, "Graphene-Network-Backboned Architectures for High-Performance Lithium Storage," *Adv. Mater.*, vol. 25, no. 29, pp. 3979–3984, Aug. 2013.
[54] A. L. M. Reddy, A. Srivastava, S. R. Gowda, H. Gullapalli, M. Dubey, and P. M. Ajayan, "Synthesis Of Nitrogen-Doped Graphene Films For Lithium Battery Application," *ACS Nano*, vol. 4, no. 11, pp. 6337–6342, Nov. 2010.
[55] D. Pan *et al.*, "Li Storage Properties of Disordered Graphene Nanosheets," *Chem. Mater.*, vol. 21, no. 14, pp. 3136–3142, Jul. 2009.
[56] J. Hou, Y. Shao, M. W. Ellis, R. B. Moore, and B. Yi, "Graphene-based electrochemical energy conversion and storage: fuel cells, supercapacitors and lithium ion batteries," *Phys. Chem. Chem. Phys.*, vol. 13, no. 34, pp. 15384–15402, Aug. 2011.
[57] H. J. Hwang, J. Koo, M. Park, N. Park, Y. Kwon, and H. Lee, "Multilayer Graphynes for Lithium Ion Battery Anode," *J. Phys. Chem. C*, vol. 117, no. 14, pp. 6919–6923, Apr. 2013.
[58] T. Zheng, J. N. Reimers, and J. R. Dahn, "Effect of turbostratic disorder in graphitic carbon hosts on the intercalation of lithium," *Phys. Rev. B*, vol. 51, no. 2, pp. 734–741, Jan. 1995.
[59] T. Zheng, Y. Liu, E. W. Fuller, S. Tseng, U. von Sacken, and J. R. Dahn, "Lithium Insertion in High Capacity Carbonaceous Materials," *J. Electrochem. Soc.*, vol. 142, no. 8, pp. 2581–2590, Aug. 1995.
[60] T. Zheng, W. Xing, and J. R. Dahn, "Carbons prepared from coals for anodes of lithium-ion cells," *Carbon*, vol. 34, no. 12, pp. 1501–1507, Jan. 1996.
[61] S. Lee, S. H. Eom, J. S. Chung, and S. H. Hur, "Large-scale production of high-quality reduced graphene oxide," *Chem. Eng. J.*, vol. 233, pp. 297–304, Nov. 2013.
[62] A. M. Dimiev and J. M. Tour, "Mechanism of Graphene Oxide Formation," *ACS Nano*, vol. 8, no. 3, pp. 3060–3068, Mar. 2014.
[63] H.-P. Cong, X.-C. Ren, P. Wang, and S.-H. Yu, "Wet-spinning assembly of continuous, neat, and macroscopic graphene fibers," *Sci. Rep.*, vol. 2, p. 613, Aug. 2012.
[64] R. Jalili *et al.*, "Scalable One-Step Wet-Spinning of Graphene Fibers and Yarns from Liquid Crystalline Dispersions of Graphene Oxide: Towards Multifunctional Textiles," *Adv. Funct. Mater.*, vol. 23, no. 43, pp. 5345–5354, Nov. 2013.
[65] Y. He *et al.*, "Alginate/graphene oxide fibers with enhanced mechanical strength prepared by wet spinning," *Carbohydr. Polym.*, vol. 88, no. 3, pp. 1100–1108, Apr. 2012.
[66] Z. Dong *et al.*, "Facile Fabrication of Light, Flexible and Multifunctional Graphene Fibers," *Adv. Mater.*, vol. 24, no. 14, pp. 1856–1861, Apr. 2012.
[67] Z. Xu, H. Sun, X. Zhao, and C. Gao, "Ultrastrong Fibers Assembled from Giant Graphene Oxide Sheets," *Adv. Mater.*, vol. 25, no. 2, pp. 188–193, Jan. 2013.
[68] M. He, L. Kang, C. Liu, Z. Lei, and Z.-H. Liu, "Layer-by-layer assembly of manganese–cobalt–nickel oxide nanosheets/graphene composite films," *Mater. Res. Bull.*, vol. 68, pp. 194–202, Aug. 2015.
[69] L. Jiang, X. Lu, C. Xie, G. Wan, H. Zhang, and T. Youhong, "Flexible, Free-Standing TiO_2–Graphene–Polypyrrole Composite Films as Electrodes for Supercapacitors," *J. Phys. Chem. C*, vol. 119, no. 8, pp. 3903–3910, Feb. 2015.

[70] A. Yu, I. Roes, A. Davies, and Z. Chen, “Ultrathin, transparent, and flexible graphene films for supercapacitor application,” *Appl. Phys. Lett.*, vol. 96, no. 25, p. 253105, Jun. 2010.
[71] J. Luo *et al.*, “Three-Dimensional Graphene Foam Supported Fe3O4 Lithium Battery Anodes with Long Cycle Life and High Rate Capability,” *Nano Lett.*, vol. 13, no. 12, pp. 6136–6143, Dec. 2013.
[72] H. Wang, X. Li, M. Baker-Fales, and P. B. Amama, “3D graphene-based anode materials for Li-ion batteries,” *Curr. Opin. Chem. Eng.*, vol. 13, pp. 124–132, Aug. 2016.
[73] X. Tian, Y. Zhou, X. Tu, Z. Zhang, and G. Du, “Well-dispersed LiFePO4 nanoparticles anchored on a three-dimensional graphene aerogel as high-performance positive electrode materials for lithium-ion batteries,” *J. Power Sources*, vol. 340, pp. 40–50, Feb. 2017.
[74] X. Zhang *et al.*, “Mechanically strong and highly conductive graphene aerogel and its use as electrodes for electrochemical power sources,” *J. Mater. Chem.*, vol. 21, no. 18, pp. 6494–6497, Apr. 2011.
[75] K. Xi *et al.*, “Binder free three-dimensional sulphur/few-layer graphene foam cathode with enhanced high-rate capability for rechargeable lithium sulphur batteries,” *Nanoscale*, vol. 6, no. 11, pp. 5746–5753, May 2014.
[76] G. Zhou *et al.*, “A graphene foam electrode with high sulfur loading for flexible and high energy Li-S batteries,” *Nano Energy*, vol. 11, pp. 356–365, Jan. 2015.
[77] X. Dong *et al.*, “Synthesis of a MnO2–graphene foam hybrid with controlled MnO2 particle shape and its use as a supercapacitor electrode,” *Carbon*, vol. 50, no. 13, pp. 4865–4870, Nov. 2012.
[78] X. Dong *et al.*, “3D Graphene Foam as a Monolithic and Macroporous Carbon Electrode for Electrochemical Sensing,” *ACS Appl. Mater. Interfaces*, vol. 4, no. 6, pp. 3129–3133, Jun. 2012.
[79] Y. Zhao *et al.*, “Highly Compression-Tolerant Supercapacitor Based on Polypyrrole-mediated Graphene Foam Electrodes,” *Adv. Mater.*, vol. 25, no. 4, pp. 591–595, Jan. 2013.
[80] Z. Hou *et al.*, “Hierarchically porous nitrogen-doped graphene aerogels as efficient metal-free oxygen reduction catalysts,” *J. Colloid Interface Sci.*, vol. 488, pp. 317–321, Feb. 2017.
[81] S. Bak, D. Kim, and H. Lee, “Graphene quantum dots and their possible energy applications: A review,” *Curr. Appl. Phys.*, vol. 16, no. 9, pp. 1192–1201, Sep. 2016.
[82] W. Chen, G. Lv, W. Hu, D. Li, S. Chen, and Z. Dai, “Synthesis and applications of graphene quantum dots: a review,” *Nanotechnol. Rev.*, vol. 7, no. 2, pp. 157–185, 2018.
[83] M. Bacon, S. J. Bradley, and T. Nann, “Graphene Quantum Dots,” *Part. Part. Syst. Charact.*, vol. 31, no. 4, pp. 415–428, Apr. 2014.
[84] X. Li, M. Rui, J. Song, Z. Shen, and H. Zeng, “Carbon and Graphene Quantum Dots for Optoelectronic and Energy Devices: A Review,” *Adv. Funct. Mater.*, vol. 25, no. 31, pp. 4929–4947, Aug. 2015.
[85] D. Pan, J. Zhang, Z. Li, and M. Wu, “Hydrothermal Route for Cutting Graphene Sheets into Blue-Luminescent Graphene Quantum Dots,” *Adv. Mater.*, vol. 22, no. 6, pp. 734–738, Feb. 2010.
[86] M. Alam Sk, A. Ananthanarayanan, L. Huang, K. Hwa Lim, and P. Chen, “Revealing the tunable photoluminescence properties of graphene quantum dots,” *J. Mater. Chem. C*, vol. 2, no. 34, pp. 6954–6960, 2014.

[87] J.-M. Yuan, R. Zhao, Z.-J. Wu, W. Li, and X.-G. Yang, “Graphene Oxide Quantum Dots Exfoliated From Carbon Fibers by Microwave Irradiation: Two Photoluminescence Centers and Self-Assembly Behavior,” *Small*, vol. 14, no. 20, p. 1703714.
[88] Y. Hu, J. Yang, L. Jia, and J.-S. Yu, “Ethanol in aqueous hydrogen peroxide solution: Hydrothermal synthesis of highly photoluminescent carbon dots as multifunctional nanosensors,” *Carbon*, vol. 93, pp. 999–1007, Nov. 2015.
[89] H. Li *et al.*, “Fluorescent carbon nanoparticles : electrochemical synthesis and their pH sensitive photoluminescence properties,” *New J. Chem.*, vol. 35, no. 11, pp. 2666–2670, 2011.
[90] R. Tian, S. Zhong, J. Wu, W. Jiang, and T. Wang, “Facile hydrothermal method to prepare graphene quantum dots from graphene oxide with different photoluminescences,” *RSC Adv.*, vol. 6, no. 46, pp. 40422–40426, 2016.
[91] X. Zhu, X. Xiao, X. Zuo, Y. Liang, and J. Nan, “Hydrothermal Preparation of Photoluminescent Graphene Quantum Dots Characterized Excitation-Independent Emission and its Application as a Bioimaging Reagent,” *Part. Part. Syst. Charact.*, vol. 31, no. 7, pp. 801–809, Jul. 2014.
[92] W.-W. Liu, Y.-Q. Feng, X.-B. Yan, J.-T. Chen, and Q.-J. Xue, “Superior Micro-Supercapacitors Based on Graphene Quantum Dots,” *Adv. Funct. Mater.*, vol. 23, no. 33, pp. 4111–4122, Sep. 2013.
[93] W. Liu *et al.*, “Paper-based all-solid-state flexible micro-supercapacitors with ultra-high rate and rapid frequency response capabilities,” *J. Mater. Chem. A*, vol. 4, no. 10, pp. 3754–3764, Mar. 2016.
[94] Z. Li *et al.*, “Nitrogen and oxygen co-doped graphene quantum dots with high capacitance performance for micro-supercapacitors,” *Carbon*, vol. 139, pp. 67–75, Nov. 2018.
[95] S. Mondal, U. Rana, and S. Malik, “Graphene quantum dot-doped polyaniline nanofiber as high performance supercapacitor electrode materials,” *Chem. Commun.*, vol. 51, no. 62, pp. 12365–12368, 2015.
[96] L. Ruiyi *et al.*, “Significantly enhanced electrochemical performance of lithium titanate anode for lithium ion battery by the hybrid of nitrogen and sulfur co-doped graphene quantum dots,” *Electrochimica Acta*, vol. 178, pp. 303–311, Oct. 2015.
[97] “Highly Conductive Ordered Mesoporous Carbon Based Electrodes Decorated by 3D Graphene and 1D Silver Nanowire for Flexible Supercapacitor - Zhi - 2014 - Advanced Functional Materials - Wiley Online Library.” [Online]. Available: https://onlinelibrary.wiley.com/doi/full/10.1002/adfm.201303082. [Accessed: 23-May-2019].
[98] Z. Niu *et al.*, “Electrophoretic Build-Up of Alternately Multilayered Films and Micropatterns Based on Graphene Sheets and Nanoparticles and their Applications in Flexible Supercapacitors,” *Small*, vol. 8, no. 20, pp. 3201–3208, 2012.
[99] X. Yang, J. Zhu, L. Qiu, and D. Li, “Bioinspired Effective Prevention of Restacking in Multilayered Graphene Films: Towards the Next Generation of High-Performance Supercapacitors,” *Adv. Mater.*, vol. 23, no. 25, pp. 2833–2838, 2011.
[100] G. Wang *et al.*, “Flexible Pillared Graphene-Paper Electrodes for High-Performance Electrochemical Supercapacitors,” *Small*, vol. 8, no. 3, pp. 452–459, 2012.
[101] M. F. El-Kady and R. B. Kaner, “Scalable fabrication of high-power graphene micro-supercapacitors for flexible and on-chip energy storage,” *Nat. Commun.*, vol. 4, p. 1475, Feb. 2013.

[102] P. Huang *et al.*, "On-chip and freestanding elastic carbon films for micro-supercapacitors," *Science*, vol. 351, no. 6274, pp. 691–695, Feb. 2016.
[103] C. Meng, J. Maeng, S. W. M. John, and P. P. Irazoqui, "Ultrasmall Integrated 3D Micro-Supercapacitors Solve Energy Storage for Miniature Devices," *Adv. Energy Mater.*, vol. 4, no. 7, p. 1301269, 2014.
[104] Z.-S. Wu, S. Yang, L. Zhang, J. B. Wagner, X. Feng, and K. Müllen, "Binder-free activated graphene compact films for all-solid-state micro-supercapacitors with high areal and volumetric capacitances," *Energy Storage Mater.*, vol. 1, pp. 119–126, Nov. 2015.
[105] L. Hu and Y. Cui, "Energy and environmental nanotechnology in conductive paper and textiles," *Energy Environ. Sci.*, vol. 5, no. 4, pp. 6423–6435, Mar. 2012.
[106] X. Pu *et al.*, "A Self-Charging Power Unit by Integration of a Textile Triboelectric Nanogenerator and a Flexible Lithium-Ion Battery for Wearable Electronics," *Adv. Mater.*, vol. 27, no. 15, pp. 2472–2478, Apr. 2015.
[107] L. Hu *et al.*, "Stretchable, Porous, and Conductive Energy Textiles," *Nano Lett.*, vol. 10, no. 2, pp. 708–714, Feb. 2010.
[108] L. Liu, Z. Niu, L. Zhang, W. Zhou, X. Chen, and S. Xie, "Nanostructured Graphene Composite Papers for Highly Flexible and Foldable Supercapacitors," *Adv. Mater.*, vol. 26, no. 28, pp. 4855–4862, 2014.
[109] M.-S. Balogun *et al.*, "Titanium dioxide@titanium nitride nanowires on carbon cloth with remarkable rate capability for flexible lithium-ion batteries," *J. Power Sources*, vol. 272, pp. 946–953, Dec. 2014.
[110] A. Janicek, N. Gao, Y. Fan, and H. Liu, "High Performance Activated Carbon/Carbon Cloth Cathodes for Microbial Fuel Cells," *Fuel Cells*, p. n/a-n/a, Oct. 2015.
[111] R. Tjandra, "Binder-free TiO_2/Carbon Cloth Composite Anode for Electrochemical Energy Storage Devices," Sep. 2015.
[112] H. Zhang, W. Ren, and C. Cheng, "Three-dimensional SnO2@TiO_2 double-shell nanotubes on carbon cloth as a flexible anode for lithium-ion batteries," *Nanotechnology*, vol. 26, no. 27, p. 274002, Jul. 2015.
[113] Z. Chen *et al.*, "3D Nanocomposite Architectures from Carbon-Nanotube-Threaded Nanocrystals for High-Performance Electrochemical Energy Storage," *Adv. Mater.*, vol. 26, no. 2, pp. 339–345, Jan. 2014.
[114] Z. Chen *et al.*, "High-Performance Energy-Storage Architectures from Carbon Nanotubes and Nanocrystal Building Blocks," *Adv. Mater.*, vol. 24, no. 15, pp. 2030–2036, Apr. 2012.
[115] Z. Wang *et al.*, "Activated carbon fiber paper with exceptional capacitive performance as a robust electrode for supercapacitors," *J. Mater. Chem. A*, vol. 4, no. 16, pp. 5828–5833, Apr. 2016.
[116] D. Yu *et al.*, "Transforming Pristine Carbon Fiber Tows into High Performance Solid-State Fiber Supercapacitors," *Adv. Mater.*, vol. 27, no. 33, pp. 4895–4901, 2015.
[117] T. Qin *et al.*, "Flexible and Wearable All-Solid-State Supercapacitors with Ultrahigh Energy Density Based on a Carbon Fiber Fabric Electrode," *Adv. Energy Mater.*, vol. 7, no. 20, p. 1700409, 2017.
[118] P. Suktha *et al.*, "High-Performance Supercapacitor of Functionalized Carbon Fiber Paper with High Surface Ionic and Bulk Electronic Conductivity: Effect of Organic Functional Groups," *Electrochimica Acta*, vol. 176, pp. 504–513, Sep. 2015.

[119] Y. H. Kwon *et al.*, "Cable-Type Flexible Lithium Ion Battery Based on Hollow Multi-Helix Electrodes," *Adv. Mater.*, vol. 24, no. 38, pp. 5192–5197, Oct. 2012.
[120] A. Yadav, B. De, S. K. Singh, P. Sinha, and K. K. Kar, "Facile Development Strategy of a Single Carbon-Fiber-Based All-Solid-State Flexible Lithium-Ion Battery for Wearable Electronics," *ACS Appl. Mater. Interfaces*, vol. 11, no. 8, pp. 7974–7980, Feb. 2019.
[121] G. Zhu, C. Xi, Y. Liu, J. Zhu, and X. Shen, "CN foam loaded with few-layer graphene nanosheets for high-performance supercapacitor electrodes," *J. Mater. Chem. A*, vol. 3, no. 14, pp. 7591–7599, Mar. 2015.
[122] A. P. Cohn *et al.*, "Assessing the improved performance of freestanding, flexible graphene and carbon nanotube hybrid foams for lithium ion battery anodes," *Nanoscale*, vol. 6, no. 9, pp. 4669–4675, Apr. 2014.
[123] Y.-S. Jun *et al.*, "Highly conductive interconnected graphene foam based polymer composite," *Carbon*, vol. 95, pp. 653–658, Dec. 2015.
[124] R. Wang, C. Xu, J. Sun, L. Gao, and C. Lin, "Flexible free-standing hollow Fe3O4/graphene hybrid films for lithium-ion batteries," *J. Mater. Chem. A*, vol. 1, no. 5, pp. 1794–1800, Jan. 2013.
[125] Z. Zhang, F. Xiao, Y. Guo, S. Wang, and Y. Liu, "One-Pot Self-Assembled Three-Dimensional TiO_2-Graphene Hydrogel with Improved Adsorption Capacities and Photocatalytic and Electrochemical Activities," *ACS Appl. Mater. Interfaces*, vol. 5, no. 6, pp. 2227–2233, Mar. 2013.
[126] B. Qiu, M. Xing, and J. Zhang, "Mesoporous TiO_2 Nanocrystals Grown in Situ on Graphene Aerogels for High Photocatalysis and Lithium-Ion Batteries," *J. Am. Chem. Soc.*, vol. 136, no. 16, pp. 5852–5855, Apr. 2014.
[127] J. Chen, J. Xu, S. Zhou, N. Zhao, and C.-P. Wong, "Nitrogen-doped hierarchically porous carbon foam: A free-standing electrode and mechanical support for high-performance supercapacitors," *Nano Energy*, vol. 25, pp. 193–202, Jul. 2016.
[128] S. Chen *et al.*, "Elastic carbon foam via direct carbonization of polymer foam for flexible electrodes and organic chemical absorption," *Energy Environ. Sci.*, vol. 6, no. 8, pp. 2435–2439, Jul. 2013.
[129] Z. Fan, D. Qi, Y. Xiao, J. Yan, and T. Wei, "One-step synthesis of biomass-derived porous carbon foam for high performance supercapacitors," *Mater. Lett.*, vol. 101, pp. 29–32, Jun. 2013.
[130] M. Inagaki, J. Qiu, and Q. Guo, "Carbon foam: Preparation and application," *Carbon*, vol. 87, pp. 128–152, Jun. 2015.
[131] M. Kodama, J. Yamashita, Y. Soneda, H. Hatori, and K. Kamegawa, "Preparation and electrochemical characteristics of N-enriched carbon foam," *Carbon*, vol. 45, no. 5, pp. 1105–1107, Apr. 2007.
[132] A. K. Roy, M. Zhong, M. G. Schwab, A. Binder, S. S. Venkataraman, and Ž. Tomović, "Preparation of a Binder-Free Three-Dimensional Carbon Foam/Silicon Composite as Potential Material for Lithium Ion Battery Anodes," *ACS Appl. Mater. Interfaces*, vol. 8, no. 11, pp. 7343–7348, Mar. 2016.
[133] H. Zhang *et al.*, "Porous nitrogen doped carbon foam with excellent resilience for self-supported oxygen reduction catalyst," *Carbon*, vol. 95, pp. 388–395, Dec. 2015.

[134] X. Zhong, Z. Yang, Y. Jiang, W. Li, L. Gu, and Y. Yu, “Carbon-Coated Na3V2(PO4)3 Anchored on Freestanding Graphite Foam for High-Performance Sodium-Ion Cathodes,” *ACS Appl. Mater. Interfaces*, vol. 8, no. 47, pp. 32360–32365, Nov. 2016.
[135] T. N. Pham *et al.*, “Industrially benign super-compressible piezoresistive carbon foams with predefined wetting properties: from environmental to electrical applications,” *Sci. Rep.*, vol. 4, p. 6933, Nov. 2014.
[136] L. Shen, J. Wang, G. Xu, H. Li, H. Dou, and X. Zhang, “NiCo2S4 Nanosheets Grown on Nitrogen-Doped Carbon Foams as an Advanced Electrode for Supercapacitors,” *Adv. Energy Mater.*, vol. 5, no. 3, p. n/a-n/a, Feb. 2015.
[137] Y. Wang *et al.*, “Lithium and lithium ion batteries for applications in microelectronic devices: A review,” *J. Power Sources*, vol. 286, pp. 330–345, Jul. 2015.
[138] A. M. Gaikwad, G. L. Whiting, D. A. Steingart, and A. C. Arias, “Highly Flexible, Printed Alkaline Batteries Based on Mesh-Embedded Electrodes,” *Adv. Mater.*, vol. 23, no. 29, pp. 3251–3255, Aug. 2011.
[139] X. Wang, X. Lu, B. Liu, D. Chen, Y. Tong, and G. Shen, “Flexible Energy-Storage Devices: Design Consideration and Recent Progress,” *Adv. Mater.*, vol. 26, no. 28, pp. 4763–4782, Jul. 2014.
[140] Q. Zheng, Z. Cai, Z. Ma, and S. Gong, “Cellulose Nanofibril/Reduced Graphene Oxide/Carbon Nanotube Hybrid Aerogels for Highly Flexible and All-Solid-State Supercapacitors,” *ACS Appl. Mater. Interfaces*, vol. 7, no. 5, pp. 3263–3271, Feb. 2015.
[141] B. Liu *et al.*, “Hierarchical Three-Dimensional ZnCo2O4 Nanowire Arrays/Carbon Cloth Anodes for a Novel Class of High-Performance Flexible Lithium-Ion Batteries,” *Nano Lett.*, vol. 12, no. 6, pp. 3005–3011, Jun. 2012.
[142] Y. Tang, Y. Zhang, W. Li, B. Ma, and X. Chen, “Rational material design for ultrafast rechargeable lithium-ion batteries,” *Chem. Soc. Rev.*, vol. 44, no. 17, pp. 5926–5940, Aug. 2015.
[143] G. Lui, J.-Y. Liao, A. Duan, Z. Zhang, M. Fowler, and A. Yu, “Graphene-wrapped hierarchical TiO_2 nanoflower composites with enhanced photocatalytic performance,” *J. Mater. Chem. A*, vol. 1, no. 39, pp. 12255–12262, Sep. 2013.
[144] H. Zhang, X. Lv, Y. Li, Y. Wang, and J. Li, “P25-Graphene Composite as a High Performance Photocatalyst,” *ACS Nano*, vol. 4, no. 1, pp. 380–386, Jan. 2010.
[145] M. Moradzaman, M. R. Mohammadi, and H. Nourizadeh, “Efficient dye-sensitized solar cells based on CNTs and Zr-doped TiO_2 nanoparticles,” *Mater. Sci. Semicond. Process.*, vol. 40, pp. 383–390, Dec. 2015.
[146] A. M. Bakhshayesh and N. Bakhshayesh, “Enhanced performance of dye-sensitized solar cells aided by Sr,Cr co-doped TiO2 xerogel films made of uniform spheres,” *J. Colloid Interface Sci.*, vol. 460, pp. 18–28, Dec. 2015.
[147] X. Yan *et al.*, “TiO_2 Nanomaterials as Anode Materials for Lithium-Ion Rechargeable Batteries,” *Energy Technol.*, vol. 3, no. 8, pp. 801–814, Aug. 2015.
[148] J. Wei, J.-X. Liu, Z.-Y. Wu, Z.-L. Zhan, J. Shi, and K. Xu, “Research on the Electrochemical Performance of Rutile and Anatase Composite TiO_2 Nanotube Arrays in Lithium-Ion Batteries,” *J. Nanosci. Nanotechnol.*, vol. 15, no. 7, pp. 5013–5019, Jul. 2015.
[149] M. V. Koudriachova, N. M. Harrison, and S. W. de Leeuw, “Effect of Diffusion on Lithium Intercalation in Titanium Dioxide,” *Phys. Rev. Lett.*, vol. 86, no. 7, pp. 1275–1278, Feb. 2001.

[150] H.-Y. Wu, M.-H. Hon, C.-Y. Kuan, and I.-C. Leu, "Synthesis of TiO_2(B)/SnO_2 composite materials as an anode for lithium-ion batteries," *Ceram. Int.*, vol. 41, no. 8, pp. 9527–9533, Sep. 2015.
[151] M. Zukalová, M. Kalbáč, L. Kavan, I. Exnar, and M. Graetzel, "Pseudocapacitive Lithium Storage in TiO_2(B)," *Chem. Mater.*, vol. 17, no. 5, pp. 1248–1255, Mar. 2005.
[152] Y. Zhang *et al.*, "Titanate and titania nanostructured materials for environmental and energy applications: a review," *RSC Adv.*, vol. 5, no. 97, pp. 79479–79510, Sep. 2015.
[153] H. Wang, C. Guan, X. Wang, and H. J. Fan, "A High Energy and Power Li-Ion Capacitor Based on a TiO_2 Nanobelt Array Anode and a Graphene Hydrogel Cathode," *Small*, vol. 11, no. 12, pp. 1470–1477, Mar. 2015.
[154] H. Yang, C.-K. Lan, and J.-G. Duh, "The power of Nb-substituted TiO_2 in Li-ion batteries: Morphology transformation induced by high concentration substitution," *J. Power Sources*, vol. 288, pp. 401–408, Aug. 2015.
[155] Y.-S. Hu, L. Kienle, Y.-G. Guo, and J. Maier, "High Lithium Electroactivity of Nanometer-Sized Rutile TiO_2," *Adv. Mater.*, vol. 18, no. 11, pp. 1421–1426, Jun. 2006.
[156] M. Wagemaker, W. J. H. Borghols, and F. M. Mulder, "Large Impact of Particle Size on Insertion Reactions. A Case for Anatase LixTiO2," *J. Am. Chem. Soc.*, vol. 129, no. 14, pp. 4323–4327, Apr. 2007.
[157] X. H. Wang, C. Guan, L. M. Sun, R. A. Susantyoko, H. J. Fan, and Q. Zhang, "Highly stable and flexible Li-ion battery anodes based on TiO_2 coated 3D carbon nanostructures," *J. Mater. Chem. A*, vol. 3, no. 30, pp. 15394–15398, Jul. 2015.
[158] E. Madej, E. Ventosa, S. Klink, W. Schuhmann, and F. L. Mantia, "Aging effects of anatase TiO_2 nanoparticles in Li-ion batteries," *Phys. Chem. Chem. Phys.*, vol. 16, no. 17, pp. 7939–7945, Apr. 2014.
[159] Y. Cai, "Non-aqueous hybrid supercapacitors fabricated with mesoporous TiO_2 microspheres and activated carbon electrodes with superior performance," vol. 253, no. Complete, pp. 80–89.
[160] D. Dambournet, I. Belharouak, and K. Amine, "Tailored Preparation Methods of TiO_2 Anatase, Rutile, Brookite: Mechanism of Formation and Electrochemical Properties," *Chem. Mater.*, vol. 22, no. 3, pp. 1173–1179, Feb. 2010.
[161] G. Zampardi, E. Ventosa, F. L. Mantia, and W. Schuhmann, "In situ visualization of Li-ion intercalation and formation of the solid electrolyte interphase on TiO_2 based paste electrodes using scanning electrochemical microscopy," *Chem. Commun.*, vol. 49, no. 81, pp. 9347–9349, Sep. 2013.
[162] H. F. Xiang *et al.*, "Graphene sheets as anode materials for Li-ion batteries: preparation, structure, electrochemical properties and mechanism for lithium storage," *RSC Adv.*, vol. 2, no. 17, p. 6792, 2012.
[163] Y. Firouz, N. Omar, J.-M. Timmermans, P. Van den Bossche, and J. Van Mierlo, "Lithium-ion capacitor – Characterization and development of new electrical model," *Energy*, vol. 83, pp. 597–613, Apr. 2015.
[164] W. S. V. Lee, E. Peng, M. Li, X. Huang, and J. M. Xue, "Rational design of stable 4 V lithium ion capacitor," *Nano Energy*, vol. 27, pp. 202–212, Sep. 2016.
[165] M. Kim *et al.*, "A fast and efficient pre-doping approach to high energy density lithium-ion hybrid capacitors," *J. Mater. Chem. A*, vol. 2, no. 26, pp. 10029–10033, Jun. 2014.
[166] J. Ji *et al.*, "In Situ Activation of Nitrogen-Doped Graphene Anchored on Graphite Foam for a High-Capacity Anode," *ACS Nano*, vol. 9, no. 8, pp. 8609–8616, Aug. 2015.

[167] C. Wang, M. J. O'Connell, and C. K. Chan, "Facile One-Pot Synthesis of Highly Porous Carbon Foams for High-Performance Supercapacitors Using Template-Free Direct Pyrolysis," *ACS Appl. Mater. Interfaces*, vol. 7, no. 16, pp. 8952–8960, Apr. 2015.
[168] H. Ji *et al.*, "Ultrathin Graphite Foam: A Three-Dimensional Conductive Network for Battery Electrodes," *Nano Lett.*, vol. 12, no. 5, pp. 2446–2451, May 2012.
[169] J. C. Lytle *et al.*, "The right kind of interior for multifunctional electrode architectures: carbon nanofoam papers with aperiodic submicrometre pore networks interconnected in 3D," *Energy Environ. Sci.*, vol. 4, no. 5, pp. 1913–1925, 2011.
[170] J.-H. Kim, E. Jeong, and Y.-S. Lee, "Preparation and characterization of graphite foams," *J. Ind. Eng. Chem.*, vol. 32, pp. 21–33, Dec. 2015.
[171] J. Li *et al.*, "A facile method to prepare highly compressible three-dimensional graphene-only sponge," *J. Mater. Chem. A*, vol. 3, no. 30, pp. 15482–15488, Jul. 2015.
[172] E. Wilson and M. F. Islam, "Ultracompressible, High-Rate Supercapacitors from Graphene-Coated Carbon Nanotube Aerogels," *ACS Appl. Mater. Interfaces*, vol. 7, no. 9, pp. 5612–5618, Mar. 2015.
[173] Y. Ma, H. D. Asfaw, and K. Edström, "Three-dimensional carbon foam supported tin oxide nanocrystallites with tunable size range: Sulfonate anchoring synthesis and high rate lithium storage properties," *J. Power Sources*, vol. 294, pp. 208–215, Oct. 2015.
[174] H. Zhu *et al.*, "A Robust and Cost-Effective Superhydrophobic Graphene Foam for Efficient Oil and Organic Solvent Recovery," *Small*, vol. 11, no. 39, pp. 5222–5229, Oct. 2015.
[175] V. Chabot, B. Kim, B. Sloper, C. Tzoganakis, and A. Yu, "High yield production and purification of few layer graphene by Gum Arabic assisted physical sonication," *Sci. Rep.*, vol. 3, Mar. 2013.
[176] Y. Zhu *et al.*, "Graphene and Graphene Oxide: Synthesis, Properties, and Applications," *Adv. Mater.*, vol. 22, no. 35, pp. 3906–3924, Sep. 2010.
[177] E. Yoo, J. Kim, E. Hosono, H. Zhou, T. Kudo, and I. Honma, "Large Reversible Li Storage of Graphene Nanosheet Families for Use in Rechargeable Lithium Ion Batteries," *Nano Lett.*, vol. 8, no. 8, pp. 2277–2282, Aug. 2008.
[178] D. Geng *et al.*, "Nitrogen doping effects on the structure of graphene," *Appl. Surf. Sci.*, vol. 257, no. 21, pp. 9193–9198, Aug. 2011.
[179] F. M. Hassan, V. Chabot, J. Li, B. K. Kim, L. Ricardez-Sandoval, and A. Yu, "Pyrrolic-structure enriched nitrogen doped graphene for highly efficient next generation supercapacitors," *J. Mater. Chem. A*, vol. 1, no. 8, pp. 2904–2912, Jan. 2013.
[180] D. Hulicova-Jurcakova, M. Kodama, S. Shiraishi, H. Hatori, Z. H. Zhu, and G. Q. Lu, "Nitrogen-Enriched Nonporous Carbon Electrodes with Extraordinary Supercapacitance," *Adv. Funct. Mater.*, vol. 19, no. 11, pp. 1800–1809, Jun. 2009.
[181] J. Tan, H. Chen, Y. Gao, and H. Li, "Nitrogen-doped porous carbon derived from citric acid and urea with outstanding supercapacitance performance," *Electrochimica Acta*, vol. 178, pp. 144–152, Oct. 2015.
[182] F. Wang *et al.*, "A Quasi-Solid-State Li-Ion Capacitor Based on Porous TiO_2 Hollow Microspheres Wrapped with Graphene Nanosheets," *Small*, vol. 12, no. 45, pp. 6207–6213, Dec. 2016.
[183] T. Liu, F. Zhang, Y. Song, and Y. Li, "Revitalizing carbon supercapacitor electrodes with hierarchical porous structures," *J. Mater. Chem. A*, vol. 5, no. 34, pp. 17705–17733, Aug. 2017.

[184] M. D. Stoller and R. S. Ruoff, “Best practice methods for determining an electrode material’s performance for ultracapacitors,” *Energy Environ. Sci.*, vol. 3, no. 9, p. 1294, 2010.
[185] S. A. Hamidi, E. Manla, and A. Nasiri, “Li-ion batteries and Li-ion ultracapacitors: Characteristics, modeling and grid applications,” in *2015 IEEE Energy Conversion Congress and Exposition (ECCE)*, 2015, pp. 4973–4979.
[186] K. Lee, H. Lee, Y. Shin, Y. Yoon, D. Kim, and H. Lee, “Highly transparent and flexible supercapacitors using graphene-graphene quantum dots chelate,” *Nano Energy*, vol. 26, pp. 746–754, Aug. 2016.
[187] J. Chen, K. Fang, Q. Chen, J. Xu, and C.-P. Wong, “Integrated paper electrodes derived from cotton stalks for high-performance flexible supercapacitors,” *Nano Energy*, Aug. 2018.
[188] Y. Chen, X.-Y. Fu, Y.-Y. Yue, N. Zhang, J. Feng, and H.-B. Sun, “Flexible and transparent supercapacitor based on ultrathin Au/graphene composite electrodes,” *Appl. Surf. Sci.*, vol. 467–468, pp. 104–111, Feb. 2019.
[189] S. J. Patil and D.-W. Lee, “Scalable and ascendant synthesis of carbon cloth coated hierarchical core–shell CoMoS@Co(OH) 2 for flexible and high-performance supercapacitors,” *J. Mater. Chem. A*, vol. 6, no. 20, pp. 9592–9603, 2018.
[190] L. Lim *et al.*, “All-in-One Graphene Based Composite Fiber: Toward Wearable Supercapacitor,” *ACS Appl. Mater. Interfaces*, vol. 9, no. 45, pp. 39576–39583, Nov. 2017.
[191] W. Liu, K. Feng, G. Lui, R. Tjandra, L. Lim, and A. Yu, “Hair-Based Flexible All-Solid-State Supercapacitor with Wide Operating Voltage and Ultra-High Rate Capability,” *Meet. Abstr.*, vol. MA2017-02, no. 3, pp. 197–197, Sep. 2017.
[192] R. Tjandra, G. Li, X. Wang, J. Yan, M. Li, and A. Yu, “Flexible high performance lithium ion battery electrode based on a free-standing TiO_2 nanocrystals/carbon cloth composite,” *RSC Adv.*, vol. 6, no. 42, pp. 35479–35485, Apr. 2016.
[193] Z. Wang, W. Zhang, X. Li, and L. Gao, “Recent progress in flexible energy storage materials for lithium-ion batteries and electrochemical capacitors: A review,” *Journal of Materials Research*, Jun-2016. [Online]. Available: /core/journals/journal-of-materials-research/article/div-classtitlerecent-progress-in-flexible-energy-storage-materials-for-lithium-ion-batteries-and-electrochemical-capacitors-a-reviewdiv/643F478C3A57FE47048A6B6095D55141/core-reader. [Accessed: 31-Jan-2017].
[194] G. Chen *et al.*, “Robust, hydrophilic graphene/cellulose nanocrystal fiber-based electrode with high capacitive performance and conductivity,” *Carbon*, vol. 127, no. Supplement C, pp. 218–227, Feb. 2018.
[195] M. Dirican *et al.*, “Flexible binder-free silicon/silica/carbon nanofiber composites as anode for lithium–ion batteries,” *Electrochimica Acta*, vol. 169, pp. 52–60, Jul. 2015.
[196] L. Gao *et al.*, “Flexible Fiber-Shaped Supercapacitor Based on Nickel–Cobalt Double Hydroxide and Pen Ink Electrodes on Metallized Carbon Fiber,” *ACS Appl. Mater. Interfaces*, vol. 9, no. 6, pp. 5409–5418, Feb. 2017.
[197] K. Guo, X. Wang, L. Hu, T. Zhai, H. Li, and N. Yu, “Highly Stretchable Waterproof Fiber Asymmetric Supercapacitors in an Integrated Structure,” *ACS Appl. Mater. Interfaces*, May 2018.

[198] P. Dai *et al.*, “Paper-Derived Flexible 3D Interconnected Carbon Microfiber Networks with Controllable Pore Sizes for Supercapacitors,” *ACS Appl. Mater. Interfaces*, Oct. 2018.
[199] W. Luo, X. Li, and J. Y. Chen, “All-fabric flexible supercapacitor for energy storage,” *J. Ind. Text.*, p. 1528083718804208, Oct. 2018.
[200] Y. Zhao *et al.*, “Highly Compression-Tolerant Supercapacitor Based on Polypyrrole-mediated Graphene Foam Electrodes,” *Adv. Mater.*, vol. 25, no. 4, pp. 591–595, Jan. 2013.
[201] R. Tjandra, W. Liu, L. Lim, and A. Yu, “Melamine based, n-doped carbon/reduced graphene oxide composite foam for Li-ion Hybrid Supercapacitors,” *Carbon*, vol. 129, pp. 152–158, Apr. 2018.
[202] H. Jeon *et al.*, “Facile and fast microwave-assisted fabrication of activated and porous carbon cloth composites with graphene and MnO2 for flexible asymmetric supercapacitors,” *Electrochimica Acta*, vol. 280, pp. 9–16, Aug. 2018.
[203] G. Wang *et al.*, “Solid-State Supercapacitor Based on Activated Carbon Cloths Exhibits Excellent Rate Capability,” *Adv. Mater.*, vol. 26, no. 17, pp. 2676–2682.
[204] Y. Zhou, P. Jin, Y. Zhou, and Y. Zhu, “High-performance symmetric supercapacitors based on carbon nanotube/graphite nanofiber nanocomposites,” *Sci. Rep.*, vol. 8, no. 1, p. 9005, Jun. 2018.
[205] Y. Dong *et al.*, “One-step and high yield simultaneous preparation of single- and multi-layer graphene quantum dots from CX-72 carbon black,” *J. Mater. Chem.*, vol. 22, no. 18, pp. 8764–8766, Apr. 2012.
[206] Y. Li *et al.*, “Free-Radical-Assisted Rapid Synthesis of Graphene Quantum Dots and Their Oxidizability Studies,” *Langmuir*, vol. 32, no. 34, pp. 8641–8649, Aug. 2016.
[207] J.-D. Xie, G.-W. Lai, and M. M. Huq, “Hydrothermal route to graphene quantum dots: Effects of precursor and temperature,” *Diam. Relat. Mater.*, vol. 79, pp. 112–118, Oct. 2017.
[208] F. Liu, M.-H. Jang, H. D. Ha, J.-H. Kim, Y.-H. Cho, and T. S. Seo, “Facile Synthetic Method for Pristine Graphene Quantum Dots and Graphene Oxide Quantum Dots: Origin of Blue and Green Luminescence,” *Adv. Mater.*, vol. 25, no. 27, pp. 3657–3662, Jul. 2013.
[209] R. Tian *et al.*, “Solvothermal method to prepare graphene quantum dots by hydrogen peroxide,” *Opt. Mater.*, vol. 60, no. Supplement C, pp. 204–208, Oct. 2016.
[210] Z. Li *et al.*, “Amine-enriched Graphene Quantum Dots for High-pseudocapacitance Supercapacitors,” *Electrochimica Acta*, vol. 208, pp. 260–266, Aug. 2016.
[211] M. K. Chini and S. Chatterjee, “Hydrothermally reduced nano porous graphene–polyaniline nanofiber composites for supercapacitor,” *FlatChem*, vol. 1, pp. 1–5, Jan. 2017.
[212] Y. J. Oh *et al.*, “Oxygen functional groups and electrochemical capacitive behavior of incompletely reduced graphene oxides as a thin-film electrode of supercapacitor,” *Electrochimica Acta*, vol. 116, pp. 118–128, Jan. 2014.
[213] Y. Yang *et al.*, “Waterproof, Ultrahigh Areal-Capacitance, Wearable Supercapacitor Fabrics,” *Adv. Mater.*, vol. 29, no. 19, p. 1606679, May 2017.
[214] “Highly Transparent and Flexible All-Solid-State Supercapacitors Based on Ultralong Silver Nanowire Conductive Networks.” [Online]. Available: https://pubs.acs.org/doi/pdf/10.1021/acsami.8b10138. [Accessed: 03-Jan-2019].

[215] N.-J. Kuo, Y.-S. Chen, C.-W. Wu, C.-Y. Huang, Y.-H. Chan, and I.-W. P. Chen, "One-Pot Synthesis of Hydrophilic and Hydrophobic N-Doped Graphene Quantum Dots via Exfoliating and Disintegrating Graphite Flakes," *Sci. Rep.*, vol. 6, p. 30426, Jul. 2016.
[216] Y. Hu *et al.*, "Graphene quantum dots–carbon nanotube hybrid arrays for supercapacitors," *Nanotechnology*, vol. 24, no. 19, p. 195401, 2013.
[217] J. Hou, C. Cao, F. Idrees, and X. Ma, "Hierarchical Porous Nitrogen-Doped Carbon Nanosheets Derived from Silk for Ultrahigh-Capacity Battery Anodes and Supercapacitors," *ACS Nano*, vol. 9, no. 3, pp. 2556–2564, Mar. 2015.
[218] Y.-X. Tong *et al.*, "Nitrogen-doped hierarchical porous carbon derived from block copolymer for supercapacitor," *Energy Storage Mater.*, vol. 3, pp. 140–148, Apr. 2016.
[219] J. Xu *et al.*, "A Hierarchical Carbon Derived from Sponge-Templated Activation of Graphene Oxide for High-Performance Supercapacitor Electrodes," *Adv. Mater.*, vol. 28, no. 26, pp. 5222–5228, 2016.
[220] M.-H. Kim, K.-B. Kim, S.-M. Park, and K. C. Roh, "Hierarchically structured activated carbon for ultracapacitors," *Sci. Rep.*, vol. 6, p. 21182, Feb. 2016.
[221] I. Mustafa, I. Lopez, H. Younes, R. A. Susantyoko, R. A. Al-Rub, and S. Almheiri, "Fabrication of Freestanding Sheets of Multiwalled Carbon Nanotubes (Buckypapers) for Vanadium Redox Flow Batteries and Effects of Fabrication Variables on Electrochemical Performance," *Electrochimica Acta*, vol. 230, pp. 222–235, Mar. 2017.
[222] D. Wang *et al.*, "Facile and Scalable Preparation of Fluorescent Carbon Dots for Multifunctional Applications," *Engineering*, vol. 3, no. 3, pp. 402–408, Jun. 2017.
[223] J. Peng *et al.*, "Graphene Quantum Dots Derived from Carbon Fibers," *Nano Lett.*, vol. 12, no. 2, pp. 844–849, Feb. 2012.
[224] M. Buzaglo, M. Shtein, and O. Regev, "Graphene Quantum Dots Produced by Microfluidization," *Chem. Mater.*, vol. 28, no. 1, pp. 21–24, Jan. 2016.

Appendix A: Research Contributions

Publications (Refereed Journals)

[1] G. Lui, X. Sun, L. Yang, Y.-S. Jun, **R. Tjandra**, and A. Yu, "Three-Dimensional Architecture of Carbon Nanotube-Anchored Carbon Nanofiber Epoxy Composite," *Journal of Nanoengineering and Nanomanufacturing*, vol. 4, no. 4, pp. 311–315, Dec. 2014.

[2] Y.-S. Jun, S. Sy, W. Ahn, H. Zarrin, L. Rasenthiram, **R. Tjandra**, B. Amoli, B. Zhao, G. Chiu, A. Yu, "Highly conductive interconnected graphene foam based polymer composite," *Carbon*, vol. 95, pp. 653–658, Dec. 2015.

[3] **R. Tjandra**, G. Lui, A. Veilleux, J. Broughton, G. Chiu, and A. Yu, "Introduction of an Enhanced Binding of Reduced Graphene Oxide to Polyurethane Sponge for Oil Absorption," *Ind. Eng. Chem. Res.*, Mar. 2015.

[4] X. Wang, G. Li, **R. Tjandra**, X. Fan, X. Xiao, and A. Yu, "Fast lithium-ion storage of Nb2O5 nanocrystals in situ grown on carbon nanotubes for high-performance asymmetric supercapacitors," *RSC Adv.*, vol. 5, no. 51, pp. 41179–41185, May 2015.

[5] X. Wu, Z. Shi, **R. Tjandra**, A. Cousins, S. Sy, A. Yu, R.M. Berry, K.C Tam, "Nitrogen-enriched Porous Carbon Nanorods Templated by Cellulose Nanocrystals as High Performance Supercapacitor Electrode," *J. Mater. Chem. A*, Oct. 2015.

[6] J. Yan, G. Lui, **R. Tjandra**, X. Wang, L. Rasenthiram, and A. Yu, "α-NiS grown on reduced graphene oxide and single-wall carbon nanotubes as electrode materials for high-power supercapacitors," *RSC Adv.*, vol. 5, no. 35, pp. 27940–27945, Mar. 2015.

[7] W. Liu, J. Li, K. Feng, S. Sy, Y. Liu, L. Lim, G. Lui, **R. Tjandra**, L. Rasenthiram, G. Chiu, A. Yu, "Advanced Li-ion Hybrid Supercapacitors Based on 3D Graphene–Foam Composites," *ACS Applied Materials & Interfaces*, vol. 8, no. 39, pp. 25941–25953, Oct. 2016.

[8] W. Liu, C. Lu, H. Li, R.Y. Tay, L. Sun, X. Wang, W.L. Chow, X. Wang, B.K. Tay, Z. Chen, J. Yan, K. Feng, G. Lui, **R. Tjandra**, L. Rasenthiram, G. Chiu, A. Yu, "Paper-based all-solid-state flexible micro-supercapacitors with ultra-high rate and rapid frequency response capabilities," *J. Mater. Chem. A*, vol. 4, no. 10, pp. 3754–3764, Mar. 2016.

[9] **R. Tjandra**, G. Li, X. Wang, J. Yan, M. Li, and A. Yu, "Flexible high performance lithium ion battery electrode based on a free-standing TiO_2 nanocrystals/carbon cloth composite," *RSC Adv.*, vol. 6, no. 42, pp. 35479–35485, Apr. 2016.

[10] L. Lim, Y. Liu, W. Liu, **R. Tjandra**, L. Rasenthiram, Z. Chen, A. Yu, "All-in-One Graphene Based Composite Fiber: Toward Wearable Supercapacitor," *ACS Appl. Mater. Interfaces*, vol. 9, no. 45, pp. 39576–39583, Nov. 2017.

[11] **R. Tjandra**, W. Liu, L. Lim, and A. Yu, "Melamine based, n-doped carbon/reduced graphene oxide composite foam for Li-ion Hybrid Supercapacitors," *Carbon*, vol. 129, pp. 152–158, Apr. 2018.

[12] J. Yan, L. Rasenthiram, H. Fang, **R. Tjandra**, L. Wang, L. Wang, Y. Zhang, L. Zhang, A. Yu,"From amorphous to crystalline: in situ growth Ni-Co chalcogenides hybrid nanostructure on carbon cloth for supercapacitor," *Ionics*, Sep. 2018.

[13] J. Yan, **R. Tjandra**, H. Fang, L.-X. Wang, and A. Yu, "Boron acid catalyzed synthesis porous graphene sponge for high-performance electrochemical capacitive storage," *Diamond and Related Materials*, vol. 89, pp. 114–121, Oct. 2018.

Prepared & Submitted for Publication

[14] **R. Tjandra**, W. Liu, M. Zhang, A. Yu, "All-carbon flexible supercapacitors based on electrophoretic deposition of Graphene quantum dots on carbon cloth". (Submitted to *Journal of Power Sources*)

[15] M. Zhang, W. Liu, R. Liang, **R. Tjandra**, A. Yu, "Graphene quantum dots Induced Tunable Growth of Nanostructured $MnCo_2O_{4.5}$ Composites for High-Performance Supercapacitors". (In preparation)

Conference Presentations

[16] **R. Tjandra**, G. Lui, A. Veilleux, J. Broughton, G. Chiu, and A. Yu, "Enhanced Binding of Reduced Graphene Oxide to Polyurethane Spsonge for Oil Absorption", Graphene Canada 2016, Montreal, Canada, October 18 – 20, 2016. (Oral Presentation)

[17] **R. Tjandra**, G. Li, X. Wang, J. Yan, M. Li, and A. Yu, "Flexible high performance Lithium Ion Battery Electrode based on Free-standing TiO_2 Nanocrystals/Carbon Cloth composite", 232nd Electrochemical Society Meeting, National Harbour, United Sates, October 1 – 5, 2017. (Poster Presentation)

[18] **R. Tjandra,** W. Liu, L. Lim, A. Yu, "Melamine-Based, N-Doped Carbon/Reduced Graphene Composite Foam for Li-ion Batteries and Hybrid Supercapacitors", 232nd Electrochemical Society Meeting, National Harbour, United States, October 1 – 5, 2017. (Oral Presentation)

[19] **R. Tjandra,** W. Liu, L. Lim, A. Yu, "Melamine based, n-doped carbon/reduced graphene oxide composite foam for Li-ion Hybrid Supercapacitors", 68th Canadian Chemical Engineering Conference, Toronto, Canada, October 28-31, 2018. (Oral Presentation)